Spike train discrimination and analysis in neural and surface electromyography (sEMG) applications

Ivan GLIGORIJEVIĆ

Jury:
Prof. dr. Yves Willems, chairman
Prof. dr. Sabine Van Huffel, promotor
Prof. dr. Bart Nuttin, promotor
Prof. dr. Carmen Bartic, promotor
Prof. dr. Mirjana Popović
(Belgrade University, Serbia)
Prof. dr. Maarten De Vos
(University of Oldenburg, Germany)
Dr. Joleen H. Blok
(Department of Clinical Neurophysiology, Erasmus MC, The Netherlands)
Prof. dr. Marc Van Hulle
Prof. dr. Robert Puers

Dissertation presented in partial fulfillment of the requirements for the degree of Doctor in Engineering

April 2013

© KU Leuven – Faculty of Engineering
Arenbergkasteel, B-3001 Leuven-Heverlee, Belgium

Alle rechten voorbehouden. Niets uit deze uitgave mag worden vermenigvuldigd en/of openbaar gemaakt worden door middel van druk, fotokopie, microfilm, elektronisch of op welke andere wijze ook zonder voorafgaande schriftelijke toestemming van de uitgever.

All rights reserved. No part of the publication may be reproduced in any form by print, photoprint, microfilm or any other means without written permission from the publisher.

Legal depot number D/2013/7515/36
ISBN number 978-94-6018-650-9

The only people with whom you should try to get even are those who have helped you.

John E. Southard

Acknowledgments

It is impossible to thank all the people who deserve it in a fair way. The truth is, without many individuals that surrounded me, you probably wouldn't be reading this text now. One way that crossed my mind and that goes along well with the topic of this thesis would be to classify these people according to various criteria: moral, technical or other support. However, this would grant largely overlapping groups. One obvious advantage would be that I wouldn't have to worry about outliers because there wouldn't be any ◡̈. However, I would still be unable to define an order of importance. So, after all these years of learning how to structure my work, I will return to the beginning and completely randomly say what's on my soul giving the same weight to every paragraph.

I will start with my mentor, professor Sabine Van Huffel. I intentionally say mentor rather than supervisor or promotor. This is because she was more than that, a true support in every sense, giving away positive energy all around her and always believing in me. She taught me a valuable lesson that everything can be done if you just believe in it. I think I will never be able to repay that debt. Sabine, thank you for everything!

My two other promotors, professors Bart Nuttin and Carmen Bartic, provided me with large amount of knowledge related to the topic of this thesis, but also taught me the basics of ways that researchers think, something completely new and invaluable for me.

IMEC provided an SLT scholarship that made my research possible throughout all these years, for which I am very thankful, it was a great honor for me.

I would like to mention Bogdan, a friend someone can only wish to have, always there when you need him. Probably I would need much more space if I wanted to even start describing his friendship. Bogi, thanks, thanks a lot...

Maarten De Vos is probably one of the best researchers I met so far. He often guided my work and wasn't afraid to meet the "Serbian" way. He had the kindest words to explain me I am wrong in a way that almost left me feeling good ◡̈.

Thanks Maarten, you are a great friend!

My parents, Nikola and Ljiljana, and my sister Maja were the people behind the scenes responsible for my constant "smiling face" that most of the people know. This is because they were the vacuum cleaner for my negative energy, people who I turn to when I feel worst. Hvala tata, mama i seko, volim vas puno!

My time in Leuven was very dynamic and interesting, largely thanks to my Balkan crew, friends for all occasions, Mire, Vulić, Ilija, Duško, Tićma (also my favorite travel companion), Meto, Aca Perić, Dušan, Ljiljana (always taking care of my well-being), Jelena (great supporter in moments of panic), Topke, Marija, Ivana & Ivana,... you are really great! The Balkan crew would be incomplete without its a bit older (but still very young) part: Staki, Cina, Milan, Maja, Zrna, Sloba, Ivana, Vlada, Bilja, Miki, Dara, Miša, Nena...and their unforgettable parties and great care for all of us. Thanks boys and girls!

I owe special thanks to Cvetković family. Usually a person can have up to one mother. I had luck to get the second - Marina, who tried her best to make me a better man and to teach me not to wear white socks. Bane is a guy for everything, a loyal friend, universal problem solver, 24/7, all year long. He is still an active rock star, because ladies just don't let him retire. Damjan and Ana can only have the best future - with Marina to teach them all the good things and Bane to explain them the difference between bad and worse ◡̈

My "kumići" Milan and Sneža are just two great people that always accepted me in their home, laughed all problems away and offered any help whenever needed. I am really happy to have you two!

I must mention the cool people I met in various, usually very strange and unlikely occasions. Dries, Olga, Anna, Anastasia, Julia, Gulya, Francisca, Mirjam, Enrico, Dina, Alexandros, Zhanna... you made me feel good too many times!

Getting back to work, I have to mention my colleagues from Biomed group, my dear Katrien, Ninah, Bori, Yipeng (the king), Anca, Diana, Steven, Maria, Mariya, Kris, Rosy, Joachim, Alex, Carolina, Devy (a.k.a. Linden), Milica, Vanya, Kirsten, Ben, Jan, Laure, Wouter...you are a cool crowd! Although not researchers, John Vos, Mimi and Ida also deserve my thanks for making my life easier by solving administrative problems I managed to create ◡̈

I probably wouldn't know half of the things I know without having the discussions with Dimiter, Marleen, Silke, Kris, Hemmings, Thoa, Carolina...my IMEC crowd. Joleen Blok, Hans van Dijk and Boudewijn Sleutjes brought me to the world of muscle related research and gave me the knowledge I probably wouldn't be able to gather in years without them.

At the end, I would like to thank the jury for taking the time to read this manuscript and providing valuable suggestions for improving the final version.

For sure I forgot someone important, but I am stopping here. Good things are easy to forget and I hope that other people that deserve credit won't be too harsh on me.

U sećanje na mog dragog deda Gradu. "Ivo, nemo' da si frajer"...

Ivan Gligorijević
Leuven, April 2013

Abstract

The term "spike" is used to describe a short-time event that is the result of the activity of its source. Spikes can be seen in different signal modalities. In these modalities, often more than one source generates spikes. Classification algorithms can be used to group similar spikes, ideally spikes from the same source. This work examines the classification of spikes generated from neurons and muscles. When each detected spike is assigned to its source, the spike trains of these sources can provide information on complex brain network functioning, muscle disorders, and other applications. During the past several decades, there were many attempts to create and improve spike classification algorithms. No matter how advanced these methods are today, errors in classification cannot be avoided. Therefore, methods that would determine and improve reliability of classification are very desirable.

In this work, it is attempted to find efficient solutions for post-processing of spike trains extracted after the classification to increase their accuracy and reliability. This is done for two different signal types: neural and muscle signals. The aim was to create a reliable and automated signal processing framework. In modern neural microarray probes, many recording channels provide large quantities of data, which require an enormous amount of time to be analyzed. A fully automated system is therefore needed but is still out of reach. As for the analysis of muscle signals, treated by surface electromyography (sEMG), many recording channels observe the same spikes simultaneously. Due to the frequently overlapping spikes, only automated sophisticated methods are able to perform classification.

Starting from the problem of spike classification errors as such, independent from the used algorithm, the possibility of classification in low signal-to-noise ratio (SNR) cases is examined. This part of the work indicated the under limits in terms of SNR for trustworthy classification. Then, parameters to describe firing pattern of spikes are described and new parameters are proposed. These parameters are tested for reliability and the amount of information they are able to retrieve from the firing pattern. This logic and knowledge is then exploited in a obsessive-compulsive disorder (OCD) study where the analysis of extracted spike trains revealed the connection of a specific brain area (bed nucleus of striaterminalis - BST) to this

disorder.

In the case of the analysis of muscle signals using surface multichannel recording grids, classification of spikes is called decomposition. Due to more frequent spiking of different sources, spikes of different sources are often overlapping and the goal is to extract time instances of individual sources as well as the respective spike shapes. Achieving the decomposition of surface electromyography (sEMG) signals is needed to better understand certain muscle disorders and increase knowledge of the neuromuscular system. A new method for decomposition is proposed and successfully applied as demonstrated on real and simulated data.

Motor units are the lowest functional units in muscles. Each motor unit produces characteristic spikes. The goal of motor unit tracking is to identify the same motor units in subsequent measurements. Using the developed decomposition method to extract spikes from voluntary muscle contractions, a solution is devised that assists the motor unit tracking. The method is able to compensate for the effects of recording grid displacements in an automated manner. This results in substantial reduction of previously needed man-hours to achieve very precise placement of the measurement grid. The feasibility of this method is demonstrated on a recording mimicking accidental grid displacements. This tool provides the possibility to do non-invasive follow-up studies investigating the effects of various muscle disorders.

Samenvatting

De term "spike" word gebruikt om gebeurtenissen van korte duur, die door een bepaalde bron gegenereerd worden, te beschrijven. Spikes kunnen in verschillende signalen teruggevonden worden. In deze signalen is er vaak meer dan één bron actief om spikes tegenereren. Classificatiealgoritmes kunnen gebruikt worden om gelijkaardige spikes te groeperen, in het ideale geval zijn dit spikes opgewekt door dezelfde bron. Dit werk bestudeert de classificatie van spikes die gegenereerd worden in neuronen en spieren. Wanneer elke gedetecteerde spike aan een bepaalde bron is toegeschreven, kunnen de tijdstippen waarop de spikes gegenereerd zijn (activatiepatronen), informatie geven over complexe hersennetwerken, spierziektes en andere toepassingen. Tijdens de laatste decennia zijn er veel pogingen geweest om classificatiealgoritmes te ontwikkelen en te verbeteren. Ongeacht de complexiteit van deze methodes, kunnen classificatiefouten echter niet vermeden worden. Daarom is er nood aan methodes die de betrouwbaarheid van de classificatie kunnen bepalen en verbeteren.

In dit werk is getracht om efficiënte oplossingen te vinden voor de nabewerking van de activatiepatronen van spikes na classificatie, en dit teneinde de betrouwbaarheid te verbeteren. Dit werd gedaan voor twee verschillende types van signalen: neuronale en spiersignalen. Het doel was om een betrouwbaar en automatisch signaalverwerkingskader op te stellen. Tijdens een meting van neuronale activiteit met moderne "microarray probes", wordt een grote hoeveelheid data gegenereerd door de verschillende kanalen. Deze hoeveelheid data vraagt dus ook veel tijd om geanalyseerd te worden. Een volledig geautomatiseerd systeem is daarom nodig. Voor de analyse van spiersignalen, gemeten met een oppervlakte-electromyogram (sEMG), is het probleem dat dezelfde spikes op verschillende kanalen tegelijkertijd gezien worden. Door de vaak overlappende spikes, kunnen alleen geavanceerde algoritmes de classificatie succesvol uitvoeren.

Vertrekkende van het probleem van fouten in spike-classificatie werd bestudeerd bijwelke lage signaal-tot-ruis (SNR) verhoudingen het mogelijk is classificatie te doen en dit los van het gebruikte classificatiealgoritme. Op deze manier werd een ondergrens van betrouwbare SNR waarden voor classificatie bepaald. Daarnaast

zijn parameters om de activatiepatronen van de spikes te beschrijven bestudeerd en nieuwe parameters voorgesteld. Deze parameters zijn getest in functie van hun betrouwbaarheid en de hoeveelheid informatie die kan afgeleid worden van de activatiepatronen. Deze logica en kennis is dan gebruikt in een studie van obsessief-compulsieve aandoeningen (OCD), waar de analyse van activatiepatronen van de spikes een nieuwe connectie van een specifiek hersengebied (BST) met de ziekte aantoonde.

In de analyse van spiersignalen met meerkanaals-meetroosters, wordt classificatie van spikes vaak decompositie genoemd. Door de frequente spiking van verschillende bronnen, kunnen spikes van verschillende bronnen overlappen. Daarom is het de bedoeling om de tijdsinstanties van individuele bronnen te extraheren samen met de overeenkomstige spike-vormen zelf. Decompositie van sEMG signalen is nodig om bepaalde spierziektes beter te begrijpen. Een nieuwe methode voor decompositie is voorgesteld en succesvol toegepast op gesimuleerde en reële data.

Motoreenheden zijn de laagste functionele eenheden in spieren. Elke motoreenheid produceert karakteristieke spikes. Het doel van het opvolgen van motoreenheden is om dezelfde eenheden in verschillende meetsessies op te volgen. Met behulp van de nieuwe decompositiemethode om spikes te extraheren, is een methode ontwikkeld om opvolging van specifieke motoreenheden te doen. De methode maakt het mogelijk om de effecten van onnauwkeurigheden in het plaatsen van de meetroosters te compenseren. Dit resulteert in een substantiële reductie van het aantal manuren om de meetroosters precies te positioneren. De mogelijkheid om de methode te gebruiken is aangetoond met een meting die accidentele roosterverplaatsingen nabootst. Deze methode heeft het potentieel om niet-invasieve follow-up studies uit te voeren om de effecten van verschillende spierziekten op te volgen.

×

Abbreviations

ALS	amyotrophic lateral sclerosis
ARMA	autoregressive moving average
BiTDD	bi-transversal double differential (filter)
BSS	blind source separation
BST	bed nucleus of stria terminalis
C_V	coefficient of variation
CNS	central nervous system
CON	control (group)
CV	conduction velocity
DBRS	Deep Brain Recording and Stimulation
DBS	Deep Brain Stimulation
DWT	discrete wavelet transform
EMD	Empirical Mode Decomposition
EMG	electromyography
fMRI	functional Magnetic Resonance Imaging
GP	globus pallidus
GUI	graphical user interface
HD-sEMG	high density surface electromyography
ICA	Independent Component Analysis
ISI	inter-spike interval
ISIH	inter-spike interval histogram
IZ	innervation zone
LFP	local field potential
MCA	Morphological Component Analysis
MNF	mean frequency of the power spectrum
MT	extrastriate area of the MT in the monkey brain
MU	motor unit
MUAP	motor unit action potential
MUNE	motor unit number estimation
MUP	motor unit potential
MUPT	motor unit potential train
MVC	maximal voluntary contraction
NLEO	non-linear energy operator
NMJ	neuromuscular junction

NRMSE	normalized root mean square error
OCD	obsessive-compulsive disorder
PC	principal component
PCA	Principal Component Analysis
PCB	printed circuit board
RES	resistive (group)
RMS	root-mean-square
sEMG	surface electromyography
SEO	squared energy operator
SFAP	single-fiber action potential
SIP	schedule-induced polydipsia
SNR	signal-to-noise ratio
SPC	supeparamagnetic clustering
SSRIs	serotonin reuptake inhibitors
TEO	Teager-Kaiser energy operator

Contents

Acknowledgments iii

Abstract vi

Samenvatting viii

Abbreviations xi

Contents 1

Overview of the thesis 5

1 Introduction on spike sorting 9

1.1 Spike sorting 9

1.2 Origin and recording of neural spikes 10

1.3 Signal filtering 16

1.4 Spike detection and alignment 19

1.4.1 Spike detection 19

1.4.2 Alignment 22

1.5 Spike classification 23

1.5.1 Feature extraction 23

1.5.2 Feature reduction and classification 27

1.5.3 Variability of the spike shape 30
1.6 Superparamagnetic clustering algorithm 31
1.6.1 Outline of the algorithm 31
1.6.2 Variables of the model 32
1.6.3 Iterative procedure and achieving the clustering 33
1.6.4 Influence and setting of parameters 34

2 Reliability of statistical features describing neural spike trains in the presence of classification errors 37

2.1 Firing rate function of a spike train 37
2.2 Neuronal coding 39
2.2.1 Rate and temporal coding 39
2.2.2 What can we infer from the spike-rate function? 42
2.2.3 Homogeneous and Inhomogeneous Poisson process 42
2.3 Inter-spike interval (ISI) and autocorrelation histograms 44
2.4 Reliability of statistical features describing neural spike trains in the presence of classification errors 47
2.4.1 Methods 48
2.4.2 Results 57
2.4.3 Discussion 59
2.4.4 Conclusion 61
2.5 Additional comments on chapter composition 61

3 Obsessive-compulsive disorder (OCD) study 63

3.1 Introduction 64
3.2 Methods 65
3.2.1 Subjects and housing 65
3.2.2 Schedule-induced polydipsia model and experimental groups 66
3.2.3 Electrophysiological recording 66

3.2.4 Histology 67
3.2.5 Data analysis 67
3.2.6 Statistical analysis 68
3.3 Results 68
3.3.1 Firing rate and firing pattern in SIP rats, resistant rats and control rats 70
3.3.2 Left-right hemisphere comparisons 72
3.3.3 Correlations with position of the neurons within the BST . 75
3.4 Discussion 75
3.4.1 Neuronal activity in the BST 75
3.4.2 The BST in relation to OCD 77
3.4.3 General considerations 78
3.5 Conclusion 79

4 Surface electromyography (sEMG) 81
4.1 Human muscle physiology 81
4.2 Measuring electrical activity of the muscle 84
4.3 Decomposition of HD-sEMG 87
4.4 Applications of surface EMG 91
4.5 Conclusion 95

5 A new and fast approach towards HDsEMG decomposition 97
5.1 Introduction 98
5.2 Methods 99
5.2.1 Algorithm 99
5.2.2 Data 108
5.2.3 Validation 109
5.3 Results 110
5.3.1 Simulated data 110

5.3.2 Real data . . . 112
5.4 Discussion . . . 118
5.4.1 Simulated data . . . 118
5.4.2 Real data . . . 119
5.5 Conclusion . . . 121

6 Correcting electrode displacement errors in motor unit tracking using high density surface electromyography (HDsEMG) 123

6.1 Introduction . . . 123
6.2 Methods . . . 124
6.2.1 Recordings . . . 124
6.2.2 Artificial recording grid displacement . . . 127
6.3 Results . . . 129
6.4 Discussion . . . 133
6.5 Conclusion . . . 134

7 Conclusion and Future Work 139

7.1 Analysis of neuronal signals using multichannel neuroprobes . . . 139
7.1.1 Automated analysis of neural spike trains . . . 139
7.1.2 Future work on neural spike train processing . . . 141
7.2 Utilizing HD-sEMG for the analysis of muscle signals . . . 143
7.2.1 Analysis of signals recorded using HD-sEMG . . . 143
7.2.2 Future work on HD-sEMG . . . 144

Bibliography 149

List of Publications 165

Curriculum Vitae 169

Overview of the thesis

Aims of the thesis

This thesis focuses on the problem of spike extraction and classification for two different signal modalities. It aims to provide automated signal processing solutions for:

1. Extracting and analyzing neural spike trains recorded by microprobes inserted in a brain
2. Decomposition and analysis of muscle signals recorded by means of high-density surface electromyography

For the detailed analysis of brain activity, it is often necessary to observe the activity of single neurons. This is possible nowadays thanks to recording microprobes inserted directly in the brain. However, these probes often record more than one neuron activity and therefore, classification that assigns spikes to neurons that initiated them is a necessary step prior to further analysis. In surface electromyography recordings, signals that are observed are the summation of the activity of many muscle constituting parts - motor units. Being able to decompose these signals into contributions of individual motor units grants the ability to analyze muscle functioning and explore and track progress of various disorders.

These two distinct problems share a number of common signal processing features, and therefore similar algorithms are used for solving them (see Figure 1). The aim of this work is to provide solutions for reliable classification of neural signals and the decomposition of the recorded muscle signals. The emphasis is on creation of the automated and reliable signal processing algorithms that are highly desired due to the large amount of the recorded data.

The traditional neural signal spike sorting approach is extended by post-processing the classification output using the parameters described in Chapter 2 less prone

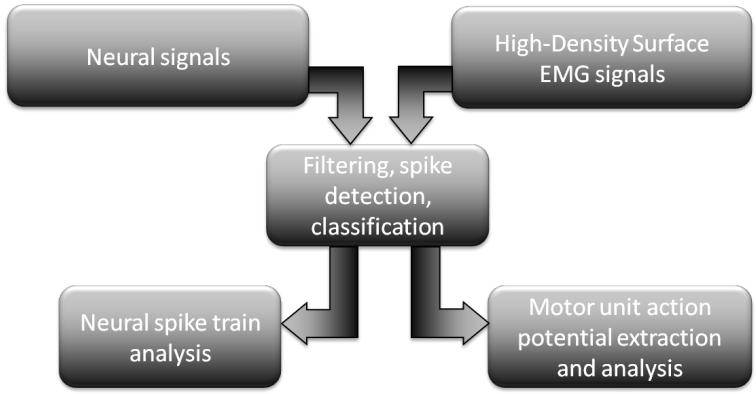

Figure 1: Outline of the thesis. On the one hand, neural signals are first conditioned followed by spike detection and classification; post-processing solutions for this output yields the automated signal analysis. On the other hand, first step in analysis of muscle signals recorded by high-density electrode grids is the detection and classification of spike-events (motor unit action potentials); this allows for further signal decomposition and manipulation of extracted spikes.

to classification errors and thus, achieve more reliable results. This strategy is later successfully applied in a study of obsessive-compulsive disorder described in Chapter 3.

High-density surface electromyography signals are a summation of many overlapping spikes from different muscle motor units and noise. In Chapter 5 a solution for decomposing this complex signal is presented and verified. Later, in Chapter 6, this decomposition solution is used as a first step followed by a new signal conditioning method for the purpose of facilitating the motor unit tracking problem - a tool of possible medical value for follow-up studies of various muscle disorders.

Chapter-by-chapter overview

Chapter 1 introduces the problem of neural spike signal analysis, starting from the description of signal recording and filtering to algorithms for the spike detection and classification. The concepts are explained with examples using neural signals for reasons of consistency. However, major signal processing steps in this chapter are common for both neural and muscle signal analysis.

Chapter 2 first examines the results of spike classification in case of low-quality signals. Thereafter, a set of known and new parameters for description of the spike-rate function (obtained as an output of the above mentioned classification) is introduced. Finally, a framework is provided for testing robustness and information-carrying potential of these parameters for better description of neural activity.

Chapter 3 uses the logic of parameter-assisted description of neural behavior in a study of obsessive-compulsive disorder (OCD). This study, aiming at providing new useful targets for deep brain stimulation for OCD treatment, is described. Results indicate the previously unknown role of bed nucleus of the stria terminalis (BST) brain area in this disorder.

Chapter 4 describes the technique for non-invasive surface recording of the muscle signals known as surface electromyography (sEMG). In addition, it describes high-density surface electromyography (HD-sEMG), a recently emerging EMG recording technique, which relies on densely spaced multielectrode arrays for data acquisition. The possibilities of this technique, as well as the challenges in data processing, are described.

Chapter 5 presents a novel algorithm for extraction of individual motor units' contributions to the recorded muscle signal, solving the problem of HDsEMG signal decomposition, needed for many research applications. The new algorithm is described and tested on simulated and real signals previously scored by trained operators.

Chapter 6 provides a new technique for compensating displacement discrepancies of the HD-sEMG recording grid. In current practice, these grids have to be placed very precisely in exactly the same position each time a new measurement is to be performed on a subject (patient), in order to conduct the so-called motor unit tracking. The proposed technique compensates for displacement discrepancies, thereby allowing arbitrary electrode placement which enables expanded applications of motor unit tracking. A pilot study is presented demonstrating the introduced concept on three healthy individuals.

Chapter 7 reviews the work presented in this thesis, and proposes directions for future research and exploration.

Collaborations

The work included in this thesis was initiated within the context of the KU Leuven collaboration with IMEC - Belgium. The joint work (in the scope of IWT SBO project BrainSTaR (01.01.2010-31.12.2013) and others) aimed to provide signal analysis for evaluation and use of new generation IMEC deep brain recording and stimulation microprobes. For this purpose, I was awarded an IMEC SLT 4-year scholarship. This collaboration introduced me to a number of people within the former BioNe/BES group in IMEC (now LST/CELL), who had great expertise and experience, which contributed greatly to this work. Namely Carmen Bartic and Wolfgang Eberle guided me as leaders of the microprobe development project through its goals and offered valuable insights. Through of daily collaboration and supervision, Dimiter Prodanov, Marleen Welkenhuyisen, Silke Musa, Thoa Nguyen and Carolina Mora offered invaluable insights and assistance. Bart Nuttin from the Experimental Neurosurgery and Neuroanatomy group clarified the medical perspective of deep brain stimulation, giving a context and reasons for these research efforts, especially the obsessive-compulsive disorder study.

In a later stage, an introduction to Joleen H. Blok from the Department of Clinical Neurophysiology, Erasmus MC Rotterdam (The Netherlands), led to additional research direction related to high-density surface electromyography. It was namely Joleen Blok and Hans van Dijk from the Department of Neurology/Clinical Neurophysiology (Donders Institute for Brain, Cognition and Behavior, Radboud University Nijmegen Medical Centre, The Netherlands) who pointed out major signal processing problems that needed to be addressed. Their expertise in muscle physiology and interpretation of the processing output was crucial for the development of algorithms presented here. Finally, cooperation with the student of Joleen, Boudewijn Sleutjes brought the new perspectives and challenges, leading to new promising solutions and perspectives for future collaboration, bringing medical practice and signal processing closer together.

Chapter 1

Introduction on spike sorting

This chapter introduces the concept of spike sorting, the main topic of the thesis. Description of the spike sorting concept is provided together with an overview of tools that are needed to detect and extract relevant information from the spikes. In particular, classification algorithm called the superparamagnetic clustering [10], [149] is described in detail. This algorithm is a key tool for a number of later applications in neural and surface electromyography signal analysis.

1.1 Spike sorting

Neurons are the building blocks of our neural system. Observing the activity and communication between individual neurons offers the finest spatio-temporal scale that allows e.g. detection of individual and global changes in neural activity, detection and localization of epileptic areas, investigation of correlations between movements and mental processes etc. Neurons communicate through exchange of electro-chemical information causing fast changes in potential over the cell surface. These fast transient changes in the electrical potential of the cell, called action potentials, travel along its surface and serve as the input to other neurons. Since action potentials appear only if a certain threshold needed for the change of cell polarity is crossed, they thought to represent the mean of binary, "all or none" way of communication between the neurons. These action potentials can be observed using an electrode placed in the vicinity of a "firing" neuron and are generally called spikes.

The relevant information of a spiking neuron is contained in appearance times of its spikes - spike timestamps. Obtaining timestamps is not an easy task in realistic experimental settings. The same electrode can record spiking trains of several

nearby neurons. The process of isolating individual spike trains is complex and is obtained through a chain of necessary processing steps: filtering of the signal; detection of spikes; and classification of spikes according to their putative neuron. This chapter presents an overview of these steps and focuses on the most important and still not fully resolved process of spike classification.

Spike sorting will be discussed in this thesis both for neuronal spikes as well as for electromyographic spikes called motor unit action potentials. For reasons of consistency, the rest of the chapter focuses on the spike classification done on neuronal spikes and the application in surface electromyography is discussed in Chapter 4.

1.2 Origin and recording of neural spikes

As previously stated, a neuron is an excitable cell that processes and transmits information by electrical and chemical signaling. Chemical signaling occurs via synapses, specialized connections with other cells. Neurons connect to each other to form neural networks. Neurons are the core components of the nervous system, which includes the brain, spinal cord, and peripheral ganglia. A number of specialized types of neurons exist: sensory neurons which respond to touch, sound, light and numerous other stimuli affecting cells of the sensory organs that then send signals to the spinal cord and brain. Motor neurons receive signals from the brain and spinal cord and cause muscle contractions. Interneurons connect neurons to other neurons within the same region of the brain or spinal cord.

A typical neuron possesses a cell body (called soma), dendrites, and an axon. Dendrites are thin structures that arise from the cell body, often extending for hundreds of micrometers and branching multiple times, giving rise to a complex "dendritic tree". An axon is a special cellular extension that arises from the cell body at a site called the axon hillock and travels for a distance, as far as 1 m in humans or even more in other species. It is often covered with a myelin layer. The main purpose of a myelin layer (or sheath) is to increase the speed at which impulses propagate along the myelinated fiber. The cell body of a neuron frequently gives rise to multiple dendrites, but never to more than one axon, although the axon may branch hundreds of times before it terminates. At the majority of synapses, signals are sent from the axon of one neuron to a dendrite of another via terminal buttons that are located at their end. A typical neuron with its constituent components is portrayed in Figure 1.1

All neurons are electrically excitable, maintaining voltage gradients across their membranes by means of metabolically driven ion pumps, which combine with ion channels embedded in the membrane to generate intracellular-versus-extracellular concentration differences of ions such as sodium (Na^+), potassium (K^+), chloride

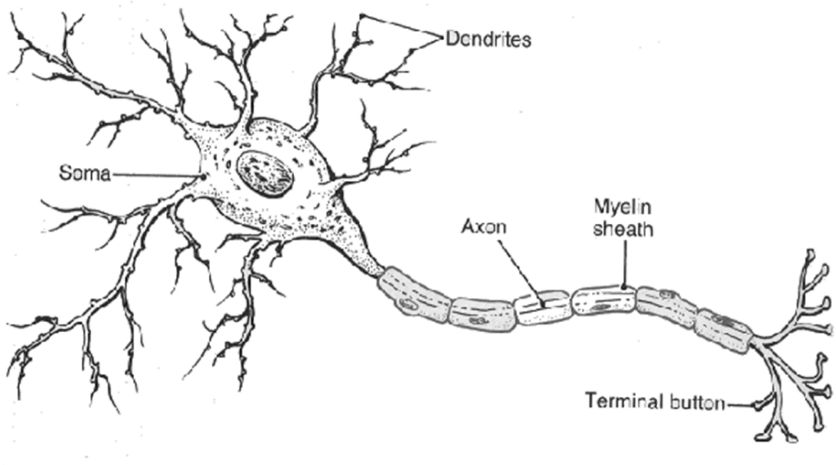

Figure 1.1: Neuron and its parts - soma, dendrites and axon. Adapted from [23].

(Cl^-), and calcium (Ca^{2+}). Neurons have a high concentration of K^+ and Cl^- ions inside and keep the Na^+ and Ca^{2+} ions outside. This creates a battery with a -60mV voltage difference between inner and outer cell space. Each cell's membrane is covered with pores allowing ions to travel in and outside of the cell. These pores can be opened and closed very quickly, thereby altering the flux of ions and consequently, the voltage difference. Small voltage changes are common but if they become large enough, they cause electrochemical pulse (spike) to appear and travel rapidly along the cell's axon also affecting (activating) synaptic connections with other neurons via release of a chemical substance, called neurotransmitter. Depending on the strength of these connections, these neurons can be activated as well. When a neuron "decides to react", the channel opening of the cell body (soma) at first occurs linearly with time and the voltage difference between inside and outside of the cell diminishes. However, after some critical amount of Na^+ crosses the cell membrane, it causes additional Na^+ channels to open, leading to exponential increase in its influx. This fast and nonlinear event causes the polarity of the cell to revert, leaving the inside at about +20mV potential. Pumping out the excessive Na^+ ions is lengthy, so a cell diverts to another strategy: as the action potential rises, the voltage-dependent K^+ channels are activated and they promptly repolarize the cell [90], [18]. This causes the falling phase of the action potential. This whole process lasts for about a millisecond limiting the maximum firing rate of a neuron. It is also a principal limitation on the speed with which the brain is able to process the data. Due to the fast nature of this process, the terms action potential and "spike" are used interchangeably by the investigators. Electrical potential change, as seen from the inside of the cell, is portrayed in

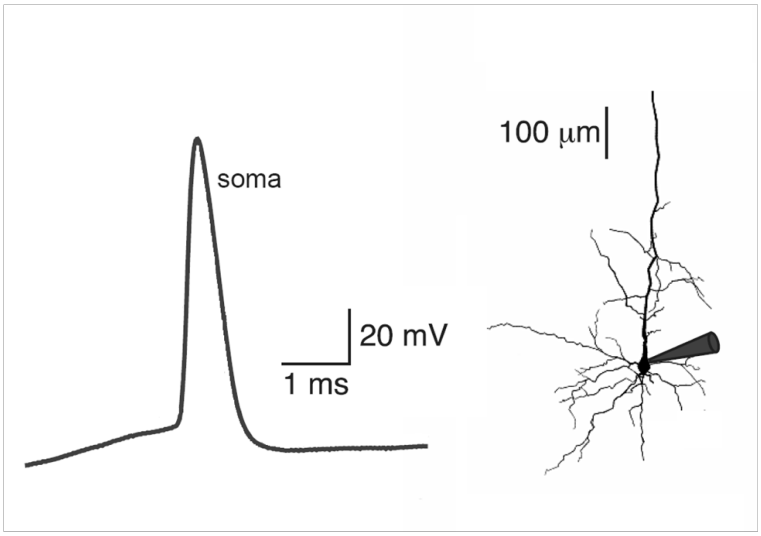

Figure 1.2: Neural spike recorded with an intracellular electrode. Spike is observed directly from the cell body (soma) measurement. From Haüsser et al. ([79]). Reprinted with permission from AAAS.

Figure 1.2.

In realistic in-vivo settings, it is technically difficult to use recordings from inside the neuron cell [186], requiring a lot of manual effort by a skilled operator (intracellular recordings achieved by so-called patch-clamping of the cell). Often, these settings rely on the extracellular recordings which are also the focus of this chapter. Recording in extracellular space is possible due to large transmembrane potentials caused by action potentials within a cell. Such an electrode has to be very close to the cell body (soma) because this recordable potential drops very fast with increasing distance from the cell. Naturally, while the inner cell body potential is in the millivolt range, its extracellular counterpart is only in the microvolt range (Figure 1.3). Modern micromanipulators are used to place electrodes with small tips (10-80 micrometer range) [67] in the region containing target neurons, but the rest is up to luck: precise targeting to one specific neuron is challenging and often not possible. The rationale supporting these seemingly random recordings is that a population of typical neurons would be observed, indicating the typical or changed activity in a particular brain region.

In often densely spaced neuronal regions, such as e.g. cortex, it is often the case that the electrode tip will record spiking activity from several neighboring neurons. Neurons of the same type sometimes have virtually indistinguishable

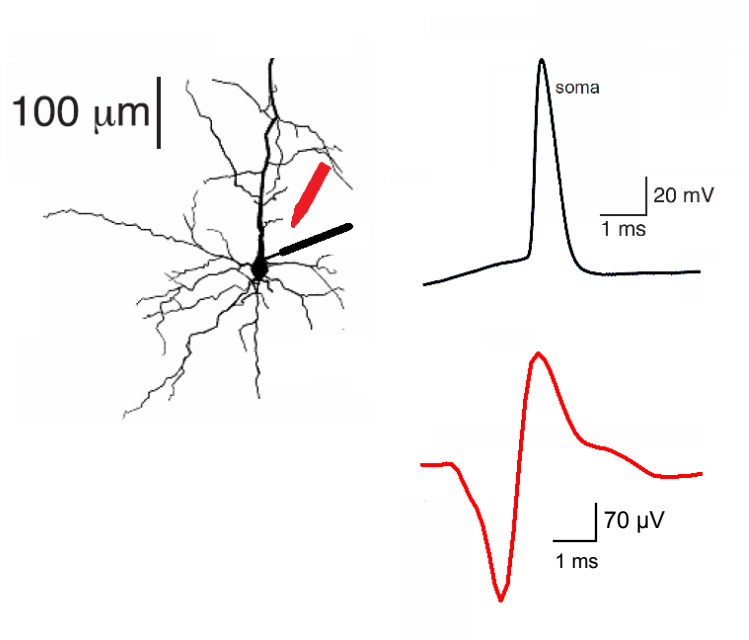

Figure 1.3: Intracellular (black) vs. extracellular (red) recording of a spike; toy positions of electrodes are indicated as well in respective colors.

action potentials when recorded from within the cell [18]. An approach allowing us to distinguish between neurons recorded extracellularly is based on the difference in relative geometry between the different neurons and the recording electrode. As the signal travels from the observed neuron to the recording electrode, it passes through the tissue which causes the spatial filtering effect. Therefore, different distances of close-by neurons alter the shape of the recorded spikes in a different manner which allows discrimination. Discrimination of different spikes according to the originating neuron is a necessary prerequisite to allow any further analysis of neural activity.

Spikes are not the only physiological signal that is present when performing extracellular brain recordings. Waves called the local field potentials (LFPs) are observed as well. LFPs arise largely from dendritic activity over large brain regions providing a measure of the input to and local processing within an area [99]. Hence, they are the linear sum of activity of many neurons, and are situated in the low frequency part of the spectra. Their role in brain is speculated to be one of synchronization, input to neural networks receiving and processing it by their own spiking activity. This synchronized neural activity in turn contributes to LFPs

contributing to the input for other neurons. A comprehensive study on LFPs is provided by Buzsaki and Traub [19]. LFP data is often used in studies aiming to correlate them with the spiking activity of neurons in an attempt to explain behavioral and other effects driving the brain.

Multichannel neuroprobes

First recordings of the single neuron activity were achieved more than half a century ago, using the, often custom made, microwires. These would be inserted in a target brain area. To be able to isolate spikes from single neurons, they had to have a tip size of $\leq 60\mu m$ order to avoid the pronounced "integration" effect of the nearby tissue electrical activity.

With the growing research "appetite" came the need to employ more recording sites and thus achieve higher resolution of the neural signals. This could be achieved by using more, densely spaced electrodes. The invention of the lithographically-based planar process, initially used for integrated circuits fabrication, offered the solution for this need. These lithographically-defined microelectrode arrays now allow for high-density recording and stimulation in the brain to facilitate new insights into organization and functioning of the central nervous system [177]. Another motivation for using the chip technology microarrays is related to their smaller size compared to single blunt microwires. This is reflected by a smaller damage of the tissue during the electrode insertion and increases the number of usable recording sites. However, the spatial relations of the microelectrodes cannot be altered later due to this process.

Naturally, the development of such probes presents a challenge and an iterative task, optimizing the device in each new step (generation). IMEC - Belgium (former BioNE/BES group) took this challenge producing so far two generations of these probes, having the third generation in the design phase. These probes were designed for tests with rodents (rats). Each specific step (design, processing, *in vitro* and *in vivo* characterization) was used to further optimize the device. Of course, all the neural microprobes development was followed by the development of the supporting electronic components, like amplifiers and printed circuit boards (PCBs).

Figure 1.4 shows the examples of first generation IMEC probes [177]. Without going into details about fabrication process itself, the following dimensions were chosen according to the current trends in modern microprobes: shaft length: 2 mm; width: 200 and 240 μm; thickness: 200 μm; tip angle: 90°; number of contacts: 10; diameter of the contacts: 10, 25, and 50 μm; contact material: Au or Pt. A temperature sensor was also included in the first generation to evaluate possible heating during stimulation or MR scanning, but abandoned in later generations due to sensor instability.

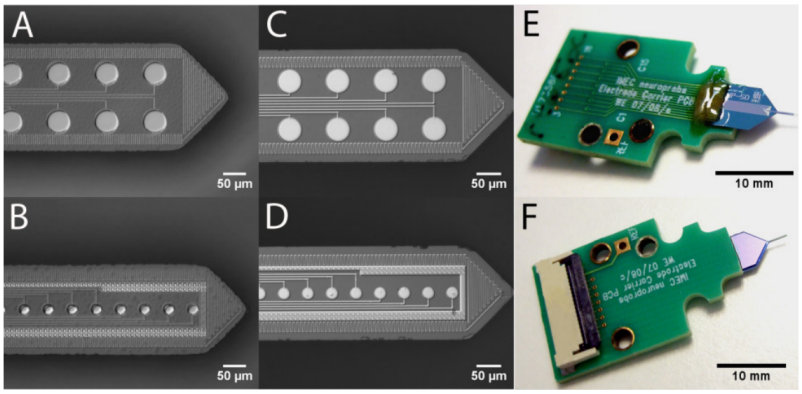

Figure 1.4: Optical micrographs of probe tip with Au contacts with diameter of 50 μm (a) and 25 μm (b) and of a probe tip with Pt contacts of 50 μm (c) and 25 μm (d) electrodes. Picture of the whole packaged probe, front side with contacts (e) and back side with Omron connector (f). Taken from [177], [130], ©IMEC, Belgium.

Second generation IMEC probes featured many processing adaptations using different materials and building upon experiences from the first generation devices. The second generation also aimed to make the probes thinner, miniaturize PCBs and make universal, easily accessible connectors. The dimensions of the probe itself were: a shaft length of 2 or 10 mm to reach all brain structures in the rat; a width of 200 μm; a reduced thickness of 100 μm; a sharper tip angle of 20°; and an increased number of contacts (n = 16). The diameter of the contacts remained 10, 25, and 50 μm and the contact material was Pt or TiN. Figure 1.5 shows the example of the second generation IMEC microprobes. Recordings made by these two generations of IMEC probes were analyzed in the course of this doctoral program.

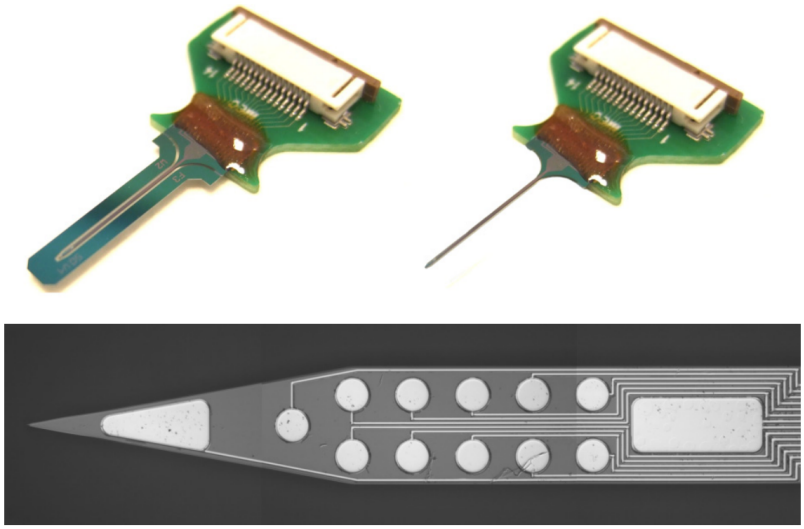

Figure 1.5: Pictures of the packaged second generation probe with an Omron connector and a long shaft (10 mm) with protection (top left) and without protection (top right). Optical micrographs of probe tip with 50 μm Pt contacts (bottom). Taken from [177], [129], ©IMEC, Belgium.

1.3 Signal filtering

In order to detect and analyze spikes, the recorded signal first has to be conditioned. For this, the structure of neural signals needs to be examined first. In the recorded signal, spikes appear as fast, transient events. Hence, in order to secure their proper reconstruction, usually sampling frequencies of around 20kHz have to be employed. However, a recorded signal has several components: spikes, LFPs and the background noise, again consisting of physiological noise (coming from relatively far neurons), and instrumental noise which is present in every recording and assumed to be random. Additionally, various artifacts can appear in measurements as a result of electrical interference (e.g. higher harmonics of the power network) or simply instrumentation imperfections like electrode drift or others, sometimes causing artificial "spiky-like" artifacts that need to be automatically or manually excluded from the analysis.

LFPs are usually considered to occupy part of the spectra between 0 and 300 Hz [150]. As slow waves, they are less affected by the low-pass filtering effects of the tissue and travel farther. In the course of sole exploration of neural spikes, LFP bandwidth is filtered out mainly due to the fact that its power is at least an order

of magnitude stronger than the power of spikes thereby making them less visible. Another reason is that spikes are mainly occupying the higher part of the frequency spectra and thus, from the perspective of spike analysis, LFPs can be considered as noise.

Instrumental noise is often assumed to be corresponding to a random Gaussian process. This assumption does not always hold and the noise is somewhat correlated (colored). This means that there is a prediction probability of a sample n based on previous samples $(n-1, n-2, ...)$. It has been shown [7] that signal prewhitening (decorrelation) improves spike detection SNR values. Therefore, using a filter that decorrelates (prewhitens) the signal (e.g. one proposed in [13]) improves the detection and classification. Decorrelation of the signal is achieved by "rotating" the coordinate system - finding a signal projection that provides white instead of colored noise. One way to achieve this used in [7] is to employ an autoregressive moving average (ARMA) model of noise. The inverse of this model provides a whitening filter to be employed.

Instrumental, random noise often cannot be filtered out. This is due to the fact that it is spectrally evenly distributed, overlapping the spiky-band. It is the limiting factor defining signal-to-noise ratio (SNR) and limiting the ability to discriminate spikes.

Spikes roughly cover the range between 300 Hz and 5 kHz [76]. Prior to detection and classification of spikes, it is thus necessary to perform high-pass filtering. Butterworth highpass filter or ellipsoid filters are usually sufficiently good choices since there is no strict requirements on the filter slope - very little information is lost by attenuating frequencies close to the LFP frequency range. Filtering the signal is portrayed in Figure 1.6: a) shows the raw signal; LFP signal obtained by low-pass filtering is shown in Figure 1.6 b) and the relevant signal containing spikes is depicted in Figure 1.6 c).

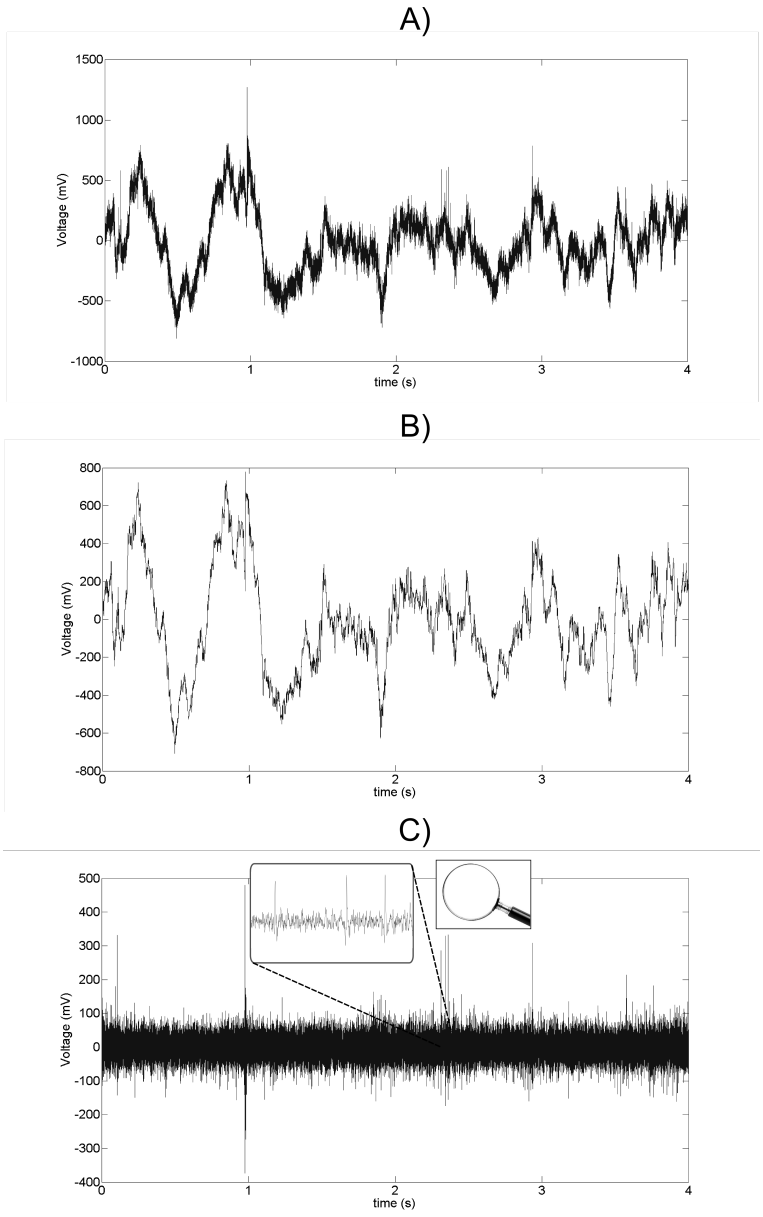

Figure 1.6: Filtering as a preprocessing tool shown on a 4s signal recorded in human medial temporal lobe reported in [155]; a) raw signal; b) low-pass filtering yields LFPs; c) high-pass filtering provides conditioned signal for spike detection and classification; magnified part shows 3 spikes appearing in a signal

1.4 Spike detection and alignment

1.4.1 Spike detection

In practice, the signal measured with extracellular microelectrodes is corrupted by noise composed of several sources: remotely located neurons, measurement noise and various artifacts. Extracting the neuronal activity from this noisy signal is referred to as spike detection. The goal of spike detection is to obtain as many real spikes (true positives) while keeping the level of detected non-spike events low (false alarms). Several techniques have been applied towards this goal.

Amplitude thresholding

Most common methods for spike detection are based on amplitude threshold crossing. Events that are above the suitable threshold are flagged and represent candidates for spikes. A suitable threshold is in general some predetermined multiple of the estimated noise level [151]. However, in the presence of spikes, estimation of this noise level is nontrivial. The simplest methods avoid this by manual threshold setting by a researcher using visual feedback of a filtered signal [111]. Although successfully used in the past, this has become obsolete due to the larger number of electrodes employed recently, making it time consuming and impractical.

The simplest way to estimate the noise level is to put it as the standard deviation of the signal itself. However, this estimate is strongly biased in the presence of spikes leading to an over-estimation of this level [149]. A more robust method, relying on median distribution of the signal absolute value, is presented in [149]. Since it is known that this median value in case of Gaussian noise is $0.6745\sigma_n$, where σ_n is the standard deviation of Gaussian noise, one can take the estimate of the noise standard deviation as:

$$\sigma = median\left\{\frac{|(x(t)|}{0.6745}\right\} \tag{1.1}$$

where $x(t)$ is the measured signal itself. It has been shown that this measure is considerably more robust in the presence of spikes and/or high-amplitude artifacts [47]. An even more robust measure of noise relies on using a signal envelope, and finding the peak of its sample distribution values (mode function) [45].

These and other operators all tend to find a measure of noise standard deviation. This measure is then multiplied with a fixed value to obtain a threshold for spike

detection. Finding the optimal multiplier value was the subject of separate studies (e.g. [151]). Its optimality is measured by detecting as many spikes in a wide range of conditions - different number of spike shapes (waveforms) and firing rates, while having as little false alarms as possible.

Energy operators

A second class of detection methods relies on first transforming the signal to emphasize the difference between spikes and background noise before applying a threshold for detection. Spikes are fast events corresponding to higher than usual energy and therefore, using operators that favor high energy helps reveal them easier. The simplest energy operator is the Squared Energy Operator (SEO) defined as:

$$S(x(t)) = x^2(t) \tag{1.2}$$

Sometimes, a running average version of this operator is used as well. It is defined as:

$$S_1\left(x(t)\right) = \frac{1}{n}\sum_{i=1}^{n}\left(x(t-i) - \bar{x}(t)\right)^2 \tag{1.3}$$

$$\bar{x}(t) = \frac{1}{n}\sum_{i=1}^{n} x(t-i) \tag{1.4}$$

Here, n is the number of samples that corresponds to the spike length that is well estimated in the past (e.g. [109]).

Another energy-based operator is the so-called Non-linear Energy Operator (NLEO or NEO) also known as Teager-Kaiser Energy Operator (TEO). It is defined as:

$$\psi\left(x(n)\right) = x^2(n) - x(n+1)x(n-1) \tag{1.5}$$

It can be shown that:

$$\langle\psi(n)\rangle \approx \langle A^2(n)\rangle\langle\Omega_x^2(n)\rangle \tag{1.6}$$

where $\langle\rangle$ denotes a time average, $A(n)$ corresponds to signal amplitude at sample n and $\Omega(n)$ to the signal frequency. It is clear that both the amplitude and frequency content are emphasized by this operator. Since spikes are spread out in the frequency domain and exhibit a higher amplitude, this operator proved very useful even in cases of below 0dB SNR for detection of spikes [92]. NLEO is also shown to outperform SEO for short time periods close to spike length [42],[139] making it a very useful transformation tool.

Wavelets

Another appealing way to increase the difference between spikes and background noise is to use the discrete wavelet transform (DWT). Recently, it has become increasingly popular due to ease of use and more importantly, the possibility of fast implementation on the hardware level. A wavelet ψ ($\psi \in R$) is a continuous function of finite energy and has a zero mean:

$$\int_R \psi(t)dt = 0 \tag{1.7}$$

It is additionally normalized ($\|\psi\|_2 = 1$). This function, also called a mother wavelet, can be scaled and translated:

$$\psi_{a,b}(t) = \frac{1}{\sqrt{a}}\psi\left(\frac{t-b}{a}\right), a, b \in R \tag{1.8}$$

where $a > 0$ represents the scale and b is translation.

The wavelet transform of a signal $x(t)$ is a projection of this signal onto the wavelet basis:

$$Tx(a,b) = \int_R x(t)\psi_{a,b}(t)dt \tag{1.9}$$

For a fixed scale (a) and translation (b), the wavelet transform of a signal x represents its resemblance index to the wavelet $\psi_{a,b}$. If this index is large, resemblance between the wavelet and the signal at this instance is high [133]. The requirements on wavelet properties enable definition of a whole group of functions, some of which resemble well the spike shape itself. Wavelets can thus "capture" fast transients (as spikes) by projecting the signal on a transformed wavelet

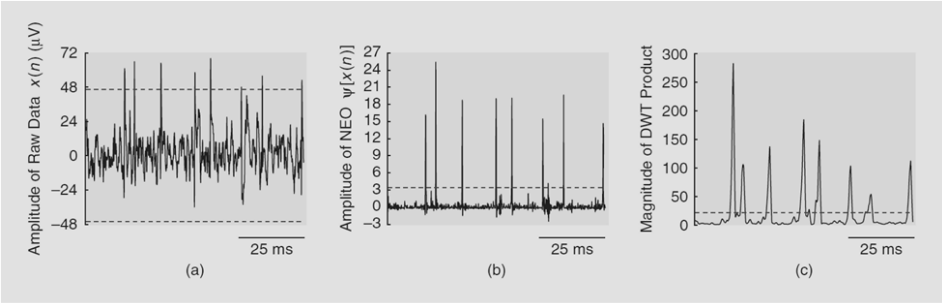

Figure 1.7: Examples of pre-emphasized signals and threshold values (dashed red lines) for three different detection methods. (a) Absolute value, (b) NEO, and (c) DWT product [93], reprinted with permission © [2012] IEEE

basis. Often, a set of discrete scales and translations is applied to obtain signal decompositions on several levels, defining a discrete wavelet transform (DWT). Various techniques then identify sets of higher coefficients that correspond to spikes easing their detection. Some examples of using DWT for spike detection include [110], [159], [93] and others. Comparison of detection transforms including amplitude detection, NEO (NLEO) and DWT are portrayed in Figure 1.7 taken from a recent comparison study ([67]).

1.4.2 Alignment

Once spike events are detected, the waveform of each action potential is extracted from the data. An optimal data window is extracted around each spike event.

Before the waveforms are clustered, they need to be correctly registered with one another. The comparison of voltage values for different instances of an action potential from the same cell is sensitive to the temporal alignment of the two waveforms. It is common but often inappropriate to align spike events on the threshold crossing found in spike detection. The more reliable method is to align spikes with respect to their positive or negative peak.

Even so, the precise moment at which an analog voltage trace corresponds to this peak will in general occur between two consecutive samples. The first sample recorded above threshold then lags the actual crossing by a duration between 0 and $1/f_s$ (where f_s is a sampling rate), and the extracted samples for the entire waveform are equally shifted in time. This process causes two identical waveforms to appear different even in the absence of noise. Background noise compounds this

effect by randomly advancing or delaying the actual peak crossing for each event, possibly by multiple samples.

One solution to misalignment is to digitally upsample the data. When electrophysiological signals are sampled at more than twice the Nyquist frequency, the sampled waveform has all the information needed to reconstruct the continuous analog signal (that is one of the reasons of using the high sampling rate in the first place). Interpolation between samples increases the effective f_s and yields an alignment with a higher temporal resolution. After an improved alignment is found, the data can be downsampled to retain the original dimensionality of the spike waveforms. Figure 1.8 shows a set of detected spikes before (a) and after (b) alignment. Seemingly not much different, average spike shape (Figure 1.8 c)) shows that also the main peaks of the spike are affected. This in turn affects the later discrimination justifying this approach.

1.5 Spike classification

Isolating the recorded spikes is only a first step towards spike-train analysis. The term "spike sorting" is usually associated with the process of classification of neuronal spikes with respect to putative neuron. The whole procedure, ranging from raw signal, its filtering, spike detection and alignment, feature extraction and finally clustering, is portrayed in Figure 1.9. Various approaches to the spike sorting were seen in the past decades. A thorough overview is provided in [111]. The usual procedure first aims for dimensionality reduction (or feature extraction) that eases the classification. Then, classification (or clustering) is performed on vectors of these features representing each spike to obtain spike trains.

1.5.1 Feature extraction

The assumption behind the spike classification is that spikes originating from different neurons will have a different shape. Based on this, spikes from the same class will exhibit large intra-group similarity. In reality however, spike shapes can be rather similar. One example of 2 overlaid spike shapes is portrayed in Figure 1.10. Using complete spike shapes as inputs to the classifier will be sub-optimal in cases like this where spike shapes are very similar on a number of samples. These samples practically do not contribute discriminatory information and reduce the quality of classification. Ways to increase the importance of discriminatory samples are common practice in recent approaches. Sometimes, sophisticated features are used that need not be physically interpretable and are therefore difficult to understand. Here, spikes are first transformed with respect to the new basis and the resulting coefficients are then analyzed. Identifying and extracting discriminatory

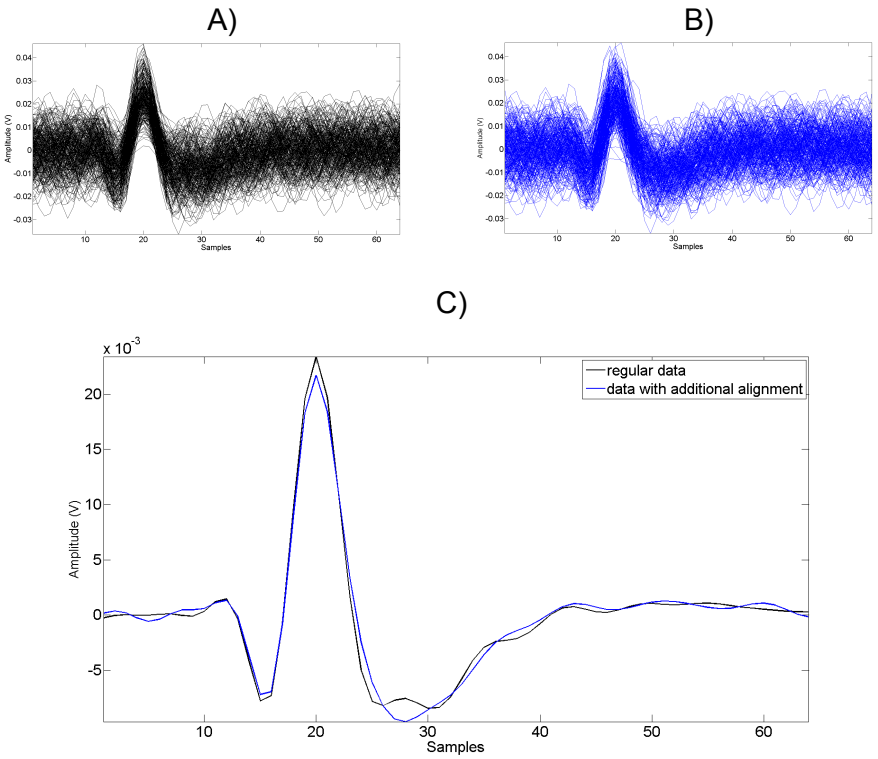

Figure 1.8: Simulation using the known spike shape shows (a) regular and (b) alignment after prior signal upsampling. Mean spike shape is better preserved when the alignment is preceded by upsampling, which can be observed in (c).

features has been the topic of many past studies. Most frequent approaches are introduced.

Simple features

In early days of spike classification, easy but effective features were used. These came from intuitive notions from observing spikes. For instance, each spike can be represented by its maximum amplitude, peak-to-peak amplitude, spike width or a combination of these [111].

Principal components

With the increased performance of computers, researchers began to use more sophisticated techniques such as Principal Component Analysis (PCA, [89]). Here, the orthogonal basis of the recorded spikes is changed. The new basis or "principal

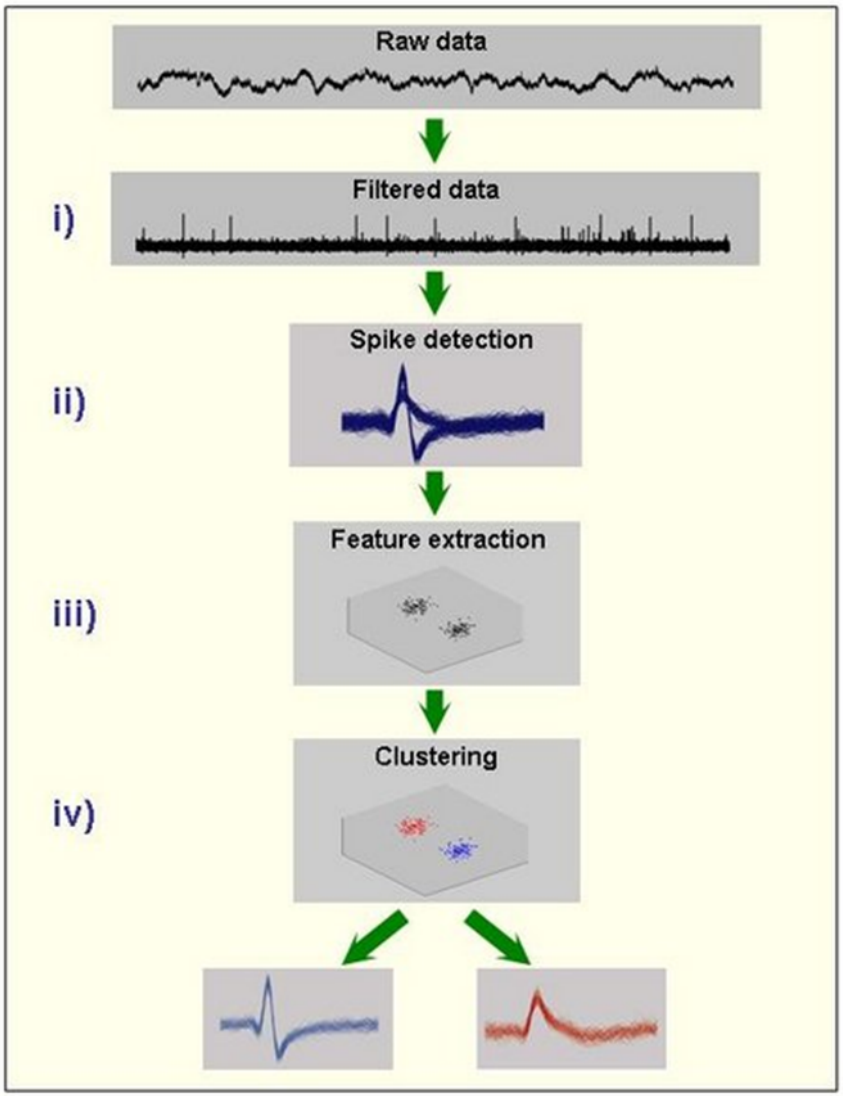

Figure 1.9: Four main steps in spike classification: filtering, spike detection, feature extraction and classification [149]. © 2004, Massachusetts Institute of Technology.

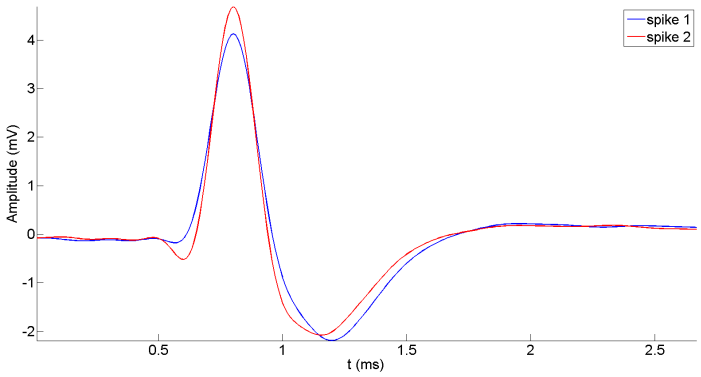

Figure 1.10: Two similar spikes (blue and red) originating from different neurons. Note that these are average (noiseless) shapes. Data from study [178].

components" is extracted in a way that favorize the directions in the data with the biggest variation. This is done by performing the eigenvalue decomposition of the covariance matrix of the stored spikes. Then, a spike c projection at each principal component i (PC_i) can be represented by a coefficient c_i that represents a future classification feature:

$$c_i = \sum_{n=1}^{N} PC_i(n)s(n) \tag{1.10}$$

Here, $s(n)$ represents a spike sample (where N is a spike length). These coefficients are then used for clustering (e.g. like in Figure 1.9 iii)).

Usually, most signal variance is contained within the first PCs and thus, computation time for coefficients can also be reduced. Although it is nowadays very common and arguably one of the best methods for feature extraction prior to clustering, the PCA method has several flaws. First, it is not an online method since all events (spikes) have to be extracted prior to eigenvalue decomposition. Secondly, sometimes in cases of very similar spikes, it cannot be determined in advance which combination of PCs will show the highest between-clusters difference.

Wavelets

DWT as a multiresolution technique represents another possible choice for selecting features. It preserves both time and frequency content and can reveal distinct properties used for later discrimination. DWT can be used to expand each spike

into some predetermined set of scales for any chosen mother wavelet. The expansion coefficients can be used afterwards as features in the same manner as with the PCA.

1.5.2 Feature reduction and classification

Spike classification or sorting is the last but most important step in obtaining neural spike trains. Usually, it is applied to the features extracted from the detected spikes. Spike sorting algorithms can be divided with respect to the global methodology and the automation achieved.

Feature reduction

Naturally, not all of the features extracted from the detected spikes are as important for classification. While some of these can have very different values and offer discrimination, others might not show any significant difference for "naturally" different spikes. Thus, finding these discriminatory features is highly desirable. Moreover, by taking fewer features, the computational effort needed for classification is decreased. Even the early spike classification methods recognized this need. The first feature reduction was done on visually selected samples based on detected spikes using the so-called window discriminators, Figure 1.11. Every spike was represented by a few most discriminating samples and if a spike had a roughly expected value simultaneously in all windows, it would be assigned to a cluster.

Early approaches used to select most obvious features like the mentioned positive and negative peak amplitude, spike width or peak-to-peak amplitude. Sophisticated methods dealing with arbitrary features, tend to reduce their number by selecting those that can best separate clusters. One such way is to apply Lilliefors test ([113]) which is a modification of the Kolmogorov-Smirnov test [118]. The idea is that a selected discriminatory feature will not pass the tests null hypothesis that the data comes from a normally distributed population. Given a set of feature values x (each spike contributes one value per feature), the test compares the cumulative distribution function of this set ($F(x)$) with that of a Gaussian distribution of the same mean and variance ($G(x)$). Then, the deviation from normality is described as ([149]) $|F(x) - G(x)|$. A number of the features (dictated by the user) that exhibit the largest value of this deviation can then be selected for classification. This way of feature selection was also used throughout this thesis. The number of features varied depending on the application.

Another choice exploiting the same idea is the use of Hartigan's dip test ([77],[78]) that specifically searches for multimodality.

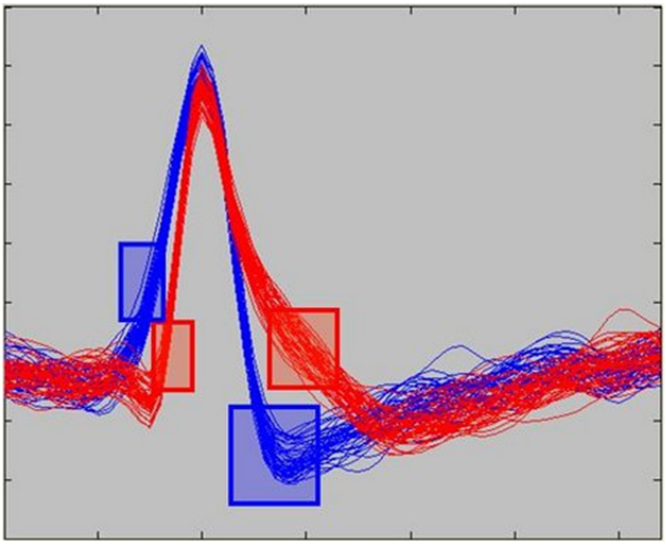

Figure 1.11: Window discriminators; rectangular windows are defined by experimenter following the detection and alignment of spikes; each spike class is associated with several (e.g. two) windows; spike is assigned to a cluster if it has sample values within all the windows of its class.

Classification

As stated previously, the goal of classification (clustering) is to assign each detected spike to its putative neuron. This is achieved based on the assumption that spikes originating from the same neuron are similar and different than spikes from other neurons.

However, the main problem with clustering is that there is no universal definition of the term cluster, mainly due to the inherent subjectivity of clustering, which precludes an absolute judgment as to the relative efficacy of all techniques [8], [9], [75]. Nevertheless, a cluster can intuitively be described as a set of data objects that are similar to each other, while data objects in different clusters are different from one another [185]. It is clear that the efficacy of clustering will largely depend on prior knowledge on the data to be clustered. This knowledge will impose criteria that will set the borders of what can be considered to be a cluster, as well as limits of allowed mutual variability of intra-cluster elements.

Clustering techniques can be categorized according to the level of automation as manual (supervised), automated (unsupervised) or a variant of these (e.g. semi-supervised, semi-automated) [67]. While manual techniques rely on constant

supervision by an operator, automated are fully autonomous. Interventions by the operator can be in reasigning the elements to clusters, setting the threshold for detection, determining the number of clusters and so on.

Methods for spike sorting can also be divided by type into 2 major categories: partition-based and hierarchical. Partition clustering can be further split up into hard partition and fuzzy clustering.

Consider a set of n d-dimensional data objects $\mathbf{X} = \{x_1, x_2, ..., x_j, ..., x_n\}$, where $x_j = (x_{j1}, x_{j2}, ..., x_{jd}) \in \Re^d$, with each measure x_{ji} called a feature [185]. The goal is to define sets C_i, which contain similar elements x such that $\cup_{i=1}^{K} C_i = \mathbf{X}$. Sets C_i then represent clusters of data. Note that determining a number of sets K is not straightforward and represents an important and largely unresolved issue.

Hierarchical clustering

Hierarchical clustering attempts to create a tree-like nested structure partition of $\mathbf{X}$, $H = \{H_1, ..., H_Q\}(Q \leq N)$, such that $C_i \in H_m, C_j \in H_l$, and $m > l$ imply $C_i \subset C_j$ for all $i, j \neq i$, $m, l = 1, ..., Q$. In other words, hierarchical clustering takes the whole data set and divides it into subgroups. The depth of this division which is subject to tuning will provide adequate clusters. Naturally, all elements must be available before the clustering is applied and thus, strictly speaking, hierarchical clustering cannot be implemented online.

Partition clustering

Hard partitional clustering seeks a K-partition of $\mathbf{X}$, $C = \{C_1, ..., C_K\}(K \leq N)$, such that

1) $C_i \neq \emptyset, \quad i = 1, ..., K$
2) $\cup_{i=1}^{K} C_i = \mathbf{X}$
3) $C_i \cap C_j = \emptyset, \quad i, j = 1, ..., K$ and $i \neq j$.

Hard partitional clustering tends to separate the data set $\mathbf{X}$ into K clusters, where K is a predetermined number. It usually achieves that by finding the best "cluster centers". Cluster centers are the points that globally minimize the distance between them and cluster members (data set X). Typical example is the $k - means$ algorithm [116] and its numerous modifications. The algorithm solves the problem by first randomly assigning cluster centers and modifying them to match the global minimization criteria in an iterative way.

Fuzzy partitional clustering

When the boundaries of clusters are not clear, it is useful to associate each data point with more than one cluster. After the clustering, even hidden relationships

between given data might be discovered. Usually, clusters are formed using a highest *a posteriori* probability. The clustering associates each data point x_i with each cluster j, giving it a degree of membership (probability) $u_{i,j} \in [0, 1]$ [185]. Two constraints are naturally imposed:

1) $\sum_{j=1}^{K} u_{i,j} = 1, \quad \forall i,$

which assures the same overall weight for clusters, and

2) $0 \leq \sum_{i=1}^{n} u_{i,j} \leq n, \quad \forall j,$

which takes care there are no empty clusters.

In neural clustering , one other characteristic appears important: whether the algorithm can perform real-time (online) or not. Real-time performance is closely related to the type of clustering algorithm but also to the classification features and detection method. For instance, for the usage of principal components, all spikes need to be available prior to feature extraction, making it an offline choice regardless of the clustering algorithm.

1.5.3 Variability of the spike shape

So far, the provided descriptions assumed the constant shape of the spikes stemming from a single neuron. While this may be sound in theory, practical measurements reveal difficulties related to this assumption. For one, after the microelectrode insertion, the surrounding tissue reacts in time by slow "relaxation". This changes the relative position of the electrode and the observed neuron and thus, the spike shape. Even if the neuron remains close-by (micromovements in the order of several μ m) and classifiable, clustering algorithm can in time fail to assign incoming spikes to the same neuron and rather form a new cluster. From statistical point of view, where many neurons are observed simultaneously to observe ensemble changes,this may not represent a big problem. However, if specific neuronal type is of interest (e.g. grid or place cells) things get more complicated. This problem is a common phenomenon in acute recordings. Nenadic and Burdic [134] conducted a study indicating the stable recordings lasting up to 1.5 hours (tissue relaxation constant). They used the quality metrics based on the spike peak-to-peak amplitude to determine automatically when the shape changes become too high for a successful tracking of a neuron. One possible alternative would be to employ algorithms able to account for gradual evolving of the average spike shape. Then, taking into account the tissue relaxation constant, the average spike shape would be modified to enable prolonged recordings. This has not yet been done, but the clustering

algorithm introduced in the following section offers one possible tool that would enable this.

1.6 Superparamagnetic clustering algorithm

Parametric clustering approaches assume some prior knowledge of clusters' structure (e.g. the number of clusters or distribution of its elements). It is then common to incorporate these assumptions in a global criterion whose minimization partitions the data and thus, achieves the clustering. This global criterion can be variance minimization, Gaussian mixtures fitting and so on. Furthermore, most of the clustering techniques will cluster any data provided to them, regardless of physical meaningfulness. Finally, the task of providing the number of clusters upfront to the clustering algorithm is embedded in most of these approaches and presents a nontrivial task.

The main problems associated with the clustering of neural spikes and motor unit action potentials from muscles are slowly changing shapes of spikes and the unknown number of clusters (ranging from 0 on). For example, changing (evolving) shapes of cluster elements would bias any approach relying on a fixed cluster center and diminish the performance of classification. On the other hand, the number of clusters provided as an input to many algorithms can crucially affect the outcome of classification. This prompted us to consider classification solutions that go around these problems avoiding parametric approaches that assume structure and the number of cluster classes. Therefore, we opted for the use of the non-parametric, hierarchical superparamagnetic clustering algorithm introduced in [10] and employed for spike sorting in [149] and its further adaptation. We did so because it showed low sensitivity to initialization, ability to correctly handle variability in spike shapes and noise resilience. The term noise in this context refers both to detected shapes that are not real spikes and overlapping spikes. The algorithm is able to leave out these shapes not affecting its performance, and estimates the number of clusters automatically, which is crucial for our stated goals.

1.6.1 Outline of the algorithm

The algorithm idea is borrowed from statistical physics models of magnetic particles. The problem of data clustering is transformed into that of finding the probable states of an inhomogeneous Potts model [10]. Here, every particle has a spin whose states are observed. Three regions of interest include: ferromagnetic stage, where the energy, represented by temperature T, is very low and thus, particle spins change together (highly ordered state); paramagnetic stage, where the temperature

is very high and spins are switched randomly regardless of particle interaction; and the so-called "superparamagnetic" stage, with in-between temperatures where only spins of grouped particles will change together. It is the goal to reach and observe this stage. Each spike is represented as a point in a D-dimensional space (assuming D pre-selected discrimination features). Particles (points) having the same spin orientation (same state) and high interaction strength are expected to belong to the same cluster. These interactions strengths are dependent on the proximity of particles. The concept of nearest neighbors circumvents the reliance on the cluster center and enables much faster calculations in a later, Monte-Carlo simulation stage.

1.6.2 Variables of the model

In this model, all the cluster elements are to be treated as particles, each having a spin value as its main property. Energy of the system will control the number of possible spin states. At each energy level, particles having the same spin value will be considered as belonging to the same group (cluster). Consider x_i to be a point representing the i-th detected spike in a D-dimensional space. Each point will be assigned a state - spin ($x_i \rightarrow s_i$), like in ferromagnetic Potts models. The spin variable s will be allowed to take one of the q integer states ($s_i \in 1, ..., q$). Each pair of points is connected by the interaction strength (cost function) defined as follows:

$$J_{ij} = \begin{cases} \frac{1}{K} exp\left(-\frac{d_{ij}}{2a^2}\right) & \text{if } x_i \text{ is a nearest neighbor of } x_j, \\ 0 & \text{otherwise.} \end{cases} \tag{1.11}$$

Here, K is the number of nearest neighbors and a is a distance constant. Both of these measures will be discussed later. d_{ij} is a distance measure between points, e.g. in the case of Euclidian distance $d_{ij} = \|x_i - x_j\|^2$.

The energy of this system is given by its Hamiltonian:

$$\mathcal{H}(s) = \sum_{<i,j>} J_{ij} \left(1 - \delta_{s_i,s_j}\right) \tag{1.12}$$

$< i, j >$ denotes neighboring sites. δ_{s_i,s_j} is a Kronecker delta function that has the value 1 when spins s_i and s_j are equal and 0 otherwise. We can obtain the average value of each physical quantity A at a temperature T as:

$$\langle A \rangle = \sum_s A(s)P(s), \tag{1.13}$$

where $P(s) = \frac{1}{Z} exp(-\frac{\mathcal{H}(s)}{T})$ represents the probability density function for each spin configuration s with a normalization constant $Z = \sum_s exp(-\frac{\mathcal{H}(s)}{T})$. This is relevant because it introduces ways to estimate probability of state change of nearest neighbors.

Two important quantities for the model are magnetization m and its variance describing parameter, susceptibility χ:

$$m(s) = \frac{qN_{max}(s) - N}{(q-1)N}, \qquad \chi = \frac{N}{T}\left(\langle m^2 \rangle - \langle m \rangle^2\right) \tag{1.14}$$

N is the total number of input points and $N_{max}(s)$ denotes the maximal number of points having the same spin value.

The importance of these parameters is following: while Monte-Carlo simulations will insure the stable state of particles with the same spin (clusters) for each temperature T, χ will pinpoint the borders of the superparamagnetic region from where the results of clustering will appear.

1.6.3 Iterative procedure and achieving the clustering

For each temperature value T, all particles are first assigned random spin creating a state s. Then, we will attempt to assign each point x_i a new spin, creating a state s_{+1}. The probability that its nearest neighbors will also change their state to s_{+1} is:

$$p_{ij} = 1 - exp\left(-\frac{J_{ij}}{T}\delta_{s_i,s_j}\right) \tag{1.15}$$

The important thing about this iterative step is the following: those nearest neighbors of x_i that had the same previous state s are only allowed to change the state altogether to a new, same value defined in s_{+1}. This defines a growing group of particles with the same state that is not allowed to change it independently in the next iteration. This frontier is allowed only to change state together. Iterations

of new random states are repeated until no (or little) changes are observed, thus forming the clusters.

Since we have a stable state (clusters) for all temperatures T, the problem comes down to finding a superparamagnetic region where natural clusters are expected to appear. This is done by observing the function χ. A toy example in Figure 1.12 a) shows the data that was successfully clustered. Figure 1.12 b) shows the function χ that assisted in locating the borders of the superparamagnetic region. Borders are easily determined as places of sharp transition and the sufficiently good results are obtained by taking the average temperature between the left and the right border.

1.6.4 Influence and setting of parameters

Performing Monte-Carlo simulations, assigning spins and deriving the function χ which provides the clustering outcome, relies on defining a set of parameters: number of possible spin states (q), temperature (T) range, particle distance constant (a) and the number of nearest neighbors (K). Their choice had only limited logical justification, while the rest was the result of empirical analysis and tuning. For the purpose of classification of neural signals, the values as well as the influence of these parameters is discussed.

The number of nearest neighbors, K, should grow with the dimensionality of the problem, however, values $5 \leq K \leq 20$ are found to be sufficiently good and small variations did not show large changes in the clustering outcome [10]. The distance parameter a needs to favor close to distant points and was taken as the average of the nearest neighbor distance. The shape of the cost function J_{ij} proved to be of little influence, as long as it decays fast (exponentially) with the distance between points.

Major influence comes with varying the value T. For purposes of spike classification, T was varied between 0 and 0.25 in steps of 0.01. Changing the spins and using the iterative procedure raises the need to observe the average value of point to point correlation $\left\langle \delta_{s_i,s_j} \right\rangle$. If this value is above a threshold θ, particles can be considered as belonging to the same cluster. A value of $\theta = 0.5$ was selected as in [149]. Finally, the number of possible states (q) was put at 20, slightly exceeding the maximally achievable number of observable neurons. The number of iterations was found by us to be of practical importance. Although a high number (e.g. 500) ensures best results, it also significantly affects the execution time. Depending on the application (e.g. neural or motor unit action potential clustering), we found the figure of about 300 Monte-Carlo iterations sufficiently good.

Superparamagnetic clustering allows to obtain good results with absolutely no interaction from the user apart from the initial tuning of the parameters. Its

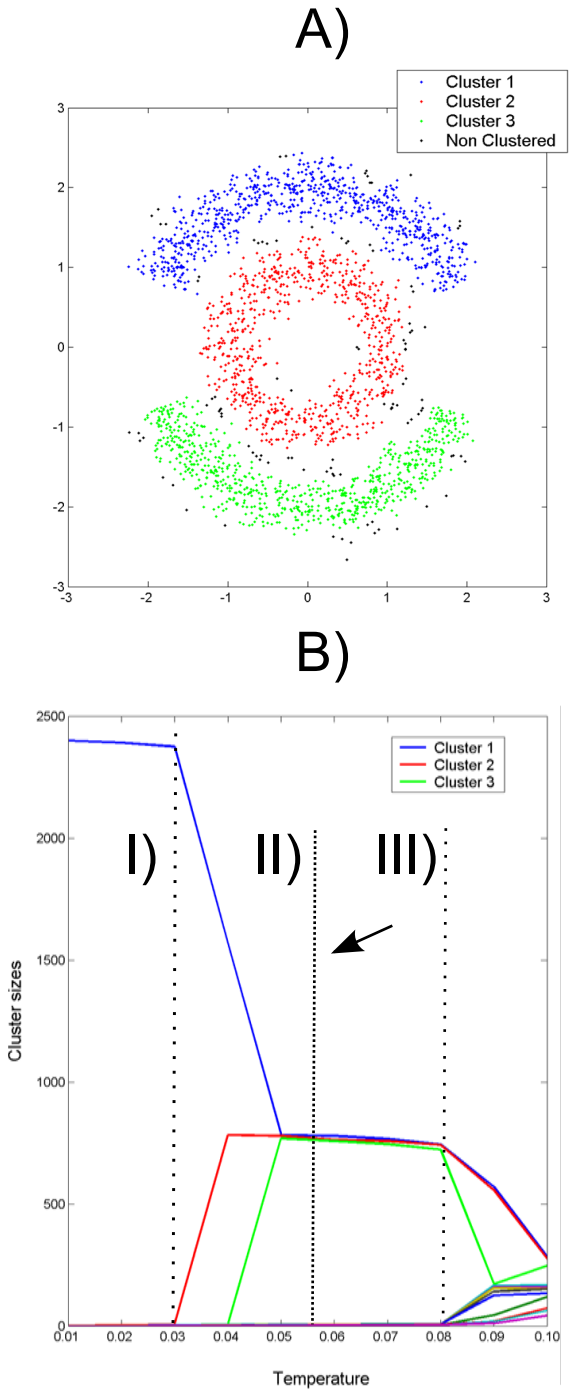

Figure 1.12: Toy example of superparamagnetic clustering; a) data successfully divided into 3 clusters and a number of elements remained unclassified (outliers - black dots); b) χ function helped identify superparamagnetic region (II) (pointed by arrow); particles marked in colors (a) were grouped as indicated by (II); y-axis shows the number of cluster elements. Adapted from [149] © 2004, Massachusetts Institute of Technology.

downside is that it is not an online tool, somewhat limiting its applications in a number of research scenarios. However, it represents an attractive and efficient solution for applications going far beyond topics presented here into other research domains.

Chapter 2

Reliability of statistical features describing neural spike trains in the presence of classification errors

Modern applications that involve signal recording from many electrodes call for automated methods for spike detection and classification. However, interpretation of these data represents a big challenge. Typically, one aims at summarizing the findings with a few parameters. It is important to see how robust these parameters are with respect to classification errors. We address the inevitable classification errors and propose a way to avoid them. The special focus is on low quality recordings (low spike SNR), which are frequently present in practice. First, the spike-rate function is introduced and described using inter-spike intervals (ISI) as the main information about the spike firing pattern. Then we introduce the parameters that characterize ISI distribution. These are the key tools for interpretation of neural firing and its changes. Finally, we analyze the cases with present errors in classification and offer a scheme to detect and circumvent these errors. This chapter is based on work published in [97].

2.1 Firing rate function of a spike train

Spikes convey information through their timing [32]. Although spikes can vary somewhat in duration, amplitude, and shape, they are typically treated in neural

studies as identical stereotyped events. If we ignore the brief duration of a spike (about 1-3 ms), a spike sequence can be characterized simply by a list of the times when spikes occur - timestamps. Thus, the timestamps associated with a neuron represent its firing pattern. This pattern can be analyzed with respect to regularity, mean firing frequency, etc. But first, in order to comprehend the difficulties and limitations of such analysis, let us see how the so-called spike-rate function can be theoretically seen and analyzed.

Let us denote timestamps for n spikes by t_i with $i = 1, 2, ..., n$. We denote the start and the end time of the recording by zero and T respectively ($0 \leq t_i \leq T$ for $\forall i$). The spike time sequence $\rho(t)$ can also be represented as a sum of idealized spikes in the form of Dirac δ functions:

$$\rho(t) = \sum_{i=1}^{n} \delta(t - t_i) \tag{2.1}$$

Convolving this function with a given spike shape gives rise to a measured (noiseless) signal.

Because the sequence of spikes generated by a given stimulus typically varies from trial to trial, neuronal responses are typically treated probabilistically, and characterized by the probability that a spike occurs at a particular time during a trial.

For the particular case of spike occurrences, we can write the probability that a spike occurs between times t and $t + \triangle t$ for a small $\triangle t$ as $p(t) \triangle t$ where $p(t)$ is the spike probability density function. By definition in this particular case, this probability function is actually the firing rate of the cell, $r(t)$: $p(t) = r(t)$.

The firing rate at time t, $r(t)$, can be estimated as the average of a number of trials assuming a given (constant) stimulus on which a spike occurred between the t and $t + \triangle t$. For sufficiently small t and sufficiently large numbers of trials, this fraction provides a good estimate of $r(t)$.

Unlike $r(t)$, the spike-count rate can be determined for a single trial. This rate, denoted as r and assuming n observed spikes during time T can be derived as:

$$r = \frac{n}{T} = \frac{1}{T} \int_0^T d\tau \rho(\tau) \tag{2.2}$$

For a number of trials, the average spike-rate $\langle r \rangle$ can similarly be determined as:

$$\langle r \rangle = \frac{\langle n \rangle}{T} = \frac{1}{T} \int_0^T d\tau \langle \rho(\tau) \rangle = \frac{1}{T} \int_0^T dt r(t) \tag{2.3}$$

Having the constant response or large enough observations to derive the spike-rate function is a pretty much idealized case. In reality, we rely on estimating this firing rate function from real measurements. This is a difficult task because, first of all, we do not have the option of continuously monitoring this function at all times. We start measuring at an arbitrary moment (from the viewpoint of a cell) and stop at another arbitrary moment. In other words, some stochastic process that triggers the cell to fire represents a function that we aim to estimate based on a limited observation window. In order to do so, we often employ so-called windowing, which is an approximation of the spike-rate function to make it analytically describable. This is often done by convolving this discrete function with another, window function, that smoothens it and avoids arbitrary placement of discrete bins. An example of this procedure and its outcome is portrayed in Figure 2.1.

2.2 Neuronal coding

Neuronal coding is concerned with characterizing the relationship between the (known or unknown) stimulus and the individual or ensemble neuronal responses and the relationship among electrical activity of the neurons in the ensemble [17]. Based on the theory that sensory and other information is represented in the brain by networks of neurons, it is thought that neurons can encode both digital and analog information [173]. This means they can be triggered by neurons they are connected with directly but also by an outside LFP wave that alters their membrane potential and to which they can synchronize. It is the goal of neuroresearch to try and decode this information by estimating the spike-rate function.

2.2.1 Rate and temporal coding

A sequence of spikes may contain information based on different coding schemes. In motor neurons, for example, the strength at which an innervated muscle is flexed depends solely on the firing rate (a "rate code"). Alternatively, a complex "temporal code" is based on the precise timing of single spikes. They may be locked to an external stimulus such as in the visual system or be generated intrinsically by the neural circuitry [66]. Whether neurons use rate or temporal coding or both is a topic of still ongoing debate within the neuroscience community.

Rate coding

Rate coding assumes that most information about the stimulus is contained in the firing rate of the neuron. Because the sequence of spikes varies from trial to trial, neuronal responses are typically treated probabilistically. They may be characterized by firing rates, rather than as specific spike sequences. In most sensory systems, the firing rate increases, generally non-linearly, with increasing stimulus intensity [157]. Here, any information possibly encoded in the temporal structure of the spike train is ignored [180].

The concept of firing rates has been successfully applied during the previous decades and became a standard tool for describing the properties of all types of sensory or cortical neurons, partly due to the relative ease of measuring rates experimentally. However, this approach neglects all the information possibly contained in the exact timing of the spikes. During recent years, experimental evidences have suggested that a straightforward firing rate concept based on temporal averaging may be too simplistic to describe brain activity [165].

During rate coding, precisely calculating firing rate is very important. Different averaging procedures are being employed, namely average over some time window or an average over several repetitions of the experiment. The example of averaging the spike-rate function with different windowing functions is portrayed in Figure 2.1 taken from [32]. In rate coding, learning is based on activity-dependent synaptic weight modifications. Spike-rate can be changed due to some internal or external trigger and this property is widely used to correlate a controlled (or observable) stimulus with changes in brain or vice-versa: to pinpoint changes in the associated neural network.

Temporal coding

In cases when precise spike timing or high-frequency firing-rate fluctuations carry information, the neural code is often referred to as the temporal code [32]. As shown in many studies and reviewed in [18], the temporal resolution of the neural code is on a millisecond time scale, indicating that precise spike timing is a significant element in neural coding. Temporal codes employ those features of the spiking activity that cannot be described by the firing rate. As there is no absolute time reference in the nervous system, the information is carried either in terms of the relative timing of spikes in a population of neurons or with respect to an ongoing brain oscillation [18].

The temporal structure of a spike train or firing rate evoked by a stimulus is determined both by the dynamics of the stimulus and by the nature of the neural encoding process. Stimuli that change rapidly tend to generate precisely timed spikes and rapidly changing firing rates no matter what neural coding strategy is being used. The temporal precision of the spiking response does not arise solely from the dynamics of the stimulus, but can relate to properties of the stimulus.

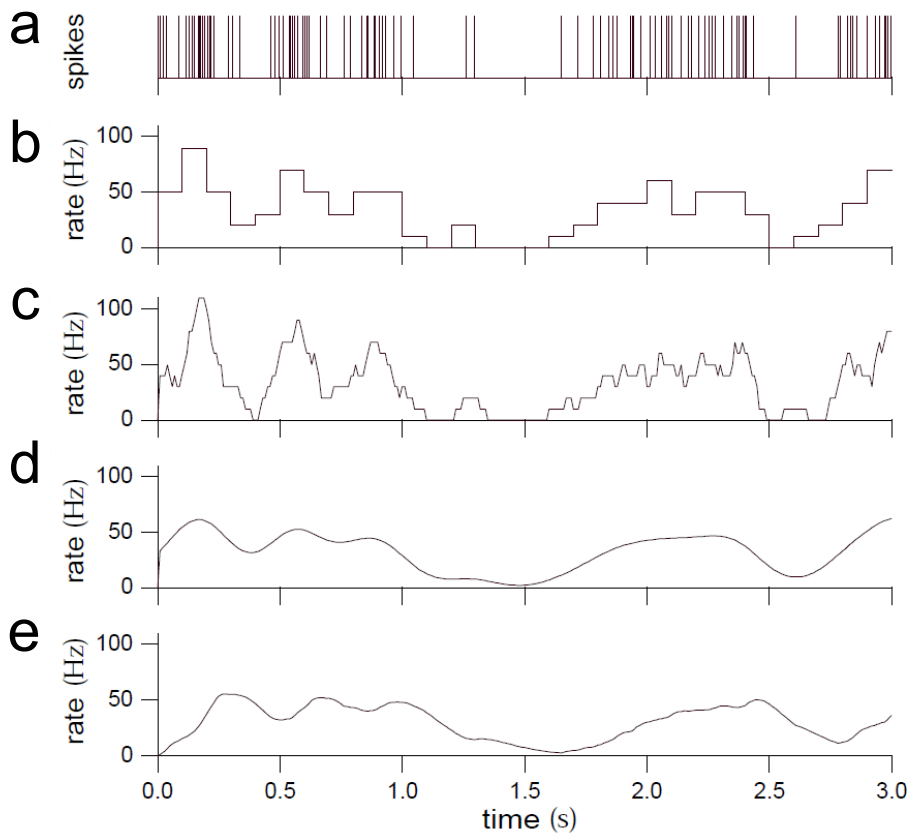

Figure 2.1: Firing rates approximated by different procedures. a) A spike train from a neuron in the inferior temporal cortex of a monkey recorded while that animal watched a video on a monitor under free viewing conditions. b) Discrete time firing rate obtained by binning time and counting spikes with t = 100 ms. c) Approximate firing rate determined by sliding a rectangular window function along the spike train with t = 100 ms. d) Approximate firing rate computed using a Gaussian window function with $\sigma_t = 100$ ms. e) Approximate firing rate for an α function window with $\frac{1}{\alpha} = 100$ ms. (Data from Baddeley et al., 1997. [4]) and printed in [32], ©2001, MIT press Cambridge, MA.

The interplay between stimulus and encoding dynamics makes the identification of a temporal code difficult [180].

Another way to look at the rate versus temporal coding is observing the speed of change of the spike-rate function $r(t)$ (assuming it is *a priori* available to observer): if it varies slowly with time, the code is typically called a rate code, and if it varies rapidly, the code is called temporal.

Temporal coding offers one way to explain e.g. the learning process. The modifications in synaptic strength between neurons can depend not only on spike rates (rate coding) but also on spike timing patterns (temporal coding), i.e., it can be a special case of spike-timing-dependent plasticity.

2.2.2 What can we infer from the spike-rate function?

The number of possible spike sequences caused by many connections with other neurons that act as possible inputs is typically so large that even roughly estimating all of their probabilities of occurrence is impossible. Further, from a practical viewpoint, the question is what kind of information do we need to infer from recorded neurons? No matter the density of recording sites or the quality of modern neuroprobes, we are still unable to comprehend the complexity of neural processes in the brain and can observe only a very tiny fraction of neurons. Therefore, we often limit our goals and simplify our conclusions to being able to: 1) detect global changes in neural spiking behavior 2) correlate spiking behavior of neurons either between one another or to an external stimulus or internal brain condition (which we often impose).

For both of these goals, we need a way to efficiently detect states and changes of the spike-rate function. For the first, this function can be described by statistical means where the derived parameters reveal its main features. For the second goal, statistics will once again be employed but this time to correlate more spike-rate functions or create a correlation between spike-rate function and stimulus/condition.

2.2.3 Homogeneous and Inhomogeneous Poisson process

Out of the sea of possible spike-rate functions, we address two important cases: the homogeneous and the inhomogeneous Poisson process. It is often the case that an observed spike-rate function is a pure Poisson process or the combination of Poisson and another underlying function(s).

A stochastic process that generates a sequence of events, such as spikes, is called a point process. In general, the probability of an event occurring at any given time could depend on the entire history of preceding events. If this dependence extends

only to the immediately preceding event, so that the intervals between successive events are independent, the point process is called a renewal process. If there is no dependence at all of the renewal process on preceding events, so that the events themselves are statistically independent, we have a Poisson process. The Poisson process provides an extremely useful approximation of stochastic neuronal firing. To make the Poisson process presentation easier to follow we describe two cases, the homogeneous Poisson process, for which the average firing rate is constant over time, and the inhomogeneous Poisson process, which involves a time-dependent firing rate. If the spike-rate function falls under Poisson process, the firing rate is all that is needed to compute the probabilities for all possible action potential sequences.

Homogeneous Poisson process

For a homogeneous Poisson process, the spike-rate function is independent of time, $r(t) = r$. The Poisson process generates every sequence of n spikes with equal probability. The probability $P[t_1, t_2, ..., t_n]$ can be expressed in terms of another probability function, $P_T(n)$ which is the probability that any sequence of n spikes occurs within a trial of duration T. If we assume that $0 \leq t_1 \leq t_2 \leq ... \leq t_n \leq T$, the relationship is:

$$P(t_1, t_2, ..., t_n) = n! P_T(n) \left(\frac{\triangle t}{T} \right) \tag{2.4}$$

To obtain a formula for continuous Poisson distribution $P_T(n)$, we start from the assumption that there are M bins (the time T is divided in M equal parts) and letting the bin size be $\triangle t = \frac{T}{M}$, we can impose an infinitesimal case where $\triangle t \to 0$. Then, following a derivation from [32], we obtain this formula:

$$P_T(n) = \frac{(rT)^n}{n!} e^{-rT} \tag{2.5}$$

Inhomogeneous Poisson process

If the firing rate depends on time, different sequences of spikes occur with different probabilities, and $P[t_1, t_2, ..., t_n]$ depends on the spike times. Because spikes are still generated independently by an inhomogeneous Poisson process, their times only enter into probability P through the time-dependent firing rate $r(t)$. Assuming that the spike times are ordered as before ($0 \leq t_1 \leq t_2 \leq ... \leq t_n \leq T$), the probability density for n spike times ([32]) is:

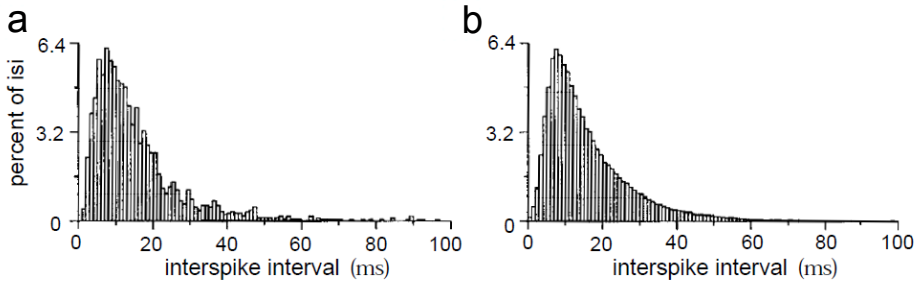

Figure 2.2: (a) Interspike interval distribution from an extrastriate area of the MT neuron responding to a moving random dot image. The probability of interspike intervals falling into the different bins, expressed as a percentage, is plotted against interspike interval. b) Interspike interval histogram generated from a Poisson model with a stochastic refractory period. Adapted from Bair et al. [5], printed in [32] ©2001, MIT press Cambridge, MA.

$$P[t_1, t_2, ..., t_n] = e^{-\int_0^T dt r(t)} \prod_{i=1}^{n} r(t_i) \tag{2.6}$$

2.3 Inter-spike interval (ISI) and autocorrelation histograms

ISI histogram

For most purposes, the spike-rate function is not observed directly but rather through its derivative that provides the time differences between successive spikes. This derivative is referred to as the interspike interval function (ISI). For this purpose, the researches often use the so-called ISI histogram (ISIH). The example of a measured stochastic neuron firing and the theoretical ISIH for a Poisson process is portrayed in Figure 2.2 taken from [32].

Another important phenomenon, called bursting of a neuron, can be detected from the observation of ISIH. Bursting is a dynamic state where a neuron repeatedly fires discrete groups (or bursts) of spikes. Each such burst is followed by a period of "regular" activity before the next burst occurs. Neuronal bursting plays an important role in communication between neurons. In particular, bursting neurons are important for motor pattern generation and synchronization. A

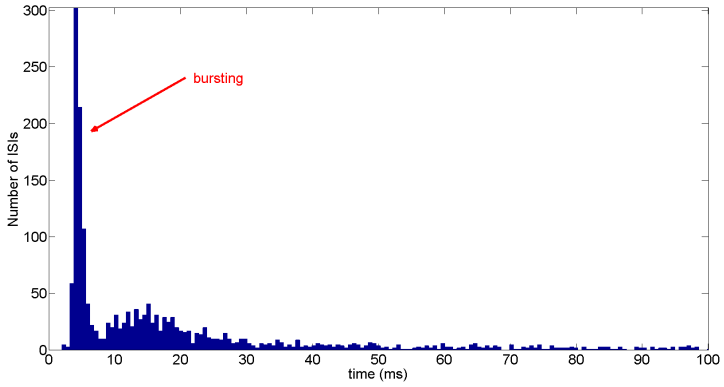

Figure 2.3: An example of bursting neuron ISIH

neuron is considered to be bursting if it is firing consecutive spikes with very small intermediate break intervals ($<$ 5 ms). On the ISIH, burst are observed as peaks occurring near the beginning of the x-axis (Figure 2.3).

Although ISIH is a very useful tool, one practical problem remains: what is the optimal bin size? ISIH can visually reveal or "hide" the underlying spiking function depending on the correct setting of the bin size. Figure 2.4 reveals one example how the same process can be portrayed just using different bin sizes and effectively hide this process.

However, determining the optimal bin number (size) is non-trivial and although there were a few attempts at addressing this problem (e.g. [128], [27]) there is no universally accepted solution for this problem. More formal ways of analyzing ISIs are still needed.

Autocorrelation function and histogram

The use of ISIH does not provide insight into second-order changes in the dynamics of neural firing. The autocorrelation function can shed light on this. It represents a joint probability density function of spike occurrences at times t and $t+\tau$ where τ is an arbitrary time delay. If we assume the mean firing frequency of the firing neuron is μ, the autocorrelation function $R_{rr}(\tau)$ can be calculated as in [62]:

$$R_{rr}(\tau) = \langle r(t)r(t+\tau)\rangle - \mu^2 = \langle (r(t)-\mu)(r(t+\tau)-\mu)\rangle \tag{2.7}$$

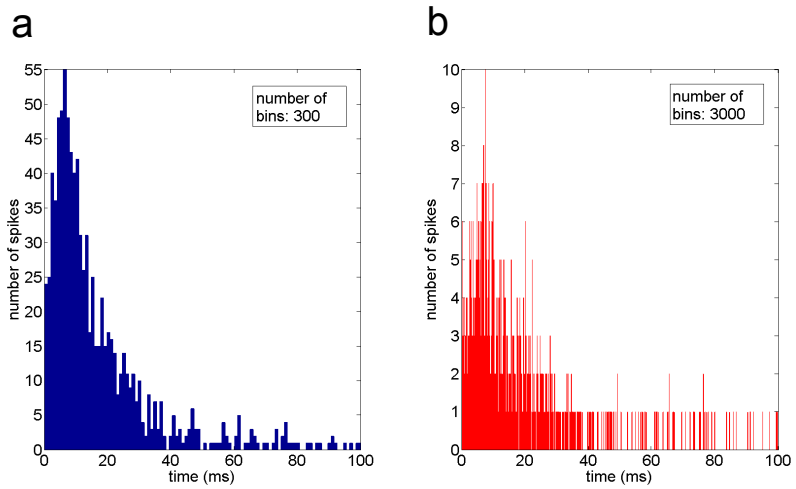

Figure 2.4: Underlying Poisson distribution might evade visual detection following the derivation of ISIH. Same set of ISI values plotted with a different number of bins: (a) number of bins=300 b) number of bins=3000.

Here, units are $(spk/sec)^2$. Stationarity assumption implies the independency of $R_{rr}(\tau)$ from the absolute time point t. It also follows that $R_{rr}(\tau) = R_{rr}(-\tau)$. Subtracting the μ^2 enforces normalization $R_{rr}(\tau) \to 0$ for large values of τ, which is expected since 2 spikes separated by a large time distance are expected to be uncorrelated:

$$\langle r(t)r(t+\tau)\rangle = \langle r(t)\rangle\langle r(t+\tau)\rangle = \mu^2 \tag{2.8}$$

For a Poisson process, we have $R_{rr}(\tau) = \mu\delta(\tau)$, where δ-function stands for the sure event of a spike appearing at time distance τ from the previous spike. Naturally, this probability drops to zero for a Poisson process, since events are completely uncorrelated. Therefore, for such a process, the autocorrelation function would not have much meaning. In reality, things are different and neuron firing does not strictly follow such a distribution. For instance, in [135], the differentiation of neurons by spiking properties revealed by autocorrelation function portrayed through a histogram (autocorrelation histogram) yielded the division in 3 different groups of neurons as portrayed in Figure 2.5. This property often makes an autocorrelation histogram a valuable tool for visual discrimination of neurons with different firing patterns.

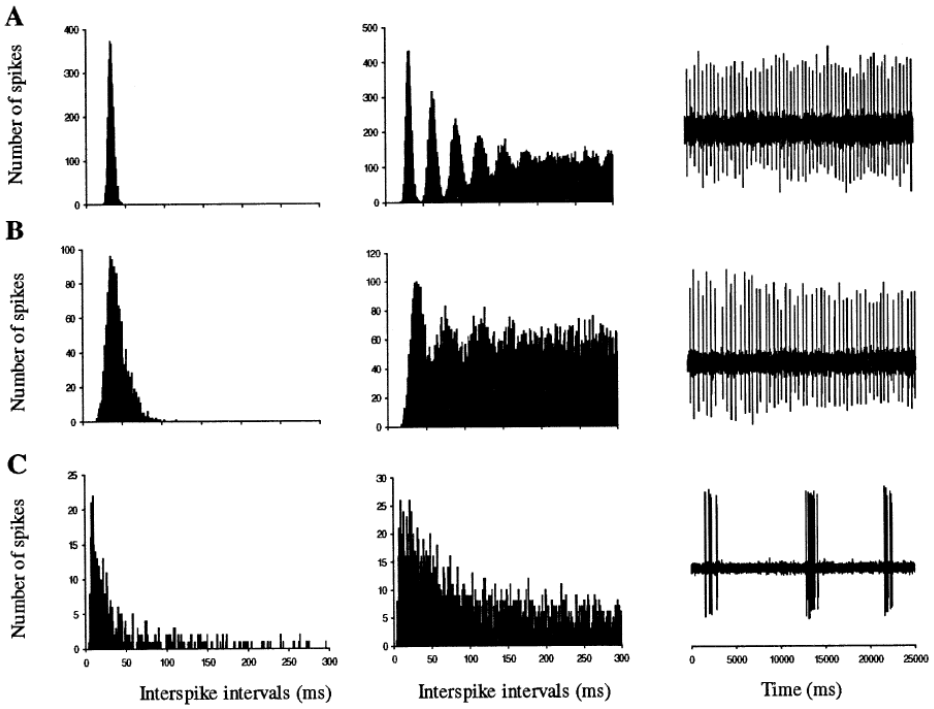

Figure 2.5: Interspike interval histograms (left), autocorrelograms (middle) and samples of spontaneous activity (right) illustrating the different types of firing pattern of GP neurons. (A) A representative example of a GP neuron discharging in a tonic regular pattern, (B) GP neuron with irregular activity and (C) GP neuron exhibiting burst activity with pauses. Taken from [135].

2.4 Reliability of statistical features describing neural spike trains in the presence of classification errors

In order to investigate functioning of the brain processes, it is important to have reliable processing of neural activity (Chan et al. 2010., [25]). For precise tracking of local neural network processes, reliable clustering of single neurons' action potentials (spikes) is necessary. So far, it was common to keep the signals of high quality and discard the others. This work examines the possibility of extracting reliable information from bad quality signals, in the presence of spike classification errors. We tested the robustness and information capacity of several statistical parameters used to describe firing patterns (ISIs) of spike trains using simulated signals mimicking most common cases in nature. Although complete reconstruction

of firing patterns is not always possible, we show that the approximation of the mean firing frequency as well as the detection of bursting processes can still be quantified successfully, thereby paving the way for future applications.

We investigate the robustness of certain statistical parameters used to describe firing patterns of neurons (spike-rate function) when the quality of the signal and the spike classification is low. In order to detect and assign spikes to their firing neurons, we first apply the described Wave_clus spike clustering algorithm ([149]). We then continue and generalize our approach so that arbitrary clustering algorithm can be used. We assume and vary a certain percentage of wrongly classified spike appearance times (timestamps) and observe the results in terms of errors of statistical parameters used to describe spike trains.

Using artificial signals with realistic distributions, with known underlying values of parameters, we show how to assess the information carrying capacity of each of them as well as their robustness. Moreover, these known underlying distributions allow us to compare the error between the results obtained from a sample of timestamps retrieved following these distributions and the theoretical function. Standard parameters (e.g. mean, median, burst coefficient, coefficient of variation, skewness, kurtosis etc.) are used. In addition new parameters and their rationale's are also introduced.

On the robustness of parameters in the presence of classification errors

Reported values of statistical features for neuronal clusters, like mean firing frequency or coefficient of variation are often taken for granted. However, one should be aware of deviations caused by clustering errors. Figure 2.6 shows one example of a cluster associated with a single neuron by the classification algorithm. It is obvious that at least 2 different spike shapes were merged as a result of classification errors.

2.4.1 Methods

Statistical features for description of spike-rate function

Many studies consider the mean firing rate as the most important parameter to describe the firing pattern of a neuron. This hugely simplifies the variety of realistic cases effectively averaging ISIs. Moreover, the question of the robustness of this sole measure of neural activity is raised. Variety of different parameters is first introduced with a purpose to faithfully describe main features of spike-rate function.

Mean: The mean represents the average value of extracted interspike intervals (formula 2.9). Here, x_i represents the i-th interspike interval.

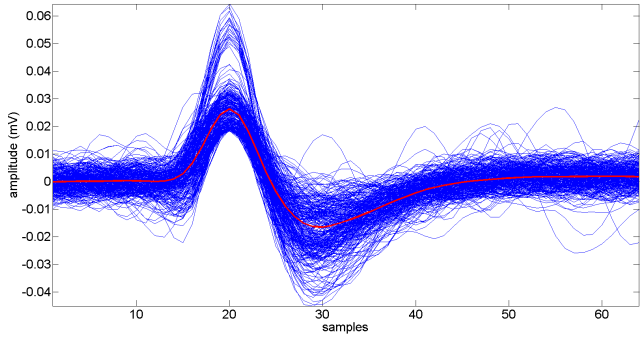

Figure 2.6: Overlayed spikes identified as belonging to a single cluster (blue) together with the mean shape (red). Visually identified "sub-grouping" strongly suggest errors in classification.

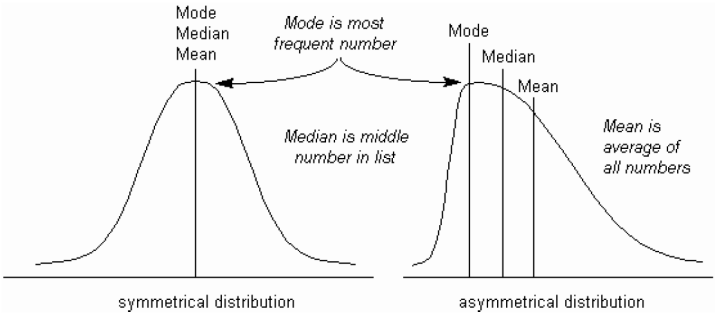

Figure 2.7: Mean, median and mode in a symmetrical and asymmetrical distribution [166].

$$\mu = \frac{1}{n}\sum_{i=1}^{n} x_i \tag{2.9}$$

Median: When a finite list of interspike intervals is ordered from the lowest to the highest value, the median represents the middle number. If there is an even number of interspike interval values, then the median is obtained by taking the mean value of the two middle numbers of this ordered list. For a skewed distribution, the mean is different from the median or the mode (most frequent value), see Figure 2.7.

Standard deviation: To describe the variability of the interspike interval values, the standard deviation is calculated using formula 2.10. Note the $n-1$ in the denominator used when calculating the standard deviation from a sample distribution. Naturally, a low value suggests a small variability of ISIs and thus, a stable firing pattern. In return, this results with a peaked probability distribution function. Likewise, a higher value for the standard deviation indicates a larger range of ISI values.

$$\sigma = \sqrt{\frac{1}{n-1}\sum_{i=1}^{n}(x_i-\mu)^2} \tag{2.10}$$

Skewness: The skewness is a measurement for the asymmetry of the probability distribution function of ISIs. A negative skewness indicates that the tail on the left side of the underlying probability function is longer than the tail on the right side. A positive skewness indicates the opposite. However, a small value for the skewness does not necessary imply symmetric distribution, it rather points that the values are relatively evenly distributed on both sides of the mean [167]. The skewness is calculated using formula 2.11

$$skewness = \frac{1}{n-1}\frac{\sum_{i=1}^{n}(x_i-\mu)^3}{\mu^3} \tag{2.11}$$

Kurtosis: This parameter serves as the indicator of the "peakyness" of the probability density function. This term comes a bit vaguely and the classical interpretation of kurtosis has been questioned recently [6]. Nevertheless, assuming that kurtosis still indicates peakyness in most of the cases, it is here calculated using formula 2.12

$$kurtosis = \frac{1}{n-1}\frac{\sum_{i=1}^{n}(x_i-\mu)^4}{\mu^4} \tag{2.12}$$

$\mathbf{C_V}$: The coefficient of variation represents the ratio between the standard deviation and the mean (formula 2.13). C_V is dimensionless and thus its value does not depend on the choice of units of ISIs (e.g. milliseconds or samples). This represents the main advantage when comparing different measures for spiking variability such as the standard deviation (or variance) and C_V [98]. Logically, assuming the same ISI spread for different mean values leads to a different interpretation. Experimentally, using simulated signals, it was suggested that the values of $C_V > 1$

represent bursting activity of the neuron. The lower limit is $C_V = 0$, suggesting highly regular spiking [98].

$$C_V = \frac{\sigma}{\mu} \tag{2.13}$$

Spiking Randomness η: This parameter uses the notion of entropy and can be described as a measure of the combination of two properties:

- **"choice"** of different ISI lengths in the spike train
- **"freedom"** in the serial order of these ISI lengths

If a discrete random X has a set of possible states $x_1, x_2, ..., x_n$ and the probability of the $i-th$ state is $p_i = P(X = x_i)$, the entropy is defined following the derivation from [161] as 2.14:

$$H(X) = -\sum_{i=1}^{n} p_i ln(p_i) \tag{2.14}$$

This traditional derivation of entropy applies for discrete cases only therefore prompting us to define the differential entropy $h(T)$ instead, using the probability density function of ISIs ($f(t)$):

$$h(T) = -\int_0^{\infty} f(t) ln f(t) dt \tag{2.15}$$

From here, finally, spiking randomness can be defined as:

$$\eta = h(T) - lnE(T) \tag{2.16}$$

Here, $E(T)$ is the mean ISI. Estimation of $h(T)$ for a discrete sample is a whole separate issue. In short, for a renewal process it can be calculated using Vasicek's estimator ([174]) as:

$$\hat{h} = \frac{1}{n}\sum_{i=1}^{n} ln\left[\frac{n}{2m}\left(t_{i+m} - t_{i-m}\right)\right] + \varphi_{bias} \tag{2.17}$$

This notation assumes that ISIs are ordered ($t_1 < t_2 < ... < t_n$). The positive integer parameter $m < \frac{n}{2}$ is set *a priori* using an estimate related to the number of ISIs (n) obtained in [53]. The following conditions hold: $t_{i-m} = t_1$ for $(i-m) < 1$ and $x_{i+m} = x_n$ for $(i+m) > n$. The bias-correcting factor is:

$$\varphi_{bias} = ln\frac{2m}{n} - \left(1 - \frac{2m}{n}\right)\Psi(2m) + \Psi(n+1) - \frac{2}{n}\sum_{i=1}^{m}\Psi(i+m-1) \quad (2.18)$$

Where $\Psi(z)$ is a digamma function ([2]).

For a non-renewal process, things become more complex. First, the dimension of the problem must be known beforehand. If the spiking is described by a d-dimensional probability density function, each vector $(t_j, t_{j+1}, ..., t_{j-1+d})$ of consequent ISIs represents a point in a d-dimensional space. If the observed spike train consists of N ISIs, then the total of $n = N - d + 1$ points may be obtained (assuming quasi-stationary behavior of firing). The estimator for h is then calculated as:

$$\hat{h} = \frac{d}{n}\sum_{i=1}^{n} ln\lambda_i + ln\left[\frac{(n-1)\sqrt{\pi^d}}{\Gamma(\frac{d}{2}+1)}\right] + \gamma \quad (2.19)$$

Here, λ_i is the Euclidean distance of the i-th point to its nearest neighbour, $\gamma = -\int_0^{\inf} e^{-z} lnz dz \approx 0.5772$ is the Euler–Mascheroni constant and $\Gamma(z)$ is the gamma function [2].

Although not completely defined in terms of values that can be expected and related to a certain condition, the spiking randomness represents a measure of "wealth" of information. For instance, any non-renewal spiking activity with exponential marginal probability distribution of ISIs must have $\eta < 1$, as less freedom in serial ordering of ISIs results in smaller randomness. Greater randomness is obtained as the choice of different lengths is more extensive, and there is more freedom in the ordering of these lengths [96]. The same spiking randomness may be achieved with different spiking variabilities. So this parameter is an alternative rather than a superior characteristic of neuronal firing [98].

A neuron often exhibits fast firing, triggered by external or internal stimuli. In some cases, this fast firing can be formally considered as bursting. Still, on some occasions, fast, consecutive spikes appear with ISIs longer than this predefined burst threshold. These events suggest the unusual transfer of information and their detection is desirable. For this purpose, a set of somewhat redundant parameters is introduced:

- **Pause_index**: This parameter is defined as the ratio of the number of interspike intervals longer than 50 ms over the number of intervals shorter than 50 ms. In this way it represents a measure of the "pauses" present in the spike train, meaning that the high value suggests less fast spiking events.

$$\forall x_i \in ISIs : pause_index = \frac{number\ of\ (x_i > 50ms)}{number\ of\ (x_i < 50ms)} \tag{2.20}$$

- **Pause_ratio**: The pause_ratio is another metric, logically equivalent to the pause_index, but counting the absolute periods instead. Following the same logic, identified intervals are summed. This means that the ratio between the sum of the lengths of the ISIs longer than 50 ms over the sum of the lengths of the ISIs shorter than 50 ms is computed (formula 2.21).

$$Pause_ratio = \frac{\sum_i x_i}{\sum_j x_j} \tag{2.21}$$

  i and j are the indices of ISIs such that: $i \in ISIs : \forall i\ x_i < 50ms;\ j \in ISIs : \forall j\ x_j > 50ms$;

- **Mod_burst**: This parameter compares the number of the interspike intervals less than 10 ms to the ones larger than 10 ms:

$$\forall x_i \in ISIs : mod_burst = \frac{number\ of\ (x_i < 10ms)}{number\ of\ (x_i > 10ms)} \tag{2.22}$$

- **Percentage window > 5 spikes**: This parameter plays a non-overlapping windowing function. The whole signal is divided into 100ms length windows. Thereafter, the number of these windows containing 5 or more spikes is compared to the overall number of windows and presented as the percentage. This parameter suggests fast spiking activity.

- **Percentage window > mean frequency**: Similarly as for the previous parameter, the signal is first divided into 1 second non-overlapping windows. Taking into account the extracted overall mean firing frequency μ, the counter is increased by 1 each time a 1s window has a spike frequency higher than 80% of the mean. This parameters tracks the firing "stability" (variability). If its value is too high, it servers as an indicator of wrong classification (e.g. merging more natural clusters).

Figure 2.8 from [98] shows different theoretical firing patterns and calculated values for C_V and η. This suggest the variety of different conditions that can (theoretically) be detected using these parameters.

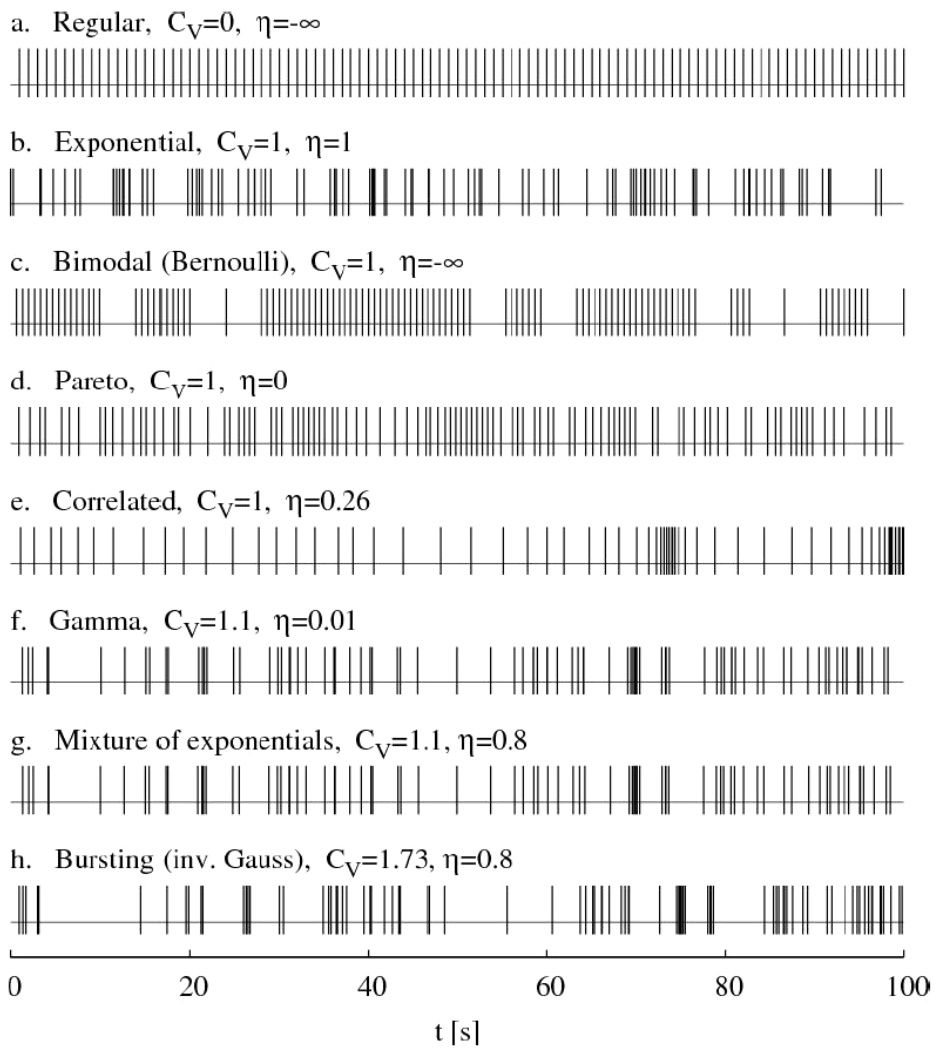

Figure 2.8: Examples of different (simulated) spike trains. The mean ISI is $E(T) = 1s$ in all cases, thus the spike trains (a–h) are equivalent in the rate coding scheme. The temporal coding scheme must be used to classify the apparent differences. The ISI variability (measured by the coefficient of variation, C_V) is not sufficient for (b–e). The ISIs described by the exponential probability distribution (b) have many different lengths (i.e. they are "variable"), but the same variability is achieved for a regular spiking disturbed by appropriately long pauses (c). Activity described by the Pareto distribution (d) has the same variability ($C_V = 1$), though it lacks short ISIs. Finally, (e) contains the same individual ISIs as (b) but ordered in a particular way (Markov chain, first-order serial correlation $\rho = 0.9$). The measure that describes the differences is randomness, η, defined as the "choice" of possible ISIs when reconstructing the spike train "spike by spike". Spike trains (f–h) were simulated using the same random seed to make the visual comparison easier. The differences in randomness between cases (f) and (g) with equal C_V are not as apparent as in (b–e). The same level of randomness, in (g) and (h), is reached with different variability and results in different spike trains. Bursting activity (h) is more variable than the exponential case (a), though its randomness is lower. Figure from [98].

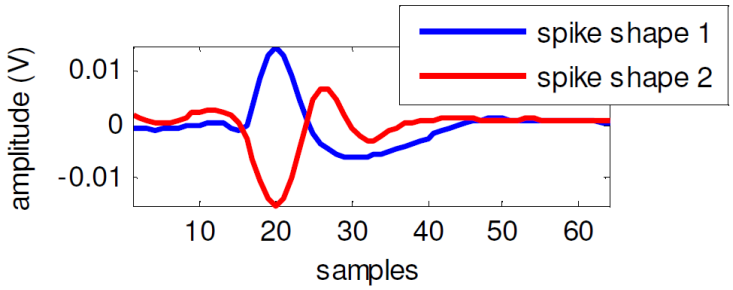

Figure 2.9: Example simulation spike shapes.

Artificially generated distributions and signals

Since real data's underlying distribution of spike timestamps is unknown, artificially generated signals were used in this study. These served as input to the clustering algorithm and for later statistical parameter estimation. In this way, the true values of parameters describing the underlying distribution can be compared to those obtained after detection and clustering. We used spike shapes obtained from real recordings, some of them available on the internet (from a study described in [155]) and some obtained from IMEC - Belgium recordings. Two example shapes (also used in this research) are shown in Figure 2.9.

Matlab was used to generate Gaussian and Poisson distributed timestamps. These are reported to be realistic models of firing patterns of many neurons (e.g. in [32]). Also, a simulated distribution of a firing pattern containing bursts (fast consecutive neural firing) was created. Signals are created by adding spikes whenever indicated by generated timestamps. Noise is also added to form a realistic artificial neuronal signal. This noise is a mixture of white and background noise. The latter consists of a large number of randomly selected and scaled waveforms which were added to mimic far away neurons ([155]). The SNR differed among those artificial signals (calculated as in formula (2.23) with n representing the number of samples of a selected spike). To create different (low quality) signals, this random noise trace can be re-scaled to obtain signals with a pre-specified SNR. Overall, around 120 signals were used in this study.

$$SNR = \frac{signalpower}{noisepower} = \frac{\sqrt{\sum_{i=1}^{n} x_i^2}}{\sqrt{n \cdot std(noise)^2}} \tag{2.23}$$

A more general and computationally faster procedure avoiding the need for the

clustering is also applied. This procedure simulates classification errors by mixing timestamps of multiple spike trains. A percentage of these timestamps, imposed by the user, is correctly classified; accordingly, misclassified (assigned to a wrong cluster) timestamps are added as well. In addition, a certain percentage of timestamps is left undetected to imitate the realistic case, where some spikes evade detection because of low SNR. The computational gain is achieved by mimicking the clustering results without applying the actual procedure. After assigning timestamps to clusters, robustness of parameters is tested.

Calculation of errors

We can compare values and errors of specified parameters at three different moments of the spike train analysis based on the following three models:

- Continuous underlying distribution
- Sampled distribution after taking values conforming to the continuous distribution for the interspike intervals (Figure 2.10 a)
- Distribution after clustering (Figure 2.10 b)

We extracted the described parameters from the computed ISIs. These parameters assist us in describing the firing model of a neuron. To compare the three different models, the errors on the used statistical features have to be calculated. For example, the error between the mean of the sampled distribution and the distribution after clustering is calculated as in formula (2.24). The error shows how this value deviates after clustering compared to the one before. This deviation error could therefore be larger than 100% in contrast to the classification errors, which could potentially reach up to 100% (when all the spikes are assigned to the wrong cluster).

The error between the sample distribution and the theoretical underlying distribution served as a check whether a distribution sample is large enough to pinpoint to the real spike-rate function. Since the simulated signals were 20s long and this error rate was below 1% and found satisfactory, obtained results were omitted and formally reported elsewhere [96].

$$error(\%) = \left| \frac{mean_{clustered} - mean_{sampled}}{mean_{sampled}} \right| \cdot 100 \tag{2.24}$$

The behavior of the parameters is examined for different distributions and different SNRs in the sense of their robustness (to errors) and information that they carry. Also, after clustering, some of the spikes are not detected by the algorithm, which can be observed as peaks on multiples of mean firing frequency (Figure 2.10 b).

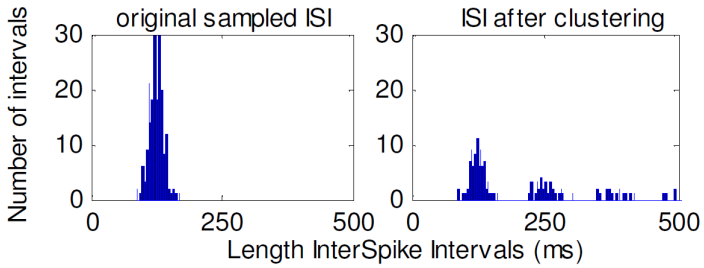

Figure 2.10: (a) Sampled normal distribution provides ISIs for generation of the artificial neuronal signal. (b) ISIH after clustering (using a spike sorting algorithm).

Overclustering

Sometimes the clustering outcome provides clusters with similar shapes and it remains unknown if it is a result of "overclustering" of a single neuron activity. To investigate this case and its reflection on values of parameters, the following approach was adopted. Two distributions of interspike intervals can be compared after splitting the underlying distribution. More specific, a certain percentage of the total of ISIs generating the underlying distribution is assigned to one cluster. The second cluster consists of the remaining ISIs of the same underlying distribution. It was investigated whether these separate clusters have similar enough values for certain parameters. If so, this could indicate the need to merge them.

2.4.2 Results

Parameter estimation

The goal we set was to investigate statistical parameters and their information capacity for low quality clusters. More than 120 signals were examined with different timestamp distributions, different low SNRs and different spike shapes. The median was found to be a better feature to approximate the mean frequency of the underlying distribution than the extracted mean of the reconstructed distribution after clustering. Indeed, the calculated errors between the values of the median describing the two sampled models - before and after clustering - are in all of our simulations smaller compared to the errors of the mean. These errors reduce when the SNR increases, so the estimation of the mean firing frequency becomes better. An example is shown in Figure 2.11 for signals with different low SNRs.

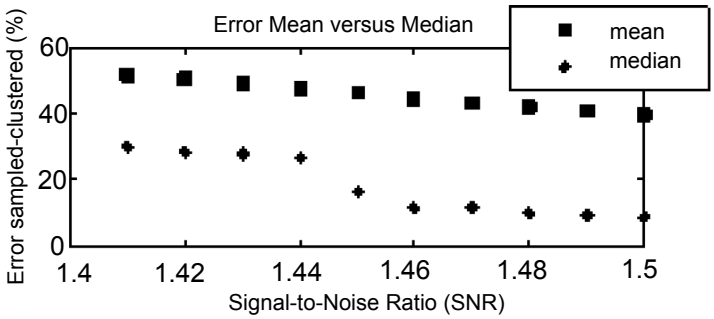

Figure 2.11: Average error of mean versus error median parameters for signals with different (low) SNRs.

Table 2.1: Example of two normal distributions (with and without bursts) corresponding to the two active neurons recorded in one signal. C_V is calculated for two models - before and after clustering. The second column is a repeated simulation with other values for the means of the underlying distributions.

Mean (ms)	83,33 +bursts	125,00	75,00 +bursts	133,33
Std (ms)	12,50	20,00	12,50	20,00
C_V,before_cl	0,60	0,17	0,45	0,15
C_V,after_cl	1,63	0,52	1,86	0,53

C_V parameter was found to be informative and reasonably accurate (examples shown in Table 2.1). $C_V > 1$ was reported as an indicator for bursting activity ([98]). In our simulations this feature has higher values for signals with bursts, reaching values ≥ 1 after clustering, substantiating this claim. As a consequence of low SNR many spikes are not detected, hence the change of the standard deviation and mean will lead to the large deviations of the C_V. Nevertheless, it has informative capacity indicating main features of distribution (Table 2.1).

Spiking randomness indicates the variety of spiking patterns. However, it showed large and unpredictable errors, indicating little practical usefulness, when a spike firing pattern is incomplete. This proved to be very much related to multiple peaks in ISI distribution. The mean error was $401,67(\pm 403,22)\%$. Burst parameters can reveal the presence or absence of bursts (Table 2.2). In this case both features mod_burst and "percentage window > 5 spikes" are larger than zero. On the other

Table 2.2: Examples of two normal timestamp distributions (with and without bursts), selected for generating an artificial signal. Bursting parameters are calculated for two models - before (b_cl) and after clustering (a_cl).

Mean (ms)	100	108,33	91,67	116,67
	+bursts		+bursts	
Std (ms)	12,50	20,00	12,50	20,00
Mod_burst, b_cl	0,31	0,00	0,22	0,00
Mod_burst, a_cl	0,29	0,02	0,22	0,02
Pause_index, b_cl	2,74	249,00	3,60	249,00
Pause_index, a_cl	2,22	13,93	2,57	10,79
Pause_ratio, b_cl	51,57	709,15	42,41	637,41
Pause_ratio, a_cl	27,04	79,18	21,88	55,57
Perc>5spikes, b_cl	3,96	0,00	3,30	0,00
Perc>5spikes, a_cl	3,30	0,00	2,82	0,00

hand, the values for pause_ratio and pause_index are smaller than those values for signals without bursts. If all these conditions are true, even modest bursting activity of a neuron is always detected in our simulations.

Overclustering

The mean and median proved to be significantly different for the two clusters. Many missing timestamps resulted in longer interspike intervals (Figure 2.12), hence higher values for mean and median compared to those of the underlying distribution.

Although not accurate in cases of individual clusters, skewness and kurtosis proved to be good indicators of overclustering. Values for the two clusters are similar (example in Table 2.3), with respective differences of 15,61% and 18,98%. As a comparison, these differences are at least twice as large in cases of different underlying distributions.

2.4.3 Discussion

This research examined the possibility of reliable information extraction from neural clusters of bad quality, often appearing in real-life recordings. It showed that features like the mean firing frequency and burst detection can still be successfully extracted. In the future, existing as well as newly derived parameters could be tested,

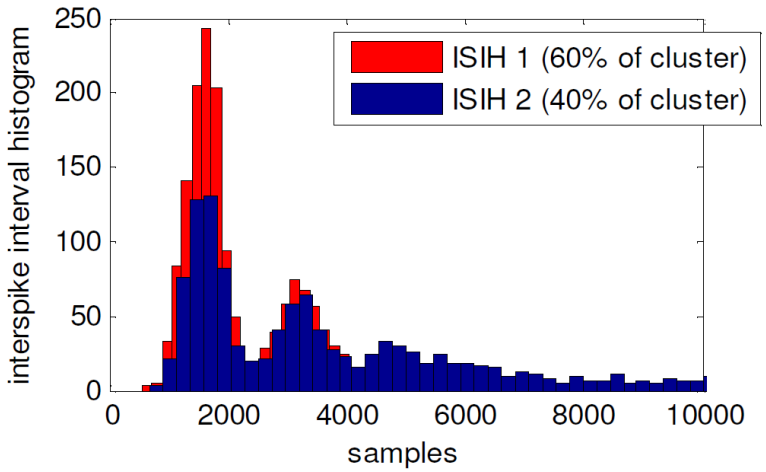

Figure 2.12: Two overlaid ISIHs, originally assumed as belonging to different clusters but having the same underlying distribution; dominant peaks matching almost perfectly.

Table 2.3: To simulate overclustering, one original normal distribution (orig_distr) is randomly split up into two clusters. A certain percentage of timestamps is assigned to the first cluster and the other timestamps to the second cluster. Values for skewness and kurtosis are calculated and compared. Two examples are given.

Mean (Std) (ms)	66,67 (12.5)		66.67 (12.5)	
cluster 1/ cluster 2	70	30	80	20
skewness, orig_distr	0.09		0.09	
skewness, after_cl	2,17	1,81	2,24	2,02
kurtosis, orig_distr	3,19		3,19	
kurtosis, after_cl	9,12	7,43	9,38	9,97

possibly circumventing the problems of missed spikes and thus adding robustness and increasing the usefulness of the extracted spike trains. These strategies could be implemented in the future as a tool that would help include previously discarded information coming from more distant neurons or signals corrupted in other ways, thus greatly increasing the possibilities for observation of brain conditioning. Initial results showed that even the signals of lower quality can grant the trustworthy analysis. This increases the available information content and therefore contributes to a more reliable experiment analysis. The use of parameters described here contributed to the obsessive-compulsive disorder (OCD) study as observed in Chapter 3. The reliability of parameters can be further improved similarly to [142] and [141] used in EMG studies. Here, a part of ISIs is first excluded based on the estimated mean firing rate by leaving out timestamps corresponding to distant ISIs. These distant ISIs are the main reason of corruption of these describing parameters even if they come as a result of an accurate classification.

On the other hand, the use of parameters skewness and kurtosis can, regardless of their imprecision, reliably point to the cases of overclustering. Fitting the ISIHs with analytical functions after clustering could be another condition to decide if the two clusters should be merged.

2.4.4 Conclusion

Reliability of spike classification of lower quality neural signals has been examined. This is encountered frequently in real-life recordings. An extremely low reliability of gathering useful information directly from traditional mean spike rate is observed. A framework that involves having more reliable parameters is introduced to describe the neural firing sequence instead, which is able to detect major spike train attributes. Furthermore, a way to detect cases of overclustering using parameter logic is also introduced. This opens the possibility of automated processing of large number of neural signals. Details of this work can be found in a master thesis that we supervised [96] and a published manuscript [97].

2.5 Additional comments on chapter composition

This chapter provided descriptions relying on the theoretical work on neural firing described in [32] ©2001, MIT press Cambridge, MA, a master thesis defended at ESAT [96], as well as the review work on parameters describing the spike-rate function treated in [98].

Chapter 3

Obsessive-compulsive disorder (OCD) study

The term deep brain stimulation (DBS) refers to the use of high-frequency electrical current for stimulation of brain regions below the cortex. DBS is readily used today for treating various neurological disorders (e.g. essential tremor, Parkinson disease, Dystonia, etc.) [144]. There is an ongoing effort to find appropriate brain regions to serve as optimal targets for DBS. This study deals with the search of a new potential target for DBS in patients with obsessive–compulsive disorders (OCD). We evaluated the single-cell activity of neurons in the bed nucleus of the stria terminalis (BST) in urethane-anesthetized rats in an animal model for OCD, the schedule-induced polydipsia (SIP) model, and compared this to the BST activity in control rats and to a third group of rats which were introduced in the model but did not develop the SIP, and thus were considered resistant. We compared the firing patterns of BST neurons between these groups, between hemispheres and made a correlation of these firing patterns to the position in the BST. The variability of BST neurons in SIP rats was lower and the spiking randomness higher than BST neurons in control rats or resistant rats. The firing rate of BST neurons in SIP rats was significantly higher and the burst index lower than BST neurons in resistant rats but not in control rats. Also, neurons from the right hemisphere in the SIP group had a higher burst index than neurons from the left hemisphere. However, this is opposite in the resistant and control group. Third, we found a higher bursting index with increasing (more ventral) depth of recording. These findings suggest that schedule-induced polydipsia, which models compulsive behavior in humans, induces a change in firing behavior of BST neurons. This Chapter is based on work published in [178], [72], [71].

3.1 Introduction

Obsessive–compulsive disorder (OCD), a psychiatric disorder with a prevalence of 0.8% in adults and 0.25% in 5–15 year old children [182],[80], is characterized by anxiety, obsessions (persistent intrusive thoughts), and compulsions (e.g. checking, ordering, and counting), which can cause significant impairment of the patients. For a small portion of the patients, current pharmacological and behavioral therapies do not relieve symptoms sufficiently [163]. Neurosurgical techniques such as capsulotomies or deep brain stimulation (DBS) in the anterior limbs of the internal capsule and the ventral striatum may be a last resort investigational treatment [137],[138]. Although these therapies may have a good outcome, little is still known about the underlying neurological mechanisms of the disorder and these therapies. New insights could be gained by investigating the neuronal activity in these brain regions.

Casual reports have described the efficacy of DBS in the bed nucleus of the stria terminalis (BST), a gray matter brain structure just below the anterior limbs of the internal capsule [117]. Figure 3.1 indicates the position of the stria terminalis in the human brain. The efficacy of DBS in this brain structure seemed to be strongly related to the position of the electrode to the BST [63]. This nucleus has connections with the cortico-striato-thalamo-cortical circuitry [46] and neuroimaging studies demonstrated the importance of this circuitry in the pathophysiology of OCD [156].

Based on these observations, we set out to investigate the neuronal single-cell activity in the BST in the schedule-induced polydipsia (SIP) model, a validated animal model for obsessive–compulsive behavior [183],[147]. In this model, hungry rats that receive a small food pellet every 60s drink a physiologically excessive amount of water. This behavior resembles the compulsions in OCD patients because this behavior is repeated over and over again in an often useless and harmful way (face validity). The SIP creates a scenario, which fits the criteria for compulsive behavior, it induces stereotyped excessive performance and resistance to both extinction and consummation [146]. In addition, the SIP model has predictive validity since drugs that efficiently reduce OCD symptoms, like fluoxetine, fluvoxamine, and clomipramine, diminish water intake in the model, while other drugs, that have no effect on OCD symptoms, like haloperidol and diazepam, do not have an effect in the model [183]. Furthermore, previous work showed the efficacy of high-frequency electrical stimulation in the BST in this model to reduce the water intake [100].

The objectives of this study[1] were to compare the neuronal firing rate and firing

[1] This study, conducted in IMEC - Belgium was the result of collaboration with Biomed group from ESAT, KU Leuven. The contributions made within the scope of this thesis include all aspects of automated signal processing of recorded neural signals.

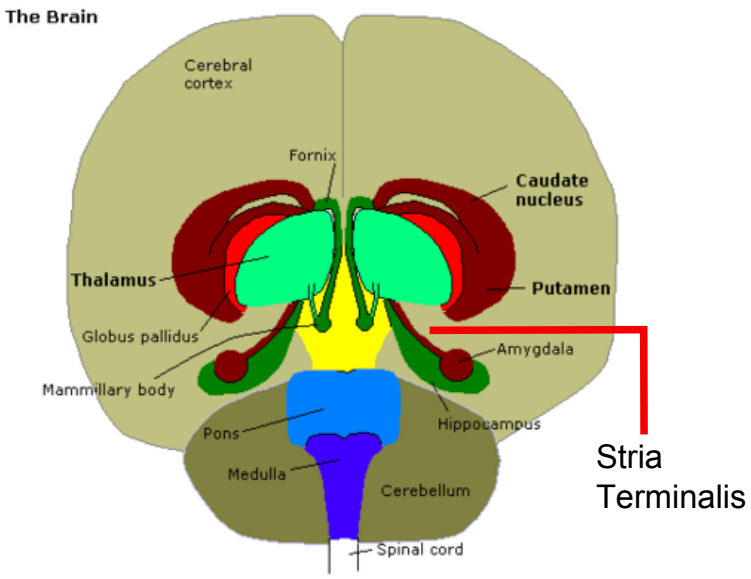

Figure 3.1: The human brain as viewed from the underside and front. The position of stria terminalis is indicated. ©2000, 2001, 2002 Free Software Foundation, Inc.

pattern (1) between SIP rats, rats that are resistant to the model, and normal control rats, (2) between the left and right hemisphere in each of the three groups (since, in some cases, unilateral deep brain stimulation is sufficient to relieve a patients' symptoms [168],[87]) and (3) to correlate the neuronal firing rate and firing pattern with the recording position within the BST in each of the three groups.

3.2 Methods

3.2.1 Subjects and housing

Forty-four young male Wistar rats were used (±200g at arrival) and housed in pairs under controlled temperature and lightening conditions with food and water available ad libitum. All experiments were carried out in accordance with protocols approved by the local university animal ethics committee and in accordance with the European Communities Council Directive of November 24, 1986 (86/609/EEC).

3.2.2 Schedule-induced polydipsia model and experimental groups

Rats were randomly allocated to one of two groups: the polydipsia group (n = 33) or the control group (n = 11). After a one-week acclimatization period, food was restricted until rats reached 85% of their original body weight. The rats were then subjected to 15 preoperative schedule-induced polydipsia tests on week days. Rats were placed in test chambers and a dispenser automatically delivered one 45-mg pellet (dustless precision pellets, F0021-J, Bioserv, Frenchtown, NJ, USA) on a fixed time 60s feeding schedule for 30 min test sessions. To assess schedule-induced polydipsia, water intake (g) was measured by weighing the water bottles before and after the 30 min test sessions. Water bottles with a ball bearing in the tube prevented water loss by spontaneous dripping. Every day the order of the subject testing was random. On the day the rat consumed 8 ml water or more [100], the rat was considered polydiptic (SIP group). Control rats (CON group) were tested in the same environment but received all the 30 food pellets at once and were pair grouped with a rat from the SIP group. If a rat, subjected to the SIP model, did not meet the 8 ml criterion after 15 test days, the rat was considered resistant (RES group).

3.2.3 Electrophysiological recording

The rats were placed under general anesthesia (urethane 1.3 g/kg, i.p.). Local anesthesia (Xylocaine® s.c., 2% 20 mg/ml; AstraZeneca SA, Brussels, Belgium) was used before scalp incision after shaving and disinfecting with alcohol (1% in 70% isopropyl alcohol). The head was positioned in the stereotactic frame so that bregma and lambda were in the same horizontal plane.

A heating blanket controlled by an anal probe prevented hypothermia during the surgery. Rats received 0.4 ml amoxicillin (Duphamox® log active; Fort Dodge Animal Health Benelux BV, Wemmel, The Netherlands) and the eyes were protected from dehydration by polymyxine B (Terra-Cortril; N.V. Pfizer S.A., Brussels, Belgium). A longitudinal incision was made and the burr holes were drilled after visualization of bregma. The electrodes (Tungsten, microTargetingTM electrode mTDWBS26710262, 1 $M\Omega$ impedance, FHC Inc., Bowdoin, USA), attached to the stereotactic arms, were placed above the burr holes. After the dura was punctured with a needle, the electrodes were implanted with a microdrive (10 $\mu m/s$, D. Kopf Instruments®, Tujunga, USA) bilaterally in the bed nucleus of the stria terminalis (coordinates: 0.60 mm posterior to bregma, 1.3 mm lateral to the midline, and 5.2–7.2mm ventral to the dura mater [143]). One insertion track per hemisphere was performed subsequently. The first hemisphere per rat was chosen randomly. When a possible neuron was encountered, signals were recorded for 5 min, amplified

and band pass-filtered (500 Hz to 5 kHz) and digitized at 24 kHz with the Leadpoint (Medtronic) where it was stored for offline analysis.

3.2.4 Histology

After the experiment, the rats were euthanized with Nembutal (3 ml, i.p.; CEVA Santé Animale, Brussels, Belgium). Next, they were perfused intracardially with 10% sucrose in distilled water (5 min) and 4% formaldehyde in distilled water (15 min) followed by the resection of the brain. The brains were processed for paraffin coronal sectioning (5 μm) and brain slices were stained with hematoxylin–eosin and examined under a light microscope. If the location of the tip of the electrode was not in the BST, according to [143], the results of that recording were excluded from the analyses. Data coming from these neurons were used to assess whether the outcome was specific for BST neurons.

3.2.5 Data analysis

The analysis was performed blindly using the Wave clus 2.0 package in Matlab (Mathworks Inc., Nattik, USA), based on superparamagnetic clustering [149], for extraction of individual neural clusters. Neurons were treated equally with no possible sub-group considerations. The output (spike clusters and timestamps) was combined with a custom made Matlab code to enable data processing [72]. Only stable neuronal activities (in the sense of observed firing during the entire recording period) with a signal-to-noise ratio (SNR) above 1.7 were used [2]. The SNR was calculated (according to the definition in [155]) as:

$$\mathbf{SNR} = \frac{\sqrt{\sum_{i=1}^{K} x_i^2}}{\sqrt{\sum_{i=1}^{K} \sigma^2}}, \tag{3.1}$$

where $K = 64$ is the number of stored samples per spike, and σ is the noise estimate calculated using Equation 1.1.

[2]Signal processing scripts were designed to load and process smaller files from the same recording sessions, granted by the recording equipment, and merge extracted clusters. Thereafter, individual clusters were analyzed using parameters described in Chapter 2, storing results in individual tables. These scripts included the signal stability test which indicated large minute-to-minute changes in mean spike firing rates. The clusters exhibiting these large changes were excluded from the analysis following an assumption of large errors resulting from spiky noise artifacts or clustering imperfections. Several other merits were used for the *a priori* exclusion of clusters, e.g. ISI histograms featuring uncommon (non-physiological) peaks.

To describe the firing properties of the neurons, we used some of the parameters described in Chapter 2: the firing rate (spikes/s), the C_V coefficient, the burst index (Mod_burst) [108],[59],[184], and the η coefficient of randomness calculated as suggested in [98]).

3.2.6 Statistical analysis

In order to correct for the dependency between multiple observations per rat, generalized estimating equations modeling with compound symmetry working correlation matrix was applied, instead of the commonly used ANOVA [112],[41]. We used a logarithmic transformation on the firing rate and variability to have a more normal distribution, but this was not possible for the burst index and the spike randomness. The generalized estimating equations modeling was carried out using the SAS system release 9.2 (SAS Institute Inc., Cary, NC, USA). p-Values < 0.05 are considered significant. Data are depicted as mean $\pm$ standard error of the mean (SEM). However, caution should be taken in the interpretation of the standard error, as this measure of variability does not take into account the dependency between different observations of the same rat, and is shown here only for illustration.

3.3 Results

Seven out of 33 animals (21%) in the schedule-induced polydipsia model reached the 8 ml criterion after 15 test sessions and were considered polydiptic. After histological analysis and spike sorting,a total of 196 neurons recorded from the BST were used in the statistical analysis, with signals from 29 neurons from the SIP group (n = 6 rats), 114 neurons from the RES group (n = 20 rats), and 53 neurons from the CON group (n = 6 rats). Only signals in accordance with criteria described in section 3.2.5 were included in the analysis.

The number of recorded neurons per rat did not differ between the groups (Kruskal–Wallis, p = 0.58). Recording sites are depicted in Figure 3.2. There was no difference in the position (subdural, mediolateral, or anterior-posterior) of the recording sites between the three groups (generalized estimating equations modeling, p = 0.25, 0.50, and 0.91, respectively). Two examples of recordings are shown in Figure 3.3 for illustration.

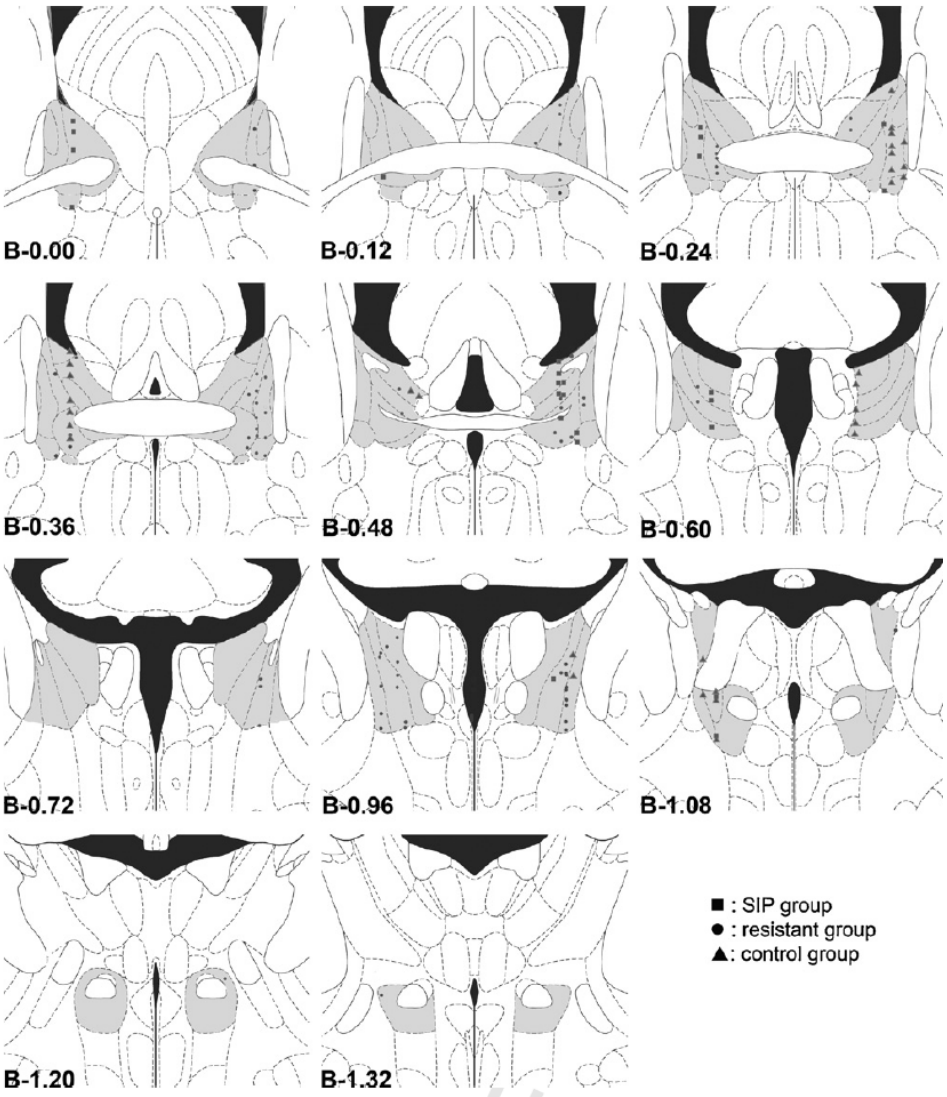

Figure 3.2: Localization of the recording positions in the schedule-induced polydipsia group (■), the control group (▲), and the resistant group (●). The bed nucleus of the stria terminalis is colored in grey. Distance of the coronal sections posterior to bregma is indicated. Adapted from [143].

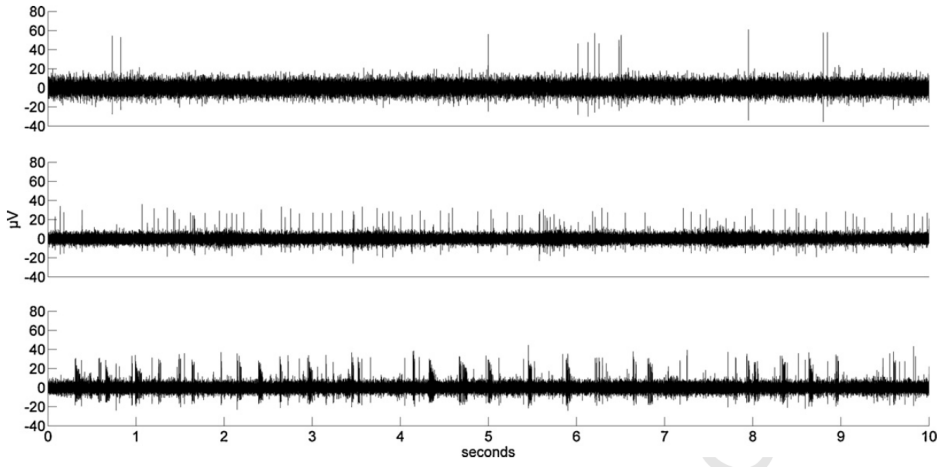

Figure 3.3: Example of a recording of 10 s of one neuron in three animals. Upper panel: a neuronal recording of a control rat with a low firing rate (1.5 Hz), high variability (5.79), a low burst index (0), and low randomness (0.47). Middle panel: a neuronal recording of a polydiptic rat with a medium firing rate (4.5 Hz), a medium variability (1.13), a medium burst index (0.1) and a medium randomness (0.23). Lower panel: a neuronal recording of a resistant rat with a high firing rate (20.2 Hz), medium variability (1.88), a high burst index (1.6), and low randomness (-1.65).

3.3.1 Firing rate and firing pattern in SIP rats, resistant rats and control rats

The firing rates and firing pattern parameters of the BST neurons of the different experimental groups are shown in Figure 3.4. The firing rate of BST neurons in SIP rats was significantly higher than that of BST neurons in resistant rats (9.89±1.99 vs. 5.32±0.58, mean ± SEM, $p = 0.03$), but not in control rats (6.95±1.02, $p = 0.44$). The variability of BST neurons in SIP rats was significantly lower than that of BST neurons in resistant and control rats (0.82±0.05 vs. 1.29±0.05 and 1.38±0.10 respectively, $p < 0.001$ and $p = 0.002$). The burst index of BST neurons in SIP rats was significantly lower than that of BST neurons in resistant rats (0.04±0.01 vs. 0.084±0.02, $p = 0.049$) but not in control rats (0.082±0.01, $p = 0.26$). The randomness of BST neurons in SIP rats was significantly higher than that of BST neurons in resistant and control rats (0.42±0.03 vs. 0.02±0.05 and 0.09±0.04, respectively, $p < 0.001$ and $p < 0.001$).

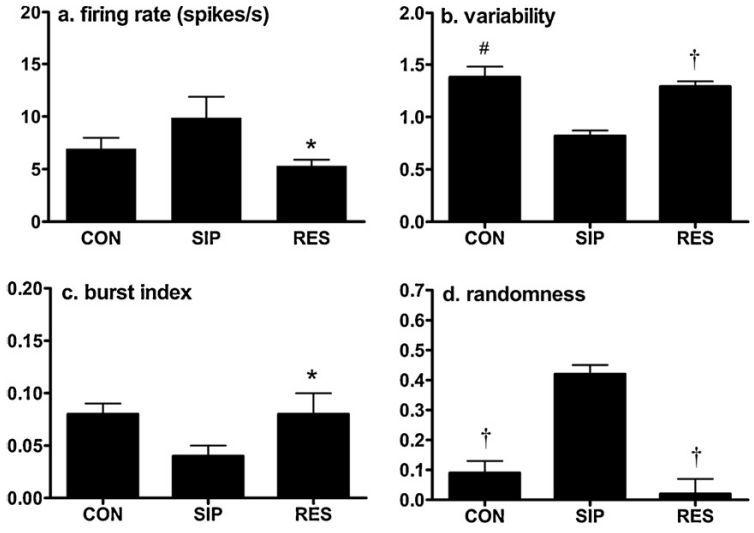

Figure 3.4: Mean (±standard error of the mean) firing rate (a), variability (b), burst index (c), and randomness (d) in all groups. CON, control; RES, resistant; and SIP, schedule induced polydipsia. *Significantly different from the SIP group at $p < 0.05$. #Significantly different from the SIP group at $p < 0.01$. †Significantly different from the SIP group at $p < 0.001$

To investigate whether the obtained results are specific only for BST neurons, we repeated the analysis using the data from neurons that were not located in the BST. A total of 365 neurons from neighboring structures were recorded, with 46 neurons from the SIP group (n = 7 rats), 201 neurons from the RES group (n = 26 rats), and 118 neurons from the CON group (n = 10 rats). There was no difference in the position (subdural) of the recording sites between the three groups (generalized estimating equations modeling, $p = 0.63$).

It was found that the higher firing rate of SIP rats vs. resistant rats was specific for the BST neurons, since for the non-BST neurons, the firing rate was lower for the SIP rats compared to the control rats and borderline significantly lower compared to resistant rats (3.36±0.73 vs. 6.28±0.61 and 4.80±0.42 respectively, $p = 0.004$ and $p = 0.054$). The higher randomness in SIP rats compared to the resistant or control rats seems not only to be present in the BST, but also in the neighboring structures (0.16±0.05 vs. 0.07±0.04 and 0.09±0.06, respectively, $p = 0.03$ and $p = 0.02$). There were no significant differences in variability or burst index between the groups in the non-BST neurons.

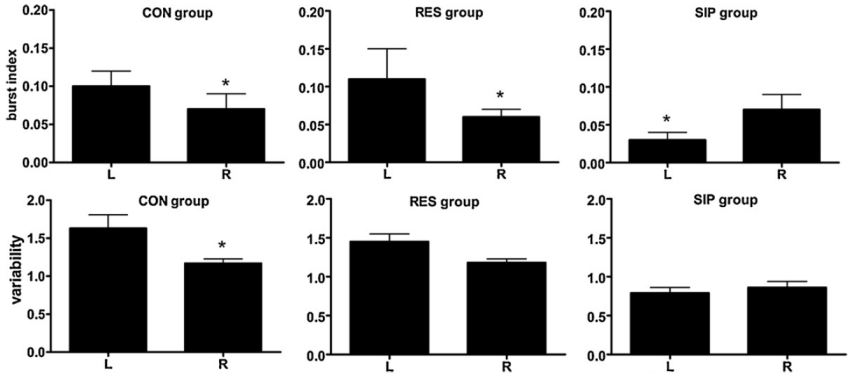

Figure 3.5: Mean (±standard error of the mean) burst index (top row) and variability (bottom row) for the left and right hemisphere per group. CON, control; RES, resistant; and SIP, schedule-induced polydipsia. *Significantly different from the other hemisphere at $p < 0.05$. #Significantly different from the other hemisphere at $p < 0.01$

3.3.2 Left-right hemisphere comparisons

In the SIP group, BST neurons from the right hemisphere showed a higher burst index than neurons from the left hemisphere (0.07±0.02 (number of neurons, n = 12) vs. 0.03±0.01 (n = 17), $p = 0.04$) (see Figure 3.5). However, in the resistant and control group, neurons from the left hemisphere showed a higher burst index than neurons from the right hemisphere (0.06±0.01 (n = 47) vs. 0.11±0.04 (n = 67), $p = 0.007$ and 0.10±0.02 (n = 25) vs. 0.07±0.02 (n = 28), $p = 0.03$). Also, in the control group, there was a significant difference in variability between neurons from the left and right hemisphere (1.63±0.18 (n = 25) vs. 1.17±0.06 (n = 28), $p = 0.02$). This difference in variability is not present in the SIP (left 0.79±0.07 vs. right 0.86±0.08, $p = 0.71$) or resistant group (left 1.45±0.10 vs. right 1.18±0.05, $p = 0.20$). There were no differences observed in firing rate or randomness between hemispheres.

In addition, when focusing only on the left or right hemisphere and performing the group analysis again (see Table 3.1), we may conclude that the lower burst index in SIP rats may be more attributed to the left than the right hemisphere. The lower variability and the higher randomness seemed to be present in the left as well as in the right hemisphere. The higher overall firing rate was not present in the left or the right hemisphere alone but combining data from both hemispheres, and thus increasing statistical power, may have caused the difference to become significant.

Table 3.1: Group comparisons in the hemisphere-stratified analysis and the overall analysis in firing rate and firing pattern parameters.

		LEFT Mean±SEM	RIGHT Mean±SEM	Overall Mean±SEM
Firing rate	SIP	11.34±3.11	7.84±1.94	9.89±1.99
	RES	5.80±1.06	4.99±0.64	5.32±0.58*
	CON	6.99±1.10	6.93±1.68	6.95±1.02
Variability	SIP	0.79±0.07	0.86±0.08	0.82±0.05
	RES	1.45±0.10***	1.18±0.05*	1.29±0.05***
	CON	1.63±0.18***	1.17±0.06*	1.38±0.10**
Burst index	SIP	0.03±0.01	0.07±0.02	0.04±0.01
	RES	0.11±0.04***	0.06±0.01	0.084±0.02*
	CON	0.10±0.02***	0.07±0.02	0.082±0.01
Randomness	SIP	0.43±0.03	0.41±0.07	0.42±0.03
	RES	-0.10±0.08***	0.11±0.05*	0.02±0.05***
	CON	-0.03±0.06***	0.19±0.05*	0.09±0.04***

Data are depicted as mean ± SEM.
* Significantly different from SIP group at $p < 0.05$.
** Significantly different from SIP group at $p < 0.01$.
*** Significantly different from SIP group at $p < 0.001$.
BST, bed nucleus of the stria terminalis; SIP, schedule-induced polydipsia group; RES, resistant group; and CON, control group.

Table 3.2: Group comparisons in the antero-postero-stratified analysis and the overall analysis in firing rate and firing pattern parameters.

		Anterior BST Mean±SEM	Middle BST Mean±SEM	Posterior BST Mean±SEM	Overall Mean±SEM
Firing rate	SIP	4.05±1.10	13.10±2.88	12.60±7.34	9.89±1.99
	RES	4.42±0.87	5.20±0.88***	5.89±1.05	5.32±0.58*
	CON	4.71±1.82	8.09±1.45*	6.28±1.29	6.95±1.02
Variability	SIP	0.98±0.06	0.71±0.08	0.80±0.12	0.82±0.05
	RES	1.34±0.15*	1.15±0.04***	1.39±0.08***	1.29±0.05***
	CON	1.09±0.05***	1.36±0.06**	2.08±0.64**	1.38±0.10**
Burst index	SIP	0.04±0.01	0.05±0.02	0.03±0.01	0.04±0.01
	RES	0.06±0.01	0.06±0.01	0.12±0.04***	0.084±0.02*
	CON	0.06±0.02	0.10±0.02	0.04±0.02***	0.082±0.01
Randomness	SIP	0.36±0.04	0.45±0.05	0.47±0.09	0.42±0.03
	RES	0.08±0.10***	0.11±0.05***	-0.08±0.08***	0.02±0.05***
	CON	0.22±0.06***	0.04±0.05***	0.02±0.13***	0.09±0.04***

Data are depicted as mean ± SEM.
* Significantly different from SIP group at $p < 0.05$.
** Significantly different from SIP group at $p < 0.01$.
*** Significantly different from SIP group at $p < 0.001$.
BST, bed nucleus of the stria terminalis; SIP, schedule-induced polydipsia group; RES, resistant group; and CON, control group.

3.3.3 Correlations with position of the neurons within the BST

In the resistant group, a more lateral position of the recording resulted in a lower variability of the BST neurons, as well as a lower burst index ($p = 0.04$ and $p = 0.01$, respectively). When we compared all neurons from all groups, we observed a higher burst index with increasing (more ventral) depth of recording ($p = 0.02$). No other correlations were observed.

In addition, we performed an antero-postero-stratified analysis (anterior BST: B-0.00 to B-0.24, middle BST: B-0.36 to B-0.60 and posterior BST: B-0.72 to B-1.08). The results of this analysis are in accordance with the overall analysis (see Table 3.2). It may be concluded that the higher overall firing rate in SIP rats may be attributed to the middle part of the BST, and the lower overall burst index to the posterior part of the BST. The lower variability and the higher randomness seemed to be present in the anterior parts as well as in the middle and posterior parts of the BST.

3.4 Discussion

We investigated the single-cell activity of neurons in the bed nucleus of the stria terminalis in rats in an animal model for OCD compared to the activity in resistant and control rats. The study provides a summary of the BST firing properties under urethane anesthesia, which were not well described in the literature so far. Notably, we provide evidence for left-right differences in the firing patterns and a dorso-ventral gradient of the bursting index distribution.

3.4.1 Neuronal activity in the BST

Mean firing rates of control animals were similar to the values already reported in literature. Low firing rates are also reported by [29],[120],[101],[181]. Other BST firing properties are not extensively described in literature, which makes comparison difficult. A common way of evaluating the firing pattern of neurons is to make a classification in regular, irregular, and bursting neurons based on the interspike interval histograms [135]. However, due to the low firing rates of neurons in the BST, this was not possible. Instead, the variability, the burst index, and the randomness were used as parameters to describe the firing pattern.

The variability of the neuronal firing in SIP rats was lower than in control or resistant rats, suggesting a more regular firing pattern in SIP rats. However, the randomness was higher, which is an indication of more irregular firing [135] and more true spontaneous activity (in the sense of neuronal activity that is not related

in any obvious way to external stimulation [160]). Low signal-to-noise ratio, and thus errors in clustering, can occasionally affect some of the parameters extracted from interspike interval histograms, which are used in this study. It has been suggested that in this case, variability shows more robustness than, for instance, mean firing frequency [72]. Hence, in the interpretation of such ambiguous data, one may put more emphasis and weight on the variability parameter than on the randomness parameter.

This combination of low variability and high randomness is not a new observation. It was also found in olfactory receptor neurons in tracheotomized rats compared to freely breathing rats [51]. The tracheotomy was done to minimize the possible external effects/stimuli that might change the properties of the spontaneous activity.

Regarding firing rate and bursting behavior (respectively, higher and lower in SIP rats), there is only a significant difference between SIP rats and resistant rats, and not control rats. The decreased bursting behavior in SIP rats compared to resistant rats also suggests a more regular firing pattern in SIP rats. Generally, spike trains with a variability < 1 appear more regular, while a variability > 1 is often used as a marker for bursting activity [98],[51]. Indeed, we found less bursting behavior for the groups with mean variability < 1, i.e. the SIP group, compared to the control (not significant) and resistant (significant) group, which have a mean variability > 1.

The higher firing rate in SIP rats compared to resistant rats suggests that rats that are susceptible to the SIP model (and thus to developing obsessive–compulsive behavior) have a higher neuronal activity in the BST than rats that are resistant and not susceptible to the SIP model.

In some cases, unilateral deep brain stimulation is sufficient to relieve a patients' symptoms [168],[87]. In this context, a comparison of the neuronal activity in the BST between hemispheres was made. However, no major differences were found. The bursting behavior in rats in the SIP group in the right hemisphere was larger than in the left hemisphere, and the opposite was true in the control or resistant group. To our knowledge, no such left-right differences in the BST were described in the literature so far.

The BST consists of many subnuclei (based on their projection pattern and neurochemical identity) that have different functions [127]. This may be the reason for the relatively large variability in the results obtained. However, it was not possible to make an analysis per subnucleus, due to the limited amount of data points in some subnuclei. This is why a correlation with the position of the neurons within the BST was sought. Recently it has been shown that neurons projecting from the BST to the ventral tegmental area, which mainly reside in the ventral BST, have lower capacitance, higher input resistance, inward rectifying potassium

currents, and lack I_h currents [52],[91]. These properties suggest that these cells may be more easily excited by synaptic input. The low threshold spike activity in the ventral BST may result in increased bursting phenomena [55]. In this study we found indeed a higher bursting index with increasing (more ventral) depth of recording.

3.4.2 The BST in relation to OCD

Currently, lesions and pharmacological manipulations of the BST suggest roles in the physiology of stress, anxiety, food intake, social behaviors, pain, goal-directed behaviors, anorexia, and addiction. Despite the findings of [63] and [100], the BST has not yet been directly linked to OCD, although anorexia is often comorbid in OCD patients. Furthermore, anxiety is a cardinal symptom in OCD, leading to compulsions even when there is no imminent threat (anymore). A link to stress can also be made; one of the most popular motivational hypotheses of schedule-induced polydipsia attributes this behavior to a coping process. The stress related to the scheduled delivery of food pellets in the hungry rats in the current model leads to the compulsive drinking, which is interpreted as a means of reducing the aversive feelings [15],[16],[30]. In a functional magnetic resonance imaging (fMRI) study of OCD symptom provocation, activation of the amygdala was observed [14]. The basolateral part of this nucleus is the major source of afferents to the BST, and the central part of the amygdala is anatomically, neurochemically, cytoarchitectonically, and embryonically related to the BST [3]. However, the BST is more involved in the processing of anxiety-induced stimuli in opposition to the amygdala, which are involved in the processing of fear-inducing stimuli [106],[176].

Dysregulation of the serotonergic system has been implicated in the pathophysiology of OCD and has been suggested primarily on the basis of the effectiveness of serotonin reuptake inhibitors (SSRIs, e.g. fluoxetine, clomipramine) in alleviating obsessions and compulsions in patients, as well as in rats in the SIP model. The BST receives a fairly dense innervation by serotonergic afferents [28],[145] and multiple serotonergic receptor subtypes are expressed within this region. The function of serotonin in the BST is to dampen the activity (and, consequently, anxiety-like behavior) during exposure to threatening stimuli. However, changes in the balance of the function of BST serotonin receptor subtypes could alter the response of BST neurons to favor excitation and produce a pathological state of anxiety [74]. Our observations of higher firing rates in BST neurons in rats in the schedule-induced polydipsia rats compared to resistant rats also imply a higher neuronal activity in the BST in this OCD model. Furthermore, the BST may be an important site of action in the pharmacological (or other) therapies in the treatment of anxiety disorders including OCD.

Although currently SSRIs are the most effective treatment for OCD, still one third

of the patients do not respond to this medication [140]. The combination of atypical antipsychotics and SSRIs has been found to induce significantly larger improvement of symptoms in patients [40],[38],[175], but studies with dopamine agonist and dopamine reuptake inhibitors have shown exacerbation of OCD symptoms in some, but not all, patients with OCD [179]. Hence, besides serotonin also dopamine may be implicated in the pathophysiology of OCD. There is direct support for a role of dopamine in the pathophysiology of OCD from neuroimaging studies that show higher densities of the dopamine transporter along with a down regulation of the D2 receptors in the basal ganglia of OCD patients. Furthermore, an increased dopamine signaling in the cortico-striato-thalamic circuitry has been related to OCD [179],[39],[36]. As mentioned before, the BST has strong connections to this circuitry [46] and neuroimaging studies demonstrated the importance of this circuitry in the pathophysiology of OCD [156]. Also, the BST may process emotional and context-dependent stimuli and integrate these in the dopaminergic reward/motivation circuitry [88].

An emerging body of evidence supports the hypothesis that also a dysregulation of glutamate neurotransmission may contribute to the pathophysiology of OCD [169]. It has been suggested that a frontocortical hyperglutamatergic dysfunction underlies the cortico-striatal-thalamo-cortical abnormalities observed in imaging studies of OCD [156] and also animal models confirm the role of corticolimbic glutamatergic hyperactivation in patients with OCD [136]. BST appears to have a distinct glutamatergic population of projection neurons also evidenced by functional assays and the presence of mRNA of multiple vesicular glutamate transporter genes [65]. This population has been identified to play a key role in anxiety-like behaviors, under which OCD is classified [121].

3.4.3 General considerations

Although we started with a large group of rats that were trained in the SIP model, only few (21%) became polydiptic. A training period of 15 days on week days seemed appropriate [114],[82]. However, adding more training days or extending the duration of the training sessions [183] may solve this problem in future experiments.

The BST (more specifically the center part) is sexually dimorphic in terms of its size and neurochemistry, both in humans [26] and in rats [81]. Because the prevalence of OCD in humans is the same for both sexes, the gender of the rats was chosen to be male in order to have no interference with the changes in energy metabolism that occur during the estrus cycle of female rats [44].

We performed neuronal recordings in animals under general anesthesia. Although we realize that the neuronal activity could differ from freely moving awake animals, it is a great challenge to do awake recordings in this animal model. The rats are

highly excited and practical difficulties arise when trying to record neuronal activity (e.g. movement artifacts, loose connections). Thus, this study should be considered as a prerequisite for studies in freely moving animals, where neural activity could be correlated to OCD-like behavior (eating and drinking).

3.5 Conclusion

The presented findings suggest that rats in the schedule-induced polydipsia, which models compulsive behavior in humans, display changes in the firing behavior of BST neurons. Further research in freely moving animals and in imaging studies could give more insight in the neuronal circuitry of the obsessive–compulsive disorder and thus may be of great aid to optimize therapies for OCD patients.

Chapter 4

Surface electromyography (sEMG)

Surface EMG (sEMG) is a technique to measure muscle activity noninvasively using surface electrodes placed on the skin overlying the muscle [148]. High density surface EMG (HD-sEMG) is a recent improvement enabling to measure electrical muscle activity with multiple (more than two) closely spaced electrodes overlying a restricted area of the skin. Besides temporal activity HD-sEMG also allows to extract spatial information from EMG, thus expanding the possibilities to detect new muscle characteristics [50], for example, the evaluation of single motor unit (MU) characteristics. This chapter offers an insight of how sEMG and HD-sEMG can be utilized for various applications taking into account muscle physiology.

4.1 Human muscle physiology

Human muscles enable movement of the body, maintain posture, and circulate blood throughout the body. They also provide strength and balance. Human muscles consist of 10 to 150 mm long and 5 to 90μm diameter muscle fibers that are attached to the bones by tendons. Each muscle fiber is innervated by a single motorneuron that controls it by transmitting the commands from the central nervous system (CNS) in the form of firing pulse trains. Several muscle fibers are innervated by the same motorneuron, forming (together with it) a basic functional unit of the muscles, called the motor unit (MU). The number of fibers in each MU varies considerably within the same muscle and even more between different muscles [54]. The neurons going from the spinal cord to the muscle and innervating its fibers (MUs), are portrayed in Figure 4.1.

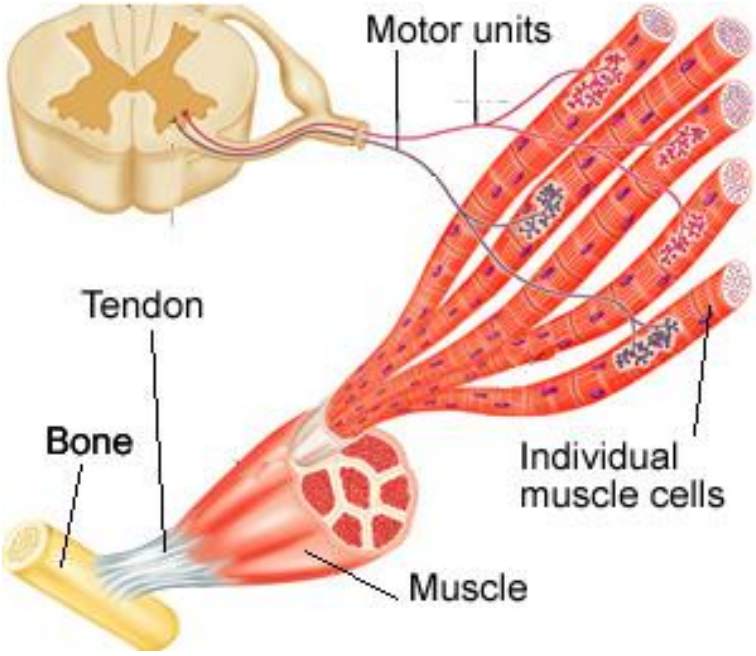

Figure 4.1: Control of the muscles from spinal motorneurons to muscle fibers [158]. ©Dynamic Science.

Electrical signals sent by the CNS propagate along a nerve fiber and terminate in a neuromuscular junction (NMJ) where they excite membranes of all innervated muscle fibers. Much like in neural spikes, every pulse in a motorneuron induces a local depolarization of the transmembrane potential of each muscle fiber, called the single-fiber action potential (SFAP). SFAP propagates without attenuation along the muscle fiber from the NMJ to the tendon endings (connections with the bone), causing the muscle fiber to contract. Process of SFAPs propagation are shown in Figure 4.2.

The sum of single-fiber action potentials corresponding to all the fibers of a single motor unit is called the motor unit action potential (MUAP). An example of motorneurons triggering fibers with pulse trains is depicted in Figure 4.3.

Depending on the contraction force controlled by CNS, up to several tens of MUs can be simultaneously active in the muscle tissue. Their MUAPs superimpose in time and space and form a highly complex interference pattern of EMG, which can be detected either within the muscle (with needle or intramuscular electrodes) or on the skin above the investigated muscles (with surface electrodes). Recording and analysis of these interference patterns can offer insight in many diseases related

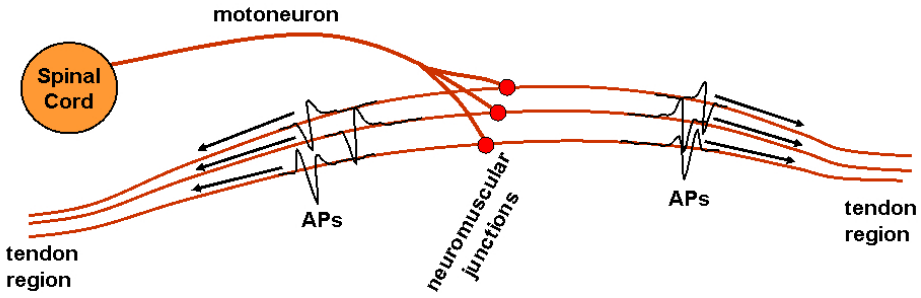

Figure 4.2: SFAPs traveling from NMJ to tendons following the received trigger pulse from a motorneuron.

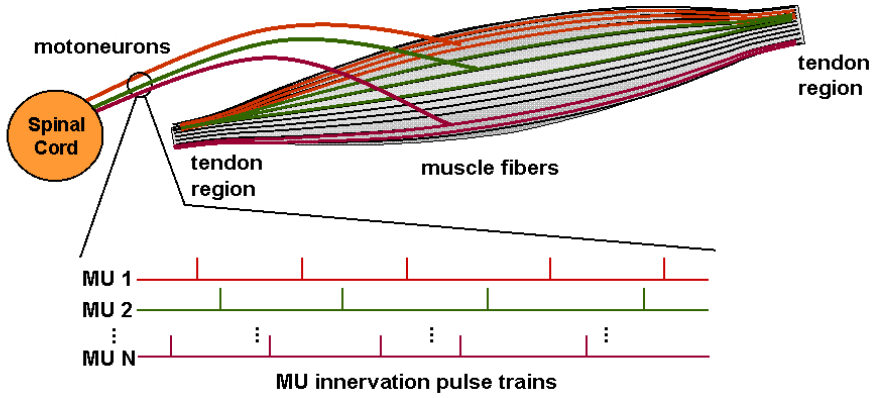

Figure 4.3: Motorneurons innervating muscle fibers (constituting MUs) and sending triggering pulse trains

either to controlling the nervous system or the muscles. It can also offer insight on how muscles behave in different conditions, what are the so-called recruitment strategies of the MUs and so on. Surface EMG increasingly becomes a popular non-invasive tool for a range of exploratory and some suggested treatment verification attempts.

4.2 Measuring electrical activity of the muscle

Usually the easiest way to observe individual MUs is through electrical properties of MUAPs. The ionic currents that flow upon the depolarization of the muscle cell membrane will cause a potential difference that can be observed. The passage of this potential through the rest of the tissue causes the filtering effect altering its shape. This "volume conduction" phenomena has been a topic of many modeling studies in the past (e.g. [152], [11], [58]) to assign physiological properties to the recorded observations. This electrical activity can be measured extracellularly using needle or surface EMG electrodes.

Needle versus surface EMG

The main difference between needle and surface EMG from the perspective of observed signals stems from the difference in conductivity between various layers of tissue: muscle, fat and skin. The complex volume conductor behaves like a spatial filter which alters the recorded signal (MUAP). The mentioned modeling studies aimed to describe how this spatial filtering changes MUAPs in order to interpret the observed EMG signals.

Needle electrodes offer the possibility to measure the action potentials of individual muscle fibers and MUs in vivo. Since the uptake area of these electrodes is small, only a part of the muscle can be seen by them.

Due to the mentioned volume conductor effect, it is not possible to measure signals from individual fibers on the surface. However, as all the fibers of single MU are activated simultaneously, their summated activity can be observed on the surface in the form of motor unit action potentials. Thus, needle EMG is more suitable for studies on the level of muscle fibers while surface EMG is oriented towards the motor unit level.

Neuromuscular disorders can affect muscle and/or nerve fibers. Needle electrodes are readily used today in the investigation of these disorders. For instance, denervation of the motor nerve will cause remodelling of motor units, known as collateral reinnervation [171]. This means that a number of muscle fibers will be innervated

by a nearby healthy nerve. This will cause the number of fibers associated with a healthy MU to rise, resulting in larger observed MUAPs.

Traditional use of surface EMG is in movement studies where the force the muscle produces is indirectly determined. When several electrodes are used, one of them is positioned on the part of the body that does not move and plays the role of the reference. This makes the electrode montage "monopolar". With the increasing force, the power of the EMG signal also increases. This happens partly due to the increased number of active MUs but also due to the increasing firing rate of the already active ones. Recordings from these traditional surface EMG systems generally do not allow observations of individual MUAPs due to complex interference patterns that emerge.

High Density surface EMG (HD-sEMG)

The initial and clinically accepted use of surface EMG electrodes was limited to a few applications, mainly nerve conduction studies ([131], [119]). The logical extension came with placing multiple electrodes in a line, resulting in a linear array recording ([57], [119]). This enabled for instance, the measurement of motor unit conduction velocity by comparing the time delay of consecutive signals, provided they are aligned with the muscle fiber direction ([102]). An example is shown in Figure 4.4 taken from ([57]). Here, the first spatial effect of the MUAP can be seen: origination at the endplate zone, propagation along the fiber and extinction at the tendon. The montage used here is bipolar, meaning that the recordings portray differences in potential of the nearby channels. The endplate zone (innervation zone) is characterized by low amplitudes (the two electrodes above the innervation zone (IZ) measure almost the same potential and thus, their difference is close to zero). Constant propagation along the fibers can be observed.

Further extension came in the form of 2D electrode arrays. Here, a large number of densely spaced electrodes over a muscle provide not only temporal but a spatial information as well on the motor unit action potential. Different grids with various inter-electrode distances (usually 3-10mm [171]) have been used, depending on the muscle ([12], [104]). Figure 4.5 shows some examples.

Recently developed flexible arrays (e.g. like the ones described in [104]) are employed frequently for HD-sEMG. The electrode configuration widely used in the research connected to this thesis is a flexible electrode grid made by Digiraster Tetzner GmbH (Stuttgart,Germany). This grid, placed over thenar hand muscles is shown in schematic Figure 4.6 and in reality in Figure 4.7. These 2D grids are often referred to as the high-density grids and using them constitutes the so-called high-density surface electromyography (HD-sEMG).

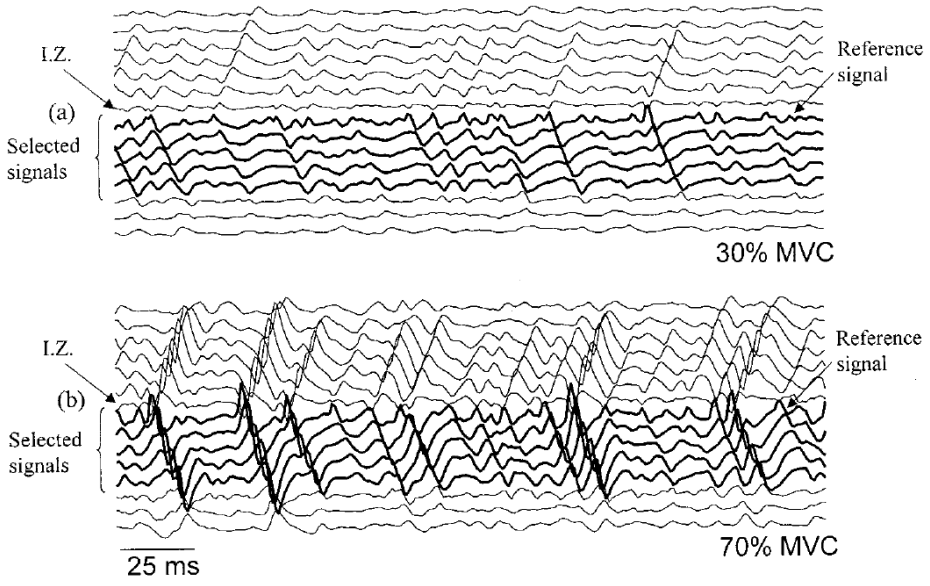

Figure 4.4: Signals detected with a linear electrode array of 16 electrodes (inter-electrode distance of 10 mm) from the biceps brachii of a healthy subject during (a) 30% maximal voluntary contraction (MVC) and (b) 70% MVC; the selected signals and the reference signal used for the estimation of CV distribution are shown. I.Z.: innervation zone. © [2000] IEEE

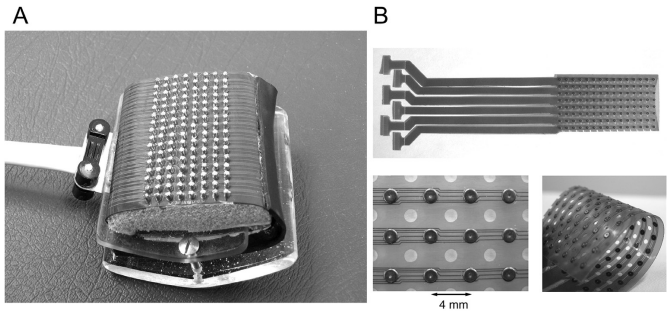

Figure 4.5: Two examples of high-density electrode grids are shown. a) For the hand muscle a grid with 8×16 electrodes gold coated serrated pins with a 3 mm inter-electrode distance. b) A flexible electrode grid; Figure taken from [171].

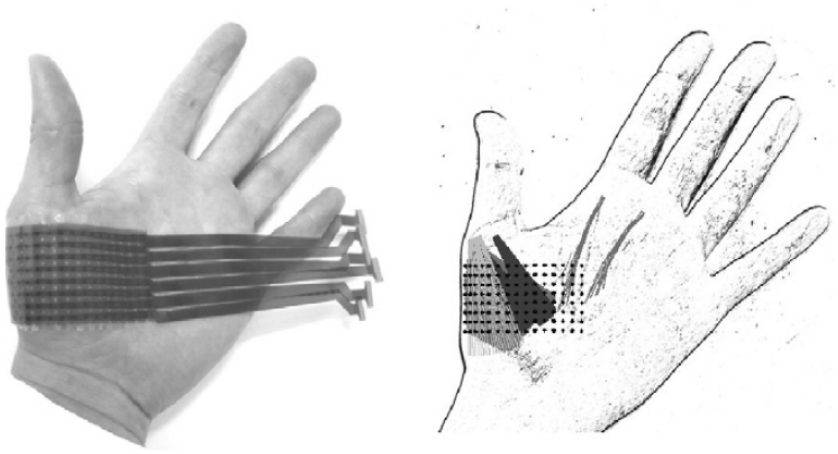

Figure 4.6: The flexible grid of 120 (8×15) electrodes used for high-density surface EMG recordings. The grid was placed transversally over the muscle belly and attached to the skin using double-sided adhesive tape with holes matching the electrode contacts. The right side of the figure illustrates the position and orientation of the muscles innervated by the median nerve. Figure adapted from [172].

The spatial dimension that is added reveals anatomical information of the muscle under study. It becomes possible to easily determine e.g. the location of IZ, conduction velocity, etc. Moreover, these high-density recordings enable the usage of modern signal processing techniques to disentangle the complex interference patterns into contribution of single MUAP trains. Once a single motor unit action potential is isolated, the monopolar montage may reveal other properties such as the length and orientation of the muscle fibers as well as (under certain conditions) the size of the motor unit [154]. In this case, signals are recorded with respect to a common, far-away reference electrode (not shown). Four examples how HD-sEMG can assist the motor unit size and depth are portrayed in Figure 4.8 adapted from [154]. Modeling of the recorded biceps brachii muscle MUAPs assisted in determination of the radial distance between the electrode array and muscle fibers.

4.3 Decomposition of HD-sEMG

With the large number of channels and mentioned topological and temporal features, it became possible to attempt the so-called decomposition of recorded EMG signals. Decomposition is a term used to describe disentanglement of the signal into



Figure 4.7: Picture of a flexible HD-sEMG electrode array placed over the thenar muscles used in a number of studies described in this thesis.

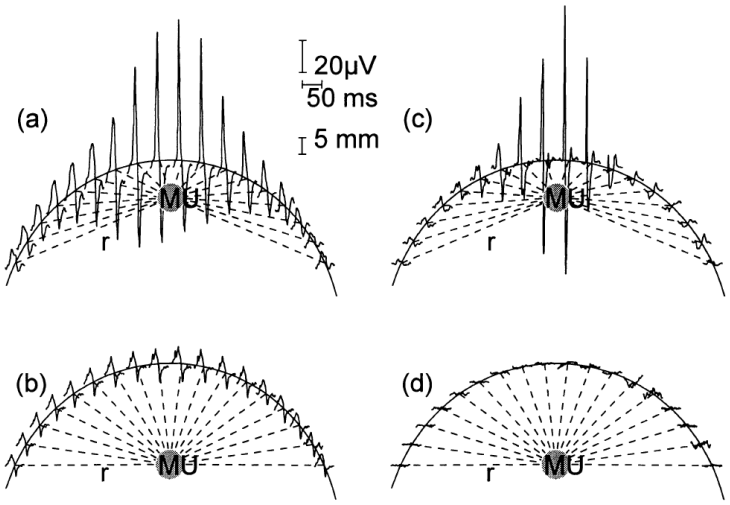

Figure 4.8: Cross-sectional impression of a superficial (a,c) and a deep (b,d) MUP signals recorded at 18 sites with different radial distances r from the MU are inserted. Reprinted, with permission from [154].

contributions of individual MUs. There have been a number of attempts to achieve full or partial decomposition, which is still a difficult task. This topic is treated in more details in Chapter 5.

Decomposition extracts the time instances when motorneurons fire a pulse causing SFAPs for each observed motor unit. This enables firing pattern analysis in various applications. Furthermore, decomposition provides the MUAP shapes of constituent MUs. The general outline of the signals generation, acquisition and decomposition results is provided in Figure 4.9.

Motor unit signatures By means of a decomposition it is possible to extract individual mean MUAP shapes. This is done, depending on the technique used to achieve decomposition, by some kind of averaging of the shapes that are assigned to the indicated MU. Since MUAPs are simultaneously observed from all HD-sEMG recording channels, they are sometimes referred to as the MUAP signatures or fingerprints. The underlying assumption of the decomposition effort and later analysis of MUAP signatures is that physiological differences of muscle fibers as well as the differences in relative positions of the fibers-electrode system, will make each MUAP signature observably different from others, allowing their discrimination.

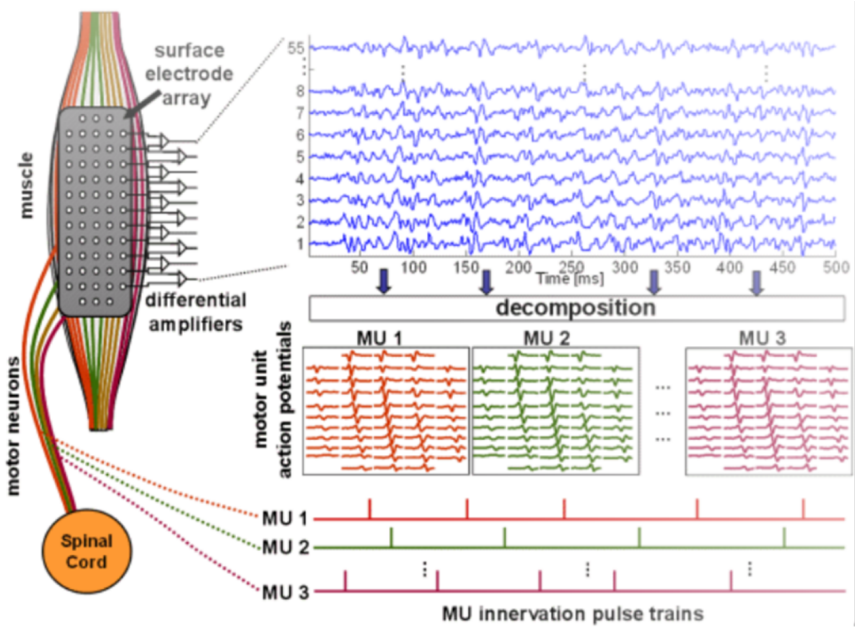

Figure 4.9: Schema of HD-sEMG signals generation (left), acquisition (top) and decomposition (bottom right).

On the other hand, individual MUAPs are assumed to preserve relatively constant or slowly evolving shape ([107], [132]). An example of 2 MUAP signatures of thenar muscles is portrayed in Figure 4.10 a) and b).

Extraction of MUAP signatures is a starting point of many applications using HD-sEMG, for example, determination of IZ and fiber conduction velocity.

Spatial filtering Various theoretical and simulation studies showed that modifying original signals by adding weights to the recording channels can ease the differentiation of MUAPs easing the process of decomposition and more. This is referred to as the spatial filtering. The schematics of the spatial filtering is shown in Figure 4.11. Here, w symbols represent the weights given to the channels before adding them to achieve signal modification. Here we focus at the modification of the middle channel. Other channels are similarly modified by moving the filter. Examples of a few frequently used spatial filters is shown through their filter matrices in Figure 4.12. All of the filters assume previously monopolarly recorded signals with far away reference electrode. The most basic spatial filter is the bipolar

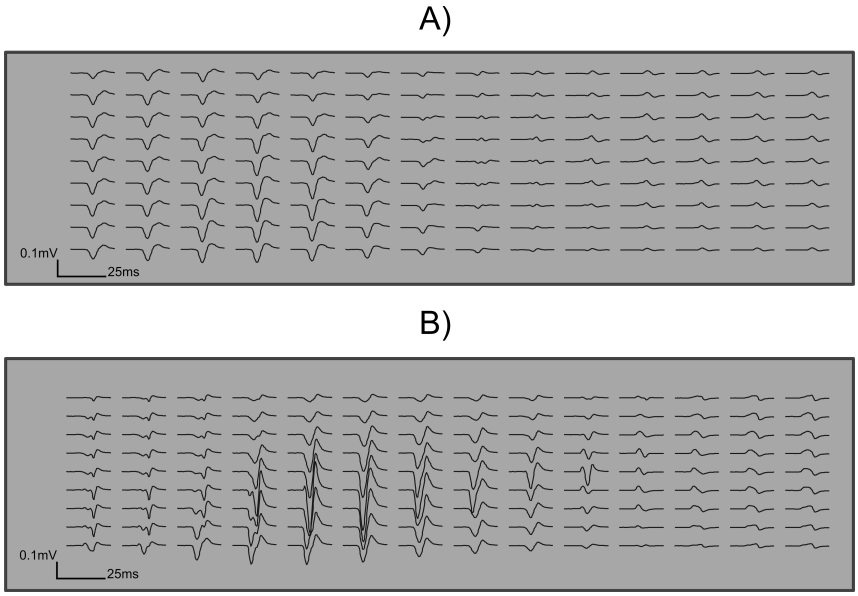

Figure 4.10: Two monopolar signatures extracted from thenar muscles voluntary contraction recordings.

filter where either rows or columns are subtracted to achieve filtering. The example of how bipolarly filtered MUAPs look like is portrayed in Figure 4.13 a) and b), for the monopolar observations in Figure 4.10 a) and b) respectively.

The effects of various spatial filters on MUAP discrimination has been treated previously, namely in [43], [56] and [105]. Known filters also used for image processing were employed either solely or in combination with each other. Also, it should be noted that these studies assumed (almost) dimensionless, equally spaced electrodes. Another type of filtering occurs as a consequence of the number and shape of electrodes. A spatial summation of electrical potentials over the surface of an electrode causes different effects that are observed. This question is raised in [58] and can point to construction of surface electrodes suited for purposes of particular studies.

4.4 Applications of surface EMG

A number of important studies rely on using high density surface EMG. The few most frequent applications are listed below.

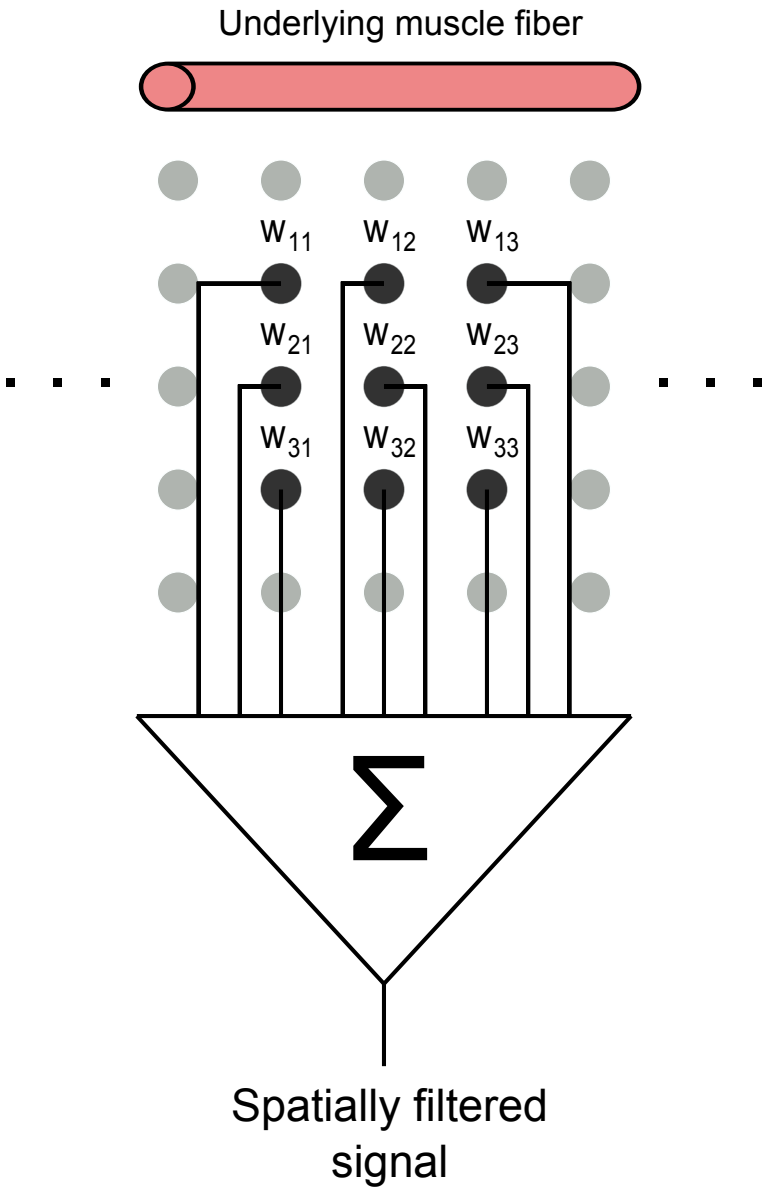

Figure 4.11: Achieving the spatial filtering of HD-sEMG signal; each recording channel is modified using surrounding channels; channels are multiplied with weight coefficients w and summed; the electrode grid is usually placed to coincide with the muscle fiber direction.

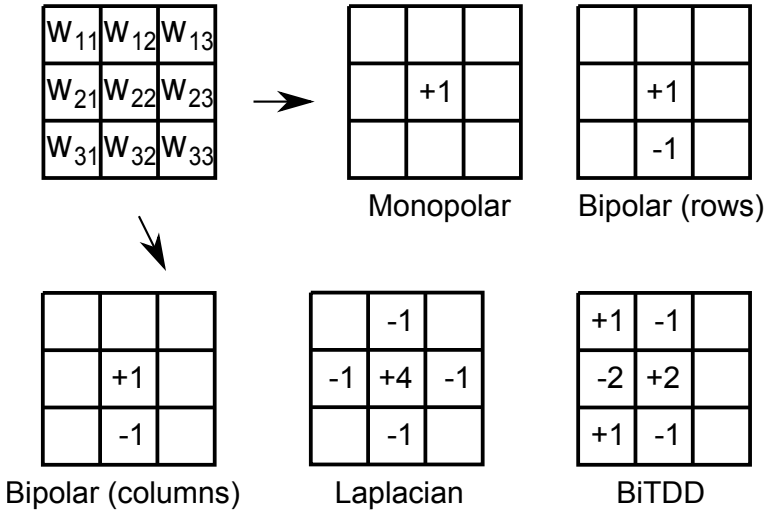

Figure 4.12: Some frequently used filter matrices described through their weight coefficients; it is clear that various ways to filter the signal use different number of electrodes; here BiTDD stands for bi-transversal double differential.

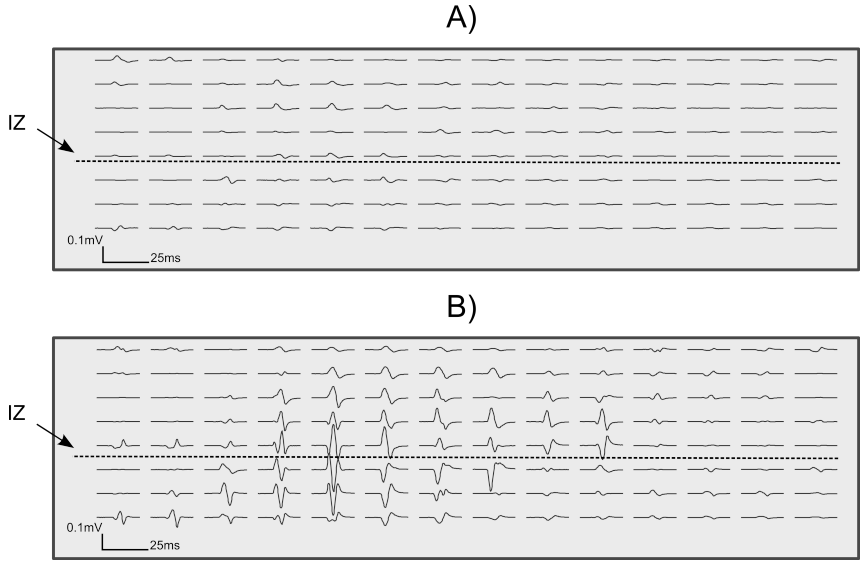

Figure 4.13: Bipolar signatures extracted from the monopolar montage in Figure 4.10; note that the IZ can be approximately estimated based on the reverse of polarity of MUAPs.

Motor unit tracking Following (tracking) individual motor units over time can provide important new insights, both into the relationships among various MU morphological and functional properties and into how these properties are influenced by neuromuscular disorders or interventions [115]. The electrode grid needs to be placed as accurately as possible between sessions to achieve this task, which represents a time consuming difficulty that can actually be bypassed using the technique described in Chapter 6. HD-sEMG can be used reliably enough to estimate whether MUAP shapes recorded in successive sessions could be considered as belonging to the same MU. So far, only a controlled stimulation-recording technique [115] has been used although decomposition assisted voluntary contractions were successfully treated as well recently [70].

Location of the innervation zone (IZ) Determining the location of IZ assists the non-invasive characterization of muscles in human body. Locating the IZ has become relatively easy assuming the individual MUAPs have been identified. In principle, using a bipolar filter to transform the signal automatically pinpoints the IZ as the area closest to the channel from which the propagation started. Manual and automated methods have long been suggested for this purpose. The logic behind this is that MUAPs recorded from the electrodes closest to IZ will almost cancel out in bipolar derivation, leaving close-to-zero signals near IZ. An example is provided in Figures 4.4 and 4.13.

Firing pattern related studies Many studies have dealt with how CNS activates muscle fibers in healthy individuals. With the help of a decomposition, it is possible to follow how MUs are activated with applying the force. Further, it is also possible to analyze the MUs not conforming to the usual firing patterns by analyzing timestamps provided by a decomposition like e.g. in cases of so-called fasciculations. Fasciculations are irregularities of muscle firing patterns which can be benign but can also be due to disease of the motorneurons. sEMG has already been used in these studies ([86]) and more recently HD-sEMG was also successfully employed ([49]).

Motor unit number estimation (MUNE) A number of muscle disorders and disorders of lower motorneurons (e.g. amyotrophic lateral sclerosis (ALS)) cause the affected person to gradually lose control over their muscles. To do follow-up studies assessing the state of the disease or the effect of possible medication would be of clinical value. HD-sEMG can assist this process by estimating the number of MUs that can be activated which is referred to as the motor unit number estimation (MUNE). MUNE has a history preceding the era of surface EMG but the non-invasive character and possibilities of HD-sEMG make it an attractive alternative. MUNE can be achieved either using voluntary contractions assuming

a reliable decomposition algorithm or by applying electrical stimuli of the muscle while recording the response; here, individual MUAPs can be obtained using the stimulation trigger time. This topic is well described in [171].

Force assessment To detect fatigue is important in designing ergonomic work stations, in planning appropriate work-rest patterns, and in preventing/assessing the progress of disorders [170]. For this and other purposes that need to assess muscle force, HD-sEMG can be readily used. Here, a number of parameters is used to estimate force, e.g. muscle fibre conduction velocity (CV), root mean square value (RMS), mean frequency of the power spectrum (MNF), fractal dimension (FD), entropy, etc.

4.5 Conclusion

HD-sEMG offers new insights in muscle physiology and shows a great potential for future research and possible medical applications. It presents a still developing technique that is a non-invasive alternative for studies of normal and irregular functioning of neuromuscular system. Many applications rely on having a reliable decomposition method that is still a challenging and not completely resolved issue. This problem is tackled in Chapter 5 where a new algorithm aiming towards this goal is presented.

Acknowledgments Presented Figures 4.2, 4.3 and 4.9 are courtesy of A. Holobar.

Chapter 5

A new and fast approach towards HDsEMG decomposition

The decomposition of high-density surface EMG (HD-sEMG) interference patterns into contribution of motor units is still a challenging task. We introduce a new, fast solution to this problem. The method uses a data-driven approach for selecting a set of electrodes to enable discrimination of present motor unit action potentials (MUAPs). Then, using shapes detected on these channels, the hierarchical clustering algorithm [123] is extended for multichannel data in order to obtain the motor unit action potential (MUAP) signatures. After this first step, more motor unit firings are obtained using the extracted signatures by a novel demixing technique. In this demixing stage, we propose a time-efficient solution for the general convolutive system that models the motor unit firings on the HD-sEMG grid. We constrain this system by using the extracted signatures as prior knowledge and reconstruct the firing patterns in a computationally efficient way. The algorithm performance is successfully verified on simulated data of medium/low contraction containing up to 20 different MUAP signatures. Moreover, we tested the method on real recordings from the lateral vastus leg muscle by comparing the algorithm's output to the results obtained by manual analysis of the data from two independent trained operators. The proposed method showed to perform about equally successful as the operators. This chapter is based on [68] and [69].

5.1 Introduction

Neuromuscular disorders can be roughly divided into neurogenic disorders, which are marked by a loss of functioning neurons, and myogenic diseases, which affect the muscle fibers. Both types have in common that they influence the shape of the action potentials that are generated in a muscle when its motor units (MUs) are activated [37], [50], [153]. These pathophysiological changes tend to be fairly specific for the underlying class of disorders. Therefore, estimating the shapes of the motor unit action potentials (MUAPs) is important for the diagnostic investigation and follow-up of such diseases [37]. Data on the firing patterns of these MUs provide information on the motor control strategies of the central nervous system and hence, a valuable additional perspective [48].

As described in Chapter 4, the non-invasive high-density surface electromyography (HD-sEMG) measures the volume-conducted electrical activity from the muscle on the skin overlaying this muscle using a grid of multiple densely spaced electrodes [12], [50]. MUAPs observed on such a grid vary not only between MUs but also from channel to channel. These spatial variations within a MUAP are generally sufficiently characteristic to allow discrimination between them. These MUAPs recorded with HD-sEMG constitute the mentioned MUAP signatures.

When a MU is active, it fires at fairly regular intervals, resulting in a train of repetitive MUAPs. This property supports the assignment of MUAPs to a specific MU. Detecting and classifying each firing of all MUs contributing to a recording is referred to as the full decomposition. To accomplish this, the overlapping mixtures of various MUAPs have to be "demixed".

Several studies aiming at decomposition have been proposed over the past decade (e.g. [33], [60], [61], [64], [94], [187], [188]). For a review of methods we refer to [123]. However, various problems concerning either automation, processing time, or the number of different MUAP signatures that could be extracted (usually not more than six per recording) remain and ask for new solutions. A more recent, promising approach for full decomposition is the so-called Convolution Kernel Compensation (CKC), reported in [85] and later verified in [84]. Another solution has recently been reported in [132], which was later used in [34]. However, none of these solutions is freely available for use in the research community.

In this study we introduce a novel approach towards the ultimate aim of full decomposition. Our automated method first extracts MUAP signatures of contributing MUs and then uses these shapes as prior knowledge for subsequent decomposition. In addition, we designed it to be computationally inexpensive, and due to its data-driven nature, it is compatible with multiple surface electrode configurations and equipment. The potential of the method is demonstrated both on simulated and real-life signals.

5.2 Methods

5.2.1 Algorithm

Outline of the algorithm

The algorithm comprises three major steps (see outline in Figure 5.1): detection of action potentials (spikes) (which can either be individual MUAPs or mixtures), clustering of similar spikes, and demixing. The goal of clustering is to group similar MUAPs originating from the same active MUs and obtain their mean shapes. The demixing stage provides the time instances (timestamps) at which each MU was active. The output of the algorithm is a set of MUAP signatures and their corresponding firing patterns.

The algorithm exploits the assumption that MUAPs come in trains and have a relatively constant, all-or-none signature on the recording grid. This allows us to cluster similar signatures generated by corresponding active MUs. However, the clustering step leaves many spikes unclustered due to overlapping of MUAPs from different, concurrently active MUs or (less often) appearance of insufficiently large sub-clusters (overclustering) that are not reliable as MUAP representatives. Therefore, in the third step, all of the detected shapes are passed through a demixing process, which assumes that each observation is a superposition of one or more previously obtained shapes and noise. The demixing is performed by minimizing the residue after subtraction of the estimated shapes at proper time lags.

Detection of spikes

The HD-sEMG array in our setup contains 126 electrodes, which record the signals relative to a far-away reference (i.e., we have monopolar recordings on 126 channels) [12]. Due to densely spaced electrodes, the information content of the signals from adjacent electrodes overlaps to a large extent. This allows using a limited set of electrodes for MUAP detection, one that optimally covers the grid and allows discrimination between different MUAPs. To select these electrodes in a data-driven way, individually suited for each signal, we propose a procedure that automatically detects where repetitive MUAP signatures are maximal. A vector is created by taking the maximal value of all recording channels for each sample. Thereafter, peak detection is performed on this vector to detect possible peak maxima. For each detected peak, the corresponding channel is stored. Channels that contain more than 1% of all detected peaks are used in the spike clustering step. These channels likely include the most prominent peaks of MUAPs. We refer to them as "clustering channels". Due to the phase shift of MUAPs on different electrodes, the set of clustering channels is over complete – one MU is often expected to contribute

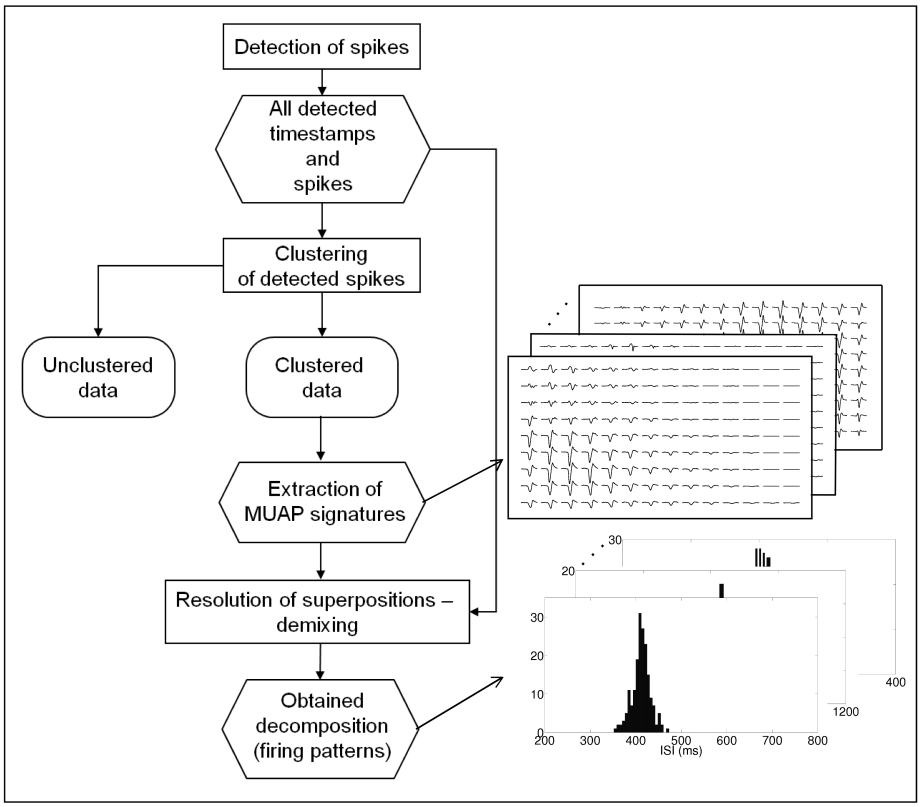

Figure 5.1: Schematic outline of the algorithm. Three major steps can be recognized: 1) spike detection, 2) clustering of spikes and extraction of MUAP signatures, 3) demixing superpositions and the recovery of interference pattern by using the MUAP signatures obtained in step 2.

more than one channel. For each of the clustering channels, time instances of peaks above the noise level are kept for clustering. This noise level was estimated using the median-based measure introduced in [47].

Clustering of spikes

For each detected spike, samples lying in an interval of ± 1.5 milliseconds around the detected peak are stored for each clustering channel. They are consequently concatenated to vectors which are then used as inputs for clustering. Multiple detections are excluded by introducing a detector-dead time (5ms) and treated

in the *demixing* stage. The amount of stored samples represents the empirically determined trade-off between the discriminatory information of the spike and the influence of possible MUAP summation (if multiple MUs are concurrently active).

Clustering of the input vectors corresponding to detected spikes is performed with a multichannel extension of the Wave_ clus algorithm [149] as reported in [68]. The algorithm returns clusters of very similar vectors and a set of nonclustered vectors that appear as outliers. The specific strength of this algorithm lies in the fact that it is unsupervised and that the number of clusters is automatically estimated, i.e. not a priori needed. Its strategy of classification using the nearest neighbor criteria additionally allows for gradual evolving of the shapes of cluster elements.

The algorithm employs hierarchical superparamagnetic clustering (SPC) [10] described in Chapter 1. SPC was originally used in statistical physics to describe ferromagnetic particle behavior thus owing its name to it. As described, the input data is modeled as a granular magnet, where each particle is assigned a spin. At very low temperatures, all the spins are aligned (ferromagnetic region). At very high temperatures, all the spins are random (paramagnetic region). An intermediate, superparamagnetic region is again the region of interest: at the right temperature, similar particles will have aligned spins revealing "natural" clusters. Limits of what is considered "natural" are defined by the specific application and controlled by tuning of the "temperature" parameter. This parameter determines the depth of differentiation of clustered elements – the line between having too many small clusters and merging elements from different classes. The tuning we employed for sEMG clustering emphasized the need to cluster as many shapes correctly and identify as many possible MUAPs. Another advantage of the clustering method is that also a group of unclustered shapes (usually mixtures of MUAPs) is formed without affecting the remaining clusters. Figure 5.2 shows an example of the detected spikes before (Figure 5.2 a) and after (Figure 5.2 b, c) clustering.

Once clusters have been identified, a number of the corresponding timestamps is attributed to individual MUs. This number of identified timestamps is dependent on the signal complexity - it usually decreases with higher contraction force. Averaging MUAP shapes (for which the length is predefined by the user) over these attributed timestamps (using median estimator) grants MUAP signatures for each MU. If 2 MUAP signatures exhibit high resemblance (correlation >0.95) they are identified as belonging to the same MU. Additional de-noising of these template MUAP signatures was obtained using the singular value decomposition (SVD) [17]. The SVD was applied on a matrix of MUAP shapes on all channels stacked below one another. De-noising is achieved by estimating the best rank-5 approximation using the SVD. These signatures will serve for attempted demixing of previously detected spikes. An example of a signature (red) and the associated MUAPs (blue) is shown in Figure 5.3.

Demixing of MUAPs

After clustering, a number of vectors remain unclustered. These include mixtures of MUAPs generated by two or more MUs, additionally corrupted by noise. With the prior knowledge of the obtained MUAP signatures as shown in *Clustering*, these shapes can be demixed by optimizing the fit between the sum of estimated shapes and a detected spike. In order to achieve this, we start from a model of how the activity of MUs is reflected on the recording channels.

Model of HD-sEMG recordings The motor neuron firing sequence can be represented as a pulse train of Dirac functions [85]. The surface EMG recording of active MUs is characterized by how activity from the muscle fibers is reflected on the recording electrodes after propagation through the tissue. This recording ($y_m(k)$,$m = 1 \dots M$, $k = 1 \dots K$, with M channels and K samples), will assume p ($p = 1 \dots P$) possibly active MUs. It can be mathematically expressed (similar to [1]) as the convolution (*) between streams of Dirac impulses (s_p) and their corresponding filters (h_{pm}):

$$\begin{aligned} y_1(k) &= h_{11} * s_1(k) + h_{21} * s_2(k) + \cdots + h_{P1} * s_P(k) + w_1(k) \\ y_2(k) &= h_{12} * s_1(k) + h_{22} * s_2(k) \cdots + h_{P2} * s_P(k) + w_2(k) \\ &\vdots \\ y_M(k) &= h_{1M} * s_1(k) + h_{2M} * s_2(k) \cdots + h_{PM} * s_P(k) + w_M(k) \end{aligned} \tag{5.1}$$

The recording is additionally corrupted by additive noise $w_m(k)$. Each s_p comprises Dirac pulses corresponding to time instances at which the central nervous system triggers the p-th MU (i.e. the MU drive) while the filters h_{pm} account for the p-th MUAP shape recorded on the m-th electrode.

We assume that during the length of the detected spike, each identified MU can be active at most once. Therefore, the activation vectors s_p have non-zero value each time when the MU fires, but can have a non-zero value at maximally one position during the whole length of one detected spike. The goal is, then, to detect the Dirac activations for each MU p, knowing the MUAP shapes (h_{pm}) a priori.

Solving the demixing problem In general, revealing the active MUs and the time positions of the activations during an observed spike is computationally very demanding. It would imply estimating all possible combinations of MUAPs with all

possible mutual delays, so that the derived solution corresponds to the observation (recordings). We aim at introducing a simplified algorithm that determines the solution. We start from expressing the convolution relation in a compact matrix representation, by introducing matrices H_{pm}:

$$H_{pm} = \begin{bmatrix} h_{pm}z_{2L-2} \\ circshift((h_{pm}z_{2L-2}), 1) \\ \vdots \\ circshift((h_{pm}z_{2L-2}), 2L-2) \end{bmatrix} \tag{5.2}$$

Each row represents a shifted MUAP from the p-th MU recorded on the m-th channel, h_{pm} denoting this MUAP shape of predefined length L. Here, z_{2L-2} is a zero padding vector of length $2L-2$ (denoted in a subscript) allowing to shift shapes, while $circshift(X, i)$ is an operator performing circular shifting to the right of shape X for i samples. Matrices H_{pm} have the size: $(2L-1) \times (L+2L-2$. All possible delays are accounted for by adding zeros (zero padding) before and after the spike shape (filling in the remaining $2L-2$ entries); i.e. if the p-th MU is active at position l, then the l-th row of the H_{pm} matrix will model the delay.

We simplify this optimization problem in three ways. First, we perform the optimization only on a selected, discriminative subset of channels. Second, we reduce the complexity of the problem further by using a vectorized concatenation of selected channels. Finally, instead of a simultaneous search for active MUs, we propose an iterative approach. Those steps are explained below.

We propose to reduce the number of channels: each of the P identified MUs will contribute only one channel – the one having the maximal peak of its MUAP signature, resulting in P demixing channels. MUAP shapes from these channels, $h_{p1}, h_{p2}, \ldots h_{pP}$ are then concatenated separated by zero padding vectors z_{L-1}: $[h_{p1}z_{L-1}, h_{p2}z_{L-1} \ldots h_{pP}z_{L-1}]$. The vector z_{L-1} prevents overlapping of the shapes (2 shapes originating from single MU coming in the same window of length L). These concatenated shapes are shifted in the same fashion as in Equation 5.2, forming a matrix $H_{p\prime}$ for each unit p:

$$H_{p\prime} = \begin{bmatrix} (h_{p1}z_{L-1}, h_{p2}z_{L-1} \ldots z_{L-1}h_{pP}z_{2L-2}) \\ circshift\left((h_{p1}z_{L-1}, h_{p2}z_{L-1} \ldots z_{L-1}h_{pP}z_{2L-2}), 1\right) \\ \vdots \\ circshift\left((h_{p1}z_{L-1}, h_{p2}z_{L-1} \ldots z_{L-1}h_{pP}z_{2L-2}), 2L-2\right) \end{bmatrix} \tag{5.3}$$

This step replaces M matrices in Equation 5.2 for each unit p by a single matrix $H_p\prime$, combining the information from all the P demixing channels.

Next, we reduce the recording output of each spike to a single vector. This we refer to as an observation vector (**Ov**). It is – in analogy with the formation of the filter representation Equation 5.3 - obtained by concatenation of spikes observed on P preselected channels interleaved by zero padding vectors z_{L-1}: $\mathbf{Ov} = z_{L-1}y_{p1}z_{L-1}\ldots z_{L-1}y_{pP}z_{L-1}$, where y_{pi} stands for the i-th channel selected for demixing. These spikes can either belong to a single, or to a mixture of more than one MU. Fitting the introduced model to the recorded data (**Ov**) solves the demixing problem.

The identification of constituting MUAPs is achieved in an iterative way. For each detected MUAP, the observation vector **Ov** (in concatenated form) is multiplied with each $H_p\prime$ matrix resulting into the vectors ($H_p\prime \cdot (\mathbf{Ov})^T$). The matrix $H_{p*}\prime$, corresponding to the vector having the maximum entry over all $H_p\prime$ matrices, is the one corresponding to the most likely unit $p*$. The row where this value is found reveals the appropriate delay - non-zero entry of s_p vector in the original model (Equation 5.2). In case where multiple units are present, the corresponding row of of the first identified MUAP is subtracted (peel-off procedure) from the original **Ov**. This updated **Ov** is used in the next iteration to detect the next most prominent unit. The maximum value of product $H_p\prime \cdot (\mathbf{Ov})^T$ favors the largest shape in a possible mixture in every step, minimizing the errors of subsequent steps.

The noise-level parameter **Rg** is defined for the recording as follows:

$$\mathbf{Rg} = \sqrt{\sum_{all\ channels} noise_estimate^2 \cdot L} \tag{5.4}$$

Noise estimate is calculated for each channel as defined in *demixing* stage using the median estimator described in [47]. After each iteration, the sum of RMS of residuals on all channels is calculated. If it is smaller than Rg, it means that the residual is below the noise level, and a successful decomposition has been achieved. For each identified MUAP, timestamp is assigned to corresponding unit's firing pattern if its peak falls in the area $\pm 5ms$ around the initially detected spike.

The computational process is depicted in Figure 5.4.

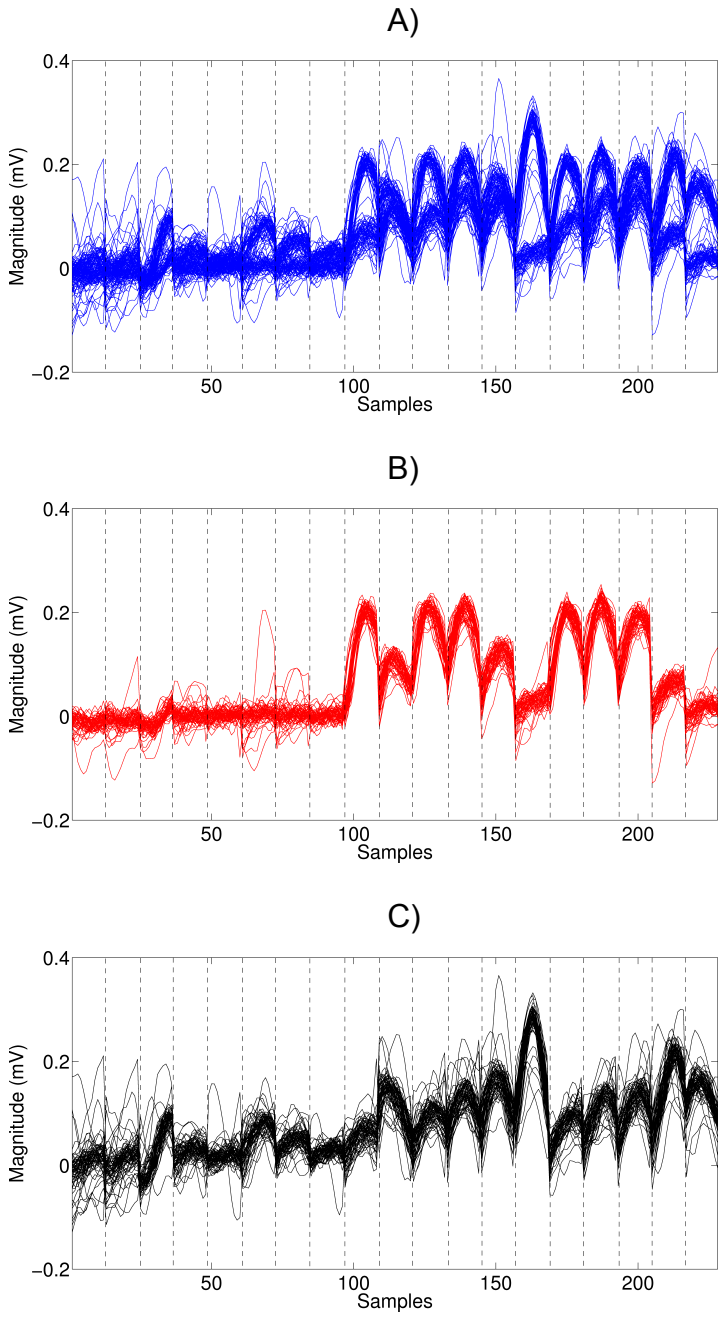

Figure 5.2: Example of clustering. a) Overlapped and aligned input vectors based on concatenated spikes from 19 clustering channels. b) and c) Clustering places the detected spikes accurately into two distinct groups with small intragroup variability. The vector data in b) can therefore be assigned reliably to a different MU than those in c).

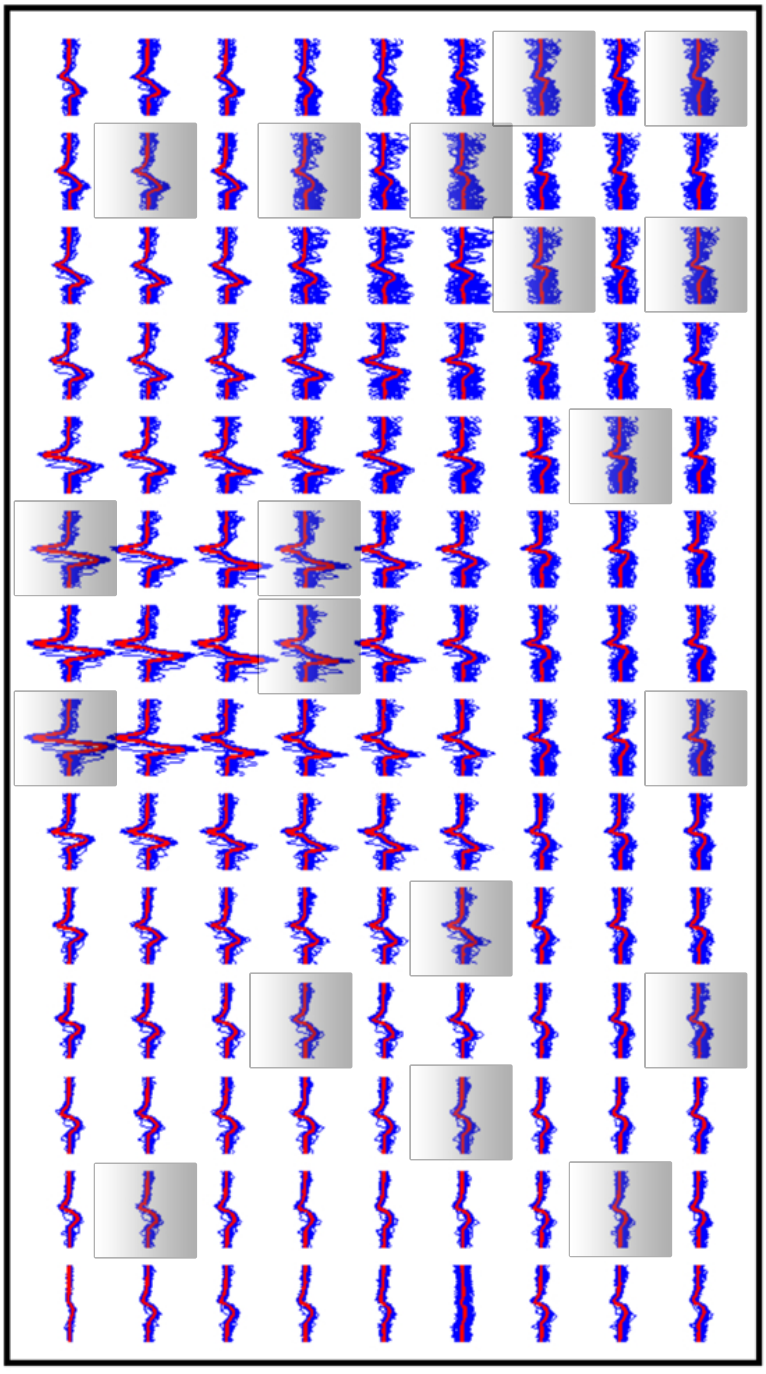

Figure 5.3: An example of overlaid MUAPs belonging to the same MU (blue) together with the median shape in red (signature). Median shape is unaffected by a single misclassified MUAP (also visible); Clustering electrodes are marked in grey

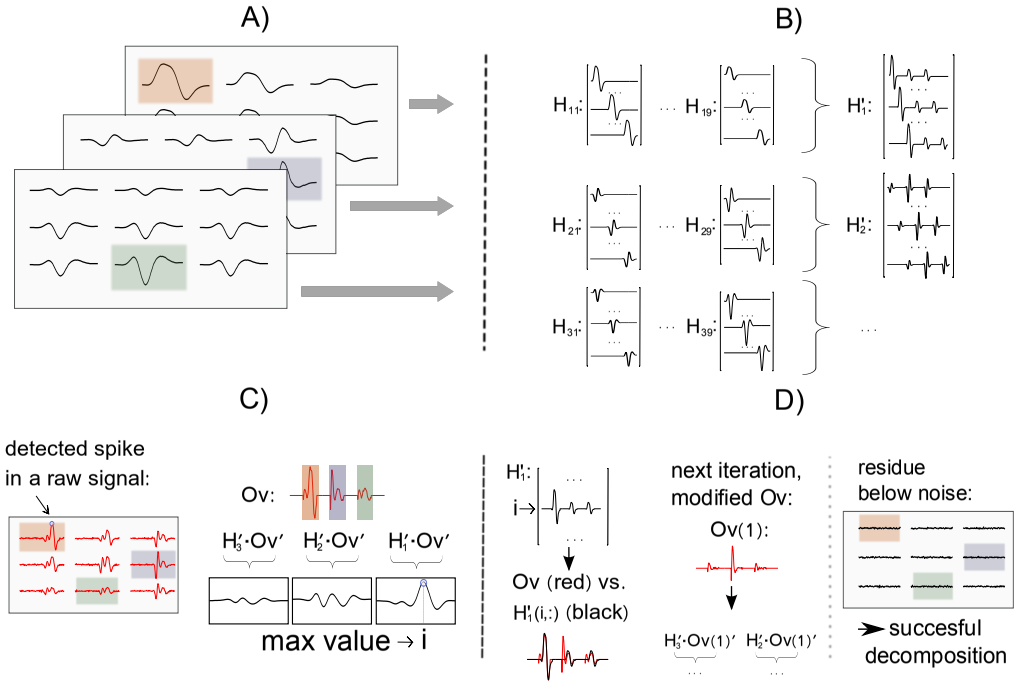

Figure 5.4: Toy example of demixing algorithm; a) Each identified MUAP signature contributes one electrode for demixing (marked using red, blue and green colors); b) Filter matrices (H_{pm}) corresponding to p-th MUAP shape recorded on m-th electrode are combined into a single $H_p\prime$ matrix for representing the p-th MU using concatenations of P demixing channels separated by zero padding; c) For each detected spike, observation vector (**Ov**) is created from raw signals by concatenation of spikes on demixing channels; thereafter, the most likely candidate MUAP is identified by the maximum of the products of all $H_p\prime$ matrices and transposed **Ov**; this maximum reveals the first MUAP ($p*$) to be peeled off while the position of this maximum (i) reveals adequate shape delay (row of the H_{p*} matrix); d) **Ov** vector is modified (**Ov**(1)) by subtraction of identified row of $H_{p*}\prime$ matrix from **Ov** and the next iteration is performed; once the residue falls below the noise level, a successful decomposition is obtained and the next timestamp is subjected to the demixing process.

5.2.2 Data

Simulated data

The proposed algorithm was validated using MUAP shapes obtained from HD-sEMG recordings of voluntary contractions of the thenar muscles [16]. Recordings were obtained using a flexible surface array of 126 Ag-AgCl electrodes (9 rows and 14 columns) with a diameter of 1.5 mm and the center-to-center electrode distance was 4 mm in both directions [104].

The obtained MUAP shapes with mutual correlation up to 0.95 were kept and used for creation of simulation signals. Firing sequences were simulated to obtain a sEMG interference pattern. The simulated interspike intervals followed a Poisson distribution with mean MU firing rates of 5, 10 or 20Hz. Interference patterns based on contributions from 3 to 20 active MUs (in increments of 1 MU) were created. For each set of generated spike trains (and template MUAP signatures) this resulted in 18 different signals – the first containing three and the eighteenth containing twenty different MUAP signatures. The duration of the simulated signals was 20 seconds and the sampling frequency was set to 4096Hz. Four of these sets were created for each mean firing rate (5, 10 or 20Hz).

Additionally, Gaussian noise was added. Realistic noise level was estimated from real recordings of thenar muscles [70] giving an average noise of $5\mu V$ root-mean-square (RMS) power. Two levels of noise are used to check the equipment-noise resilience of the algorithm. The first simulation is performed with this estimated, realistic level of noise ($5\mu V$). In the second simulation, the noise level of twice this size ($10\mu V$) is exploited. The resulting signals were low-pass filtered at 1000Hz with a fourth order Butterworth filter. Each data set was coupled with each of the noise levels. Signal-to-noise ratio (SNR) was calculated as $20 * \log_{10} \frac{MUAP_{power}}{Noise_{power}}$(dB). The mean SNR values of MUAP signatures were (15.14 ± 3.03) dB for 5 and (3.31 ± 3.03) dB for $10\mu V$ noise level respectively. Overall, 432 signals (2x3x18x4) were used for evaluation of the algorithm.

Real-life data

In addition to the simulation study, we also show the performance of the new algorithm on 20-second long low force voluntary contraction recordings from the lateral vastus leg muscle, an HD-sEMG data set that was previously reported in [95]. In short, eleven healthy volunteers, 6 males and 5 females, aged 20–29 years participated in the study. To obtain a stable interference pattern during an isometric contraction, the subjects were seated with the knee flexed at 90° and visual feedback of force was used. Target force was varied between 1% and 10% MVC. In this study, the 5-s long middle sections of recordings have been manually

analyzed by two independent, trained operators with the goal of achieving reliable identification of MUs and recovery of their firing patterns. This was possible for 9 subjects (datasets 1-9), with contraction force varying between 1 and 4% MVC. After processing signals from these recordings using our algorithm, the results on these 5-s mid-section intervals were the subject of performance evaluation compared to the operators.

The inter-operator agreement was very high (in 20 out of 25 identified units it was above 95%, the lowest being 63% on a single unit), suggesting that the manually detected firing patterns could be used as a standard for our evaluation.

The main features of the acquisition have been described in detail elsewhere [12], [95]. In short, the electrode array consisted of 10×13 electrodes with center-to-center electrode distance of 5 mm in both directions. Sampling frequency was 2000 Hz and the data were band-pass filtered (3-400Hz). After A/D conversion, a high-pass Butterworth filter of order 6 with cutoff frequency of 10 Hz was used to further reduce the baseline drift.

Because SNR values for the lateral vastus recordings are lower than those of thenar recordings, bipolarly filtered data were used. Bipolar signals were obtained by subtracting the signals from adjacent electrodes in the muscle fiber direction. After the clusters were identified in the bipolar signals, the “maximal peak" channel was selected for each cluster as described in earlier *demixing* stage, and these sets of channels were used for the demixing process. The noise level was estimated using the method described in [9], being between 5-40 and $0.5 - 15\mu V$ for monopolar and bipolar representations respectively.

5.2.3 Validation

To verify the quality of our analysis, temporal and spatial matching parameters were introduced. Temporal parameters, %complete (MUAP train) and precision, defined as in formulae 5.5 and 5.6, were used to assess the quality of interference pattern reconstruction.

$$\%complete = \frac{number\ of\ correct\ assignments}{number\ of\ correct + number\ of\ missed\ assignments} \quad (5.5)$$

$$precision = \frac{number\ of\ correct\ assignments}{number\ of\ correct + number\ of\ incorrect\ assignments} \quad (5.6)$$

Tolerance of 5 samples ($\sim$ 1ms) has been taken into account when calculating temporal parameters to account for the effect of noise. Spatial quality, used to describe the reconstruction of MUAP signatures, was estimated using 2 parameters: normalized root mean square error (NRMSE) and correlation coefficient. Each of the signatures obtained by clustering is aligned and compared with the actual shape using these two measures: only if a signature obtained by clustering exhibits a low NRMSE and high correlation at the same time, it can be considered as successfully reconstructed. NRMSE is calculated using formula 5.7, where $\hat{x}$ represents the estimated shapes obtained by clustering, and x the template (exact) forms. Summation is performed over all samples and channels.

$$\mathrm{NRMSE} = \sqrt{\frac{\sum (\hat{x} - x)^2}{\sum x^2}} \tag{5.7}$$

In case of the simulated signals, exact values for timestamps and template shapes were available. For the real datasets that were used, template MUAP signatures were calculated as the median forms obtained from timestamps grouped in clusters by operators. Similarly, timestamp values marked by the operators were taken as a gold standard for the comparison.

5.3 Results

5.3.1 Simulated data

The simulated datasets were decomposed in a fully automatic way. On average, 18 channels (5-25) were used for detection/clustering. Execution time for decomposing a 20 s dataset was between 5 and 15 minutes on an office desktop computer (Intel Core 2 Quad processor at 2.66 GHz with 4 GB of RAM).

The performance of the algorithm showed no statistical difference between the used noise levels (Wilcoxon rank sum test, $p = 0.78$). This came as a consequence of MUAPs being higher above this level for thenar muscles being close to the skin surface and pointed out that the instrumentation noise is not the main bottleneck of the decomposition attempt. Thus, all the results from signals differing only in the noise level were merged for further analysis. Figure 5.5 shows the average percentage of detected and properly classified MUAP signatures for different mean firing rates. Blue, black and red lines represent the mean values while grey areas around the curves indicate the range of all obtained results.

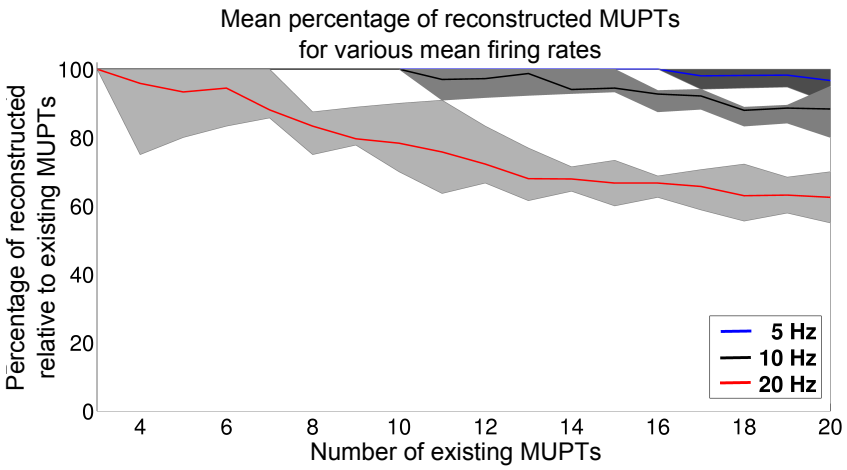

Figure 5.5: Mean percentage of reconstructed MUAP trains (MUPTs) as a function of mean firing rate and the number of present active MUPTs; mean values are shown in blue, black and red colors (for 5, 10 and 20 Hz mean firing rates) while all the obtained results are contained within the grey areas.

The %complete and precision of the analysis were evaluated after both the clustering and demixing steps. The sensitivity values as a function of firing frequency and number of active MUs are given in Figure 5.6, a-c. Mainly in the case of lower firing rates,%complete sharply increases after demixing. For 5 Hz mean firing rate, %complete reaches average values of $85-95\%$. However, %complete decreases with the increasing firing rate and the number of present active MUs. At 20 Hz level, the %complete after demixing offers less improvement mainly because not all MUAPs are identified (Figure 5.6 c). The precision before and after demixing was in the range of 0.9 to 1 for the 5 Hz mean firing rate. Despite these consistently high values, there was still a difference between the precision before and after demixing. This means that the demixing process decreased the number of wrongly classified units. However, with the increasing firing rate, precision drops and the clustering slightly outperforms demixing. The average values (over all signals containing the MUs with same mean firing rate) for precision across different firing rates (mean $\pm$ std) are given in Table 5.1.

All of the detected MUAPs appearing in large clusters (containing at least 30 elements) were successfully reconstructed. Clustering errors included misclassifications (incorrect assignments) and overclustering (dividing shapes originating from single MU in multiple clusters). While misclassifications were not frequent (indicated by high precision), the algorithm sometimes overclustered the data, leaving up to 3 smaller clusters corresponding to single MU (with correlation

Table 5.1: Average (over all signals of MUs with same firing rate) quality of spatial reconstruction for different mean firing rates (mean ± standard deviation) expressed as Pearson correlation coefficient and the normalized root mean square error (NRMSE). Values of precision after clustering and demixing procedures are also portrayed.

	Mean firing rate		
	10Hz	15Hz	20Hz
Correlation	0.99±0.01	0.98±0.02	0.94±0.04
NMRSE	0.06±0.03	0.19±0.10	0.40±0.17
Precision Clustering	0.94±0.04	0.93±0.04	0.87±0.04
Precision Demixing	0.96±0.04	0.91±0.05	0.82±0.05

between signatures >.95). However, these were successfully merged based on similarity.

The averaged values for the spatial reconstruction parameters (correlation and NRMSE) are also shown in Table 5.1. As comparison, the mean mutual NRMSE between the MU signatures used for simulation was 1.38 ± 0.53 (range 0.44-5.63). While increasing the number of units had only a marginal effect on these values (not shown), increasing the mean firing rate decreased the quality of reconstruction.

5.3.2 Real data

In the nine investigated subjects, two trained investigators found 25 reliably identified MUs [95]. Our automated method extracted 24 of these; 1 unit was not detected. Following the described approach, between 7 and 26 electrodes were used for clustering. Fig. 5.7 shows a typical example of monopolar and bipolar signal representations. In bipolar setting, physiological noise is significantly reduced assisting the decomposition effort.

Spatial matching between the operator and program extracted shapes was very good, thereby confirming a successful reconstruction of all identified MUAP signatures. Measures of the temporal aspects of the spike trains were mostly good (average %complete and precision > 0.9). Precision and %complete dropped in the presence of very low SNR units (see, e.g., Subject 3) and/or combination of low SNR and similar signatures (e.g. Subject 6, MUs 16 and 18). In all of the cases where attributed firings matched these reported by the operators, the maximal difference was within 3 samples, although the algorithmic tolerance allowed was equal to 5. The performance of our algorithm was compared in detail against the classifications agreed by both operators and the results are summarized in Table 5.2.

Table 5.2: Comparison of automatic decomposition program and the operators; each of the MUs indicated by the operators was compared in terms of the quality of reconstructed MUAP signatures and the associated firing patterns. * denotes the unit not found using the program.

MU	Subject	Force	SNR	Firings		Temporal		Spatial	
		(%MVC)	(dB)	Program	Operators	%complete	Precision	Correlation	NMRSE
1	1	1	-7.86	39	47	0.83	0.94	0.94	0.48
2	1	1	-5.37	38	45	0.84	0.90	0.90	0.36
3	1	1	-3.56	21	25	0.84	1.00	0.95	0.39
4	1	1	-3.80	26	30	0.87	0.95	0.94	0.45
5	1	1	3.53	47	49	0.96	1.00	0.99	0.12
6	1	1	-1.41	19	25	0.73	0.89	0.95	0.27
7	2	1	-3.56	53	42	1.00	0.92	0.95	0.21
8	2	1	-2.86	30	38	0.79	1.00	0.85	0.42
9	2	1	-6.47	45	42	0.90	0.85	0.83	0.56
10	3	1	-10.60	31	35	0.86	0.97	0.97	0.24
11	4	2	-8.19	43	46	0.91	0.98	0.99	0.10
12	4	2	12.26	28	27	1.00	0.96	0.95	0.23
13	5	1	-3.46	32	31	0.94	0.91	0.97	0.23
14	5	1	-3.59	39	39	0.95	0.95	0.97	0.21
15	5	1	2.11	51	51	1.00	1.00	0.98	0.12
16	6	1	-4.58	43	24	0.67	0.37	0.93	0.39
17	6	1	-4.09	24	23	0.96	0.92	0.96	0.38
18	6	1	-2.24	41	40	0.85	0.83	0.98	0.20
19	6	1	11.76	35	35	1.00	1.00	0.97	0.29
20	7	1	-4.04	32	35	0.86	0.94	0.84	0.36
21	7	1	-4.41	*	40	*	*	*	*
22	7	1	0.47	38	41	0.93	1.00	0.89	0.23
23	8	4	3.01	49	45	0.96	0.88	0.98	0.22
24	9	1	-3.79	31	40	0.78	1.00	0.92	0.29
25	9	1	-3.47	49	49	1.00	1.00	0.96	0.27

To illustrate how well the signatures of the MUAPs after decomposition matched those detected by the operators, Figure 5.8 presents both signatures for MU # 9 from Table 5.2, the unit with the lowest correlation value compared to the template (0.83; NRMSE=0.56). The relatively low value is mainly due to noise corruption in the channels where the signature is coming out of noise level. Several additional MUAP trains were also found by our program, but were excluded from the analysis since they were not marked by the operators.

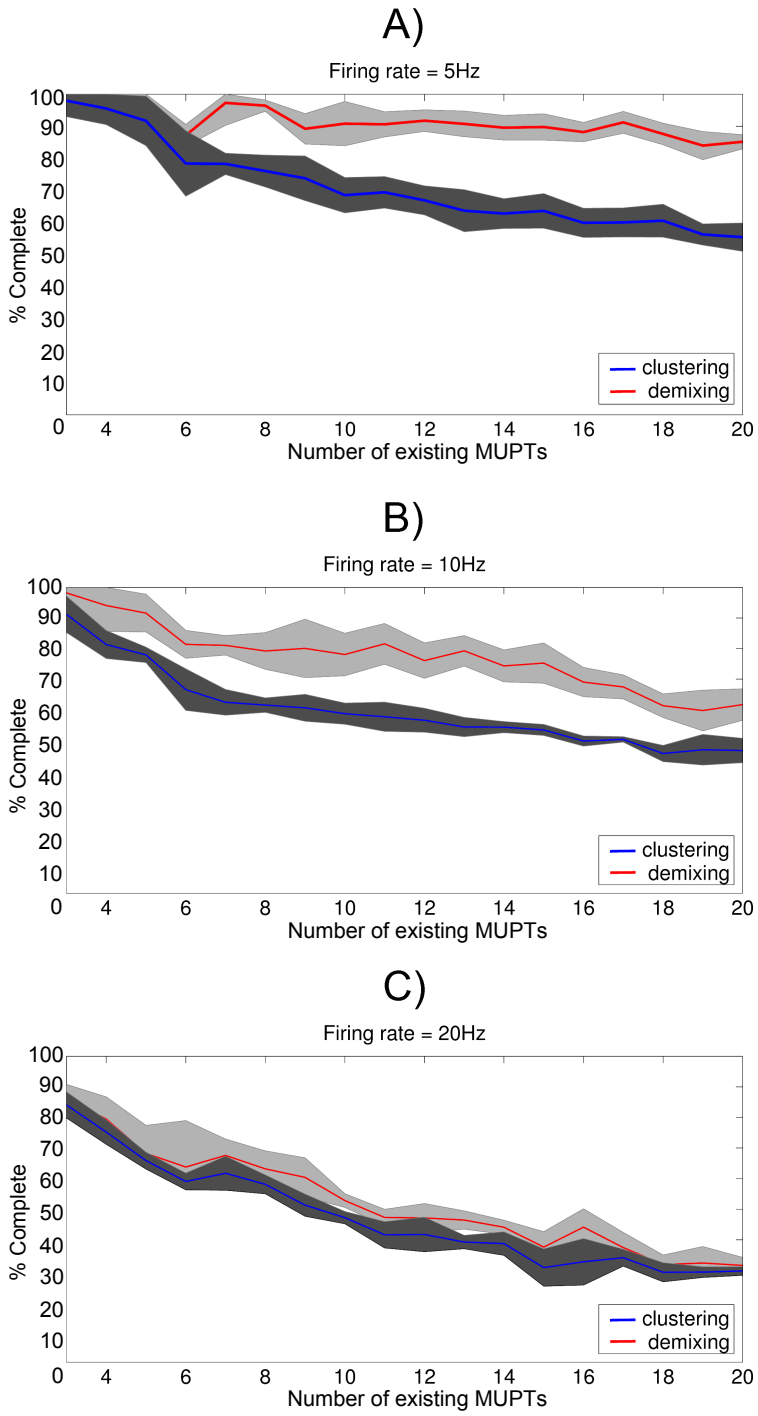

Figure 5.6: Effect of (additional) demixing on the %complete of identified MUs' trains for 5, 10 and 20 Hz mean firing rate as a function of number of present active MUPTs (a-c respectively). Mean values are shown in red (demixing) and blue (clustering). Grey areas around the mean values portray the standard deviation.

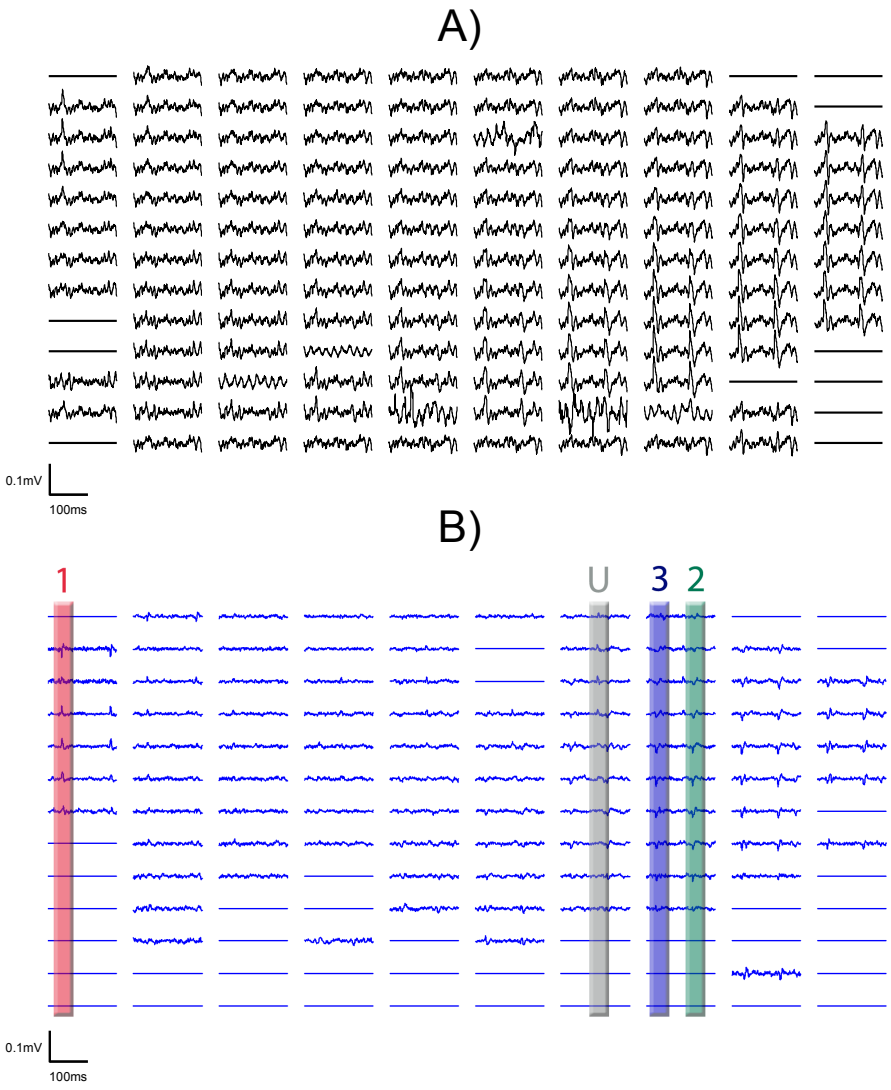

Figure 5.7: Monopolar (a) and bipolar (b) view of signal ($\sim$ 180ms; dataset 5); MUAPs (1,2 and 3) are indicated in different colors (b); very similar spikes (2 and 3) were successfully identified as separate MUAPs; unidentified small MUAPs are marked in grey, i.e. physiological noise; corrupted electrodes were switched off (zero values)

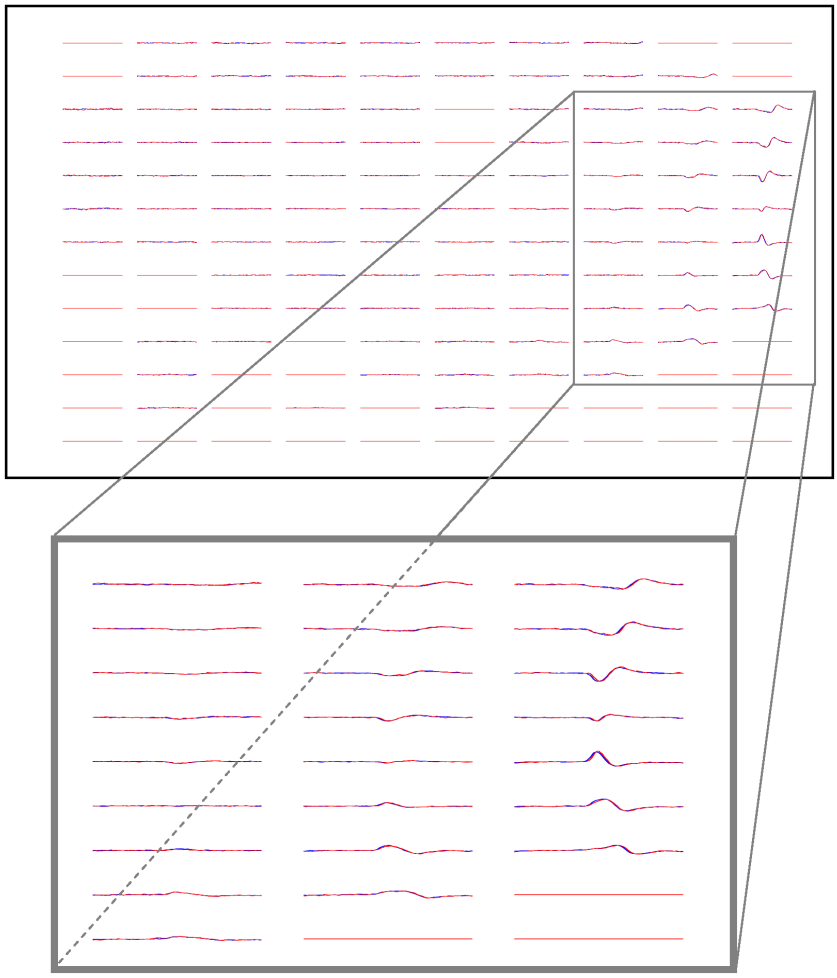

Figure 5.8: The MUAP with the lowest spatial correlation (0.83; NRMSE=0.56; MU # 9 in Table 5.2) between the actual (blue) and recovered (red) signatures. The expanded, lower figure zooms in on the part of the array that is closest to the MUs neuromuscular junction (has the largest signals). This example illustrates that even in the cases with a relatively low correlation, the reconstructed and original shapes match very well. The low correlation value is primarily due to the very small signal size in most channels in combination with the influence of noise.

5.4 Discussion

In this chapter, we presented a new approach aiming at the decomposition of the muscle activity recorded with HD-sEMG. The method is validated on both simulated and real life data. It offers a fast and automated solution for the assessment of both the MUAP signatures of active MUs and their firing patterns. The main novelties of this 3-step HD-sEMG decomposition approach are its automation and computational effectiveness: automated selection of relevant electrodes and detection of timestamps; the "smart" clustering which reliably extracts MUAP signatures; and the demixing by simple multiplication that recovers the firing patterns.

The data-driven selection of clustering electrodes does not guarantee optimality. However, results show that the rationale behind it (electrodes where MUAPs are maximal ease differentiation) picks out electrodes with discriminatory information. Additionally, selecting slightly more electrodes than the number of active MUs ensures spatial distribution information assisting the classification.

The fact that the superparamagnetic clustering algorithm reliably estimates the number of clusters in an unsupervised way, without being impaired by shapes of mixtures of MUAPs, is a strong point. Additionally, it does not assume spherical distance metric. This implies that the mean shapes of cluster components are allowed to slowly evolve in time (forming ellipsoid rather than sphere) – which could help in situations of electrode drifts and slight changes due to MUAP shape instability.

The reliable estimate of MUAP shape in the clustering step, allows then for demixing of (some) MUAP mixtures in order to derive a larger number of timestamps.

5.4.1 Simulated data

The simulated signals were designed to mimic relevant temporal and spatial aspects of the thenar muscles voluntary activity recorded with HD-sEMG. The used SNR values and signal length was similar to other recent studies ([85], [84]). The performance was more affected by the number of active MUs and their mean firing rate than by the noise level. With a mean firing rate of 10 Hz the algorithm on average recovers around 18 of 20 present signatures in the simulation study. Even in the most challenging case, assuming 20 active MUs, all firing at 20 Hz rate, 12-14 signatures could still be reliably extracted.

The grey lines around the indicated mean values in Figure 5.5 which represent the borders containing all the obtained results, confirm the stable performance of the described approach. As seen in Table 5.1, the average spatial reconstruction quality slowly decays with the increasing frequency of spikes. Small decay in

signature reconstruction (indicated by increased NRMSE) at higher firing rates can be partially explained by a smaller number of uncorrupted spikes in the clustering phase.

The identified spike timestamps are reliable, as can be seen from the precision values. Precision values are higher in the demixing step compared to clustering for firing frequency of 5 Hz, however, this ratio changes slightly in favor of clustering at 10 and 20 Hz rate. It can happen in the demixing step, that a wrong unit is peeled off when a MU signature was not identified in the clustering step and a similar shape was assigned instead. The %complete drops mainly due to the increased firing rate. It reaches the average values of ~ 35, 65 and 82% for mean firing rates of 20, 10 and 5 Hz respectively. Only more validation studies with real signals can tell how severe the drop in %complete is at higher contraction. A high firing rate affects the number of identified signatures: each missing shape implies that the mixtures containing this shape and any other MUAP cannot be resolved. When the majority of signatures is successfully recovered, like in the case of mean firing rate of 5 Hz or 10 Hz, %complete is only slowly decaying with increasing number of active MUs.

5.4.2 Real data

We also demonstrated the performance of the new method on a set of manually scored recordings from the lateral vastus leg muscle. These datasets are, despite the low contraction force, challenging because observed MUAPs have very low SNR compared to those of the thenar muscles as used in the simulations. Part of the present noise stems from physiological sources such as activity from deep MUs or distant muscles. To reduce the effect of this physiological noise, bipolar spatial filtering was applied prior to the processing.

Out of the 25 different MUAP signatures detected by the two operators in the recorded data, 24 were identified with our automated approach. Our method for selecting the clustering electrodes did not identify the appropriate electrode in the case of the missed unit, due to the dominance of two spread-out units. Possibly, having better way to choose clustering channels would enable detection of this unidentified unit. The relative number of clustering electrodes with respect to the number of existing MUPTs was higher than in simulated signals. This came as a result of a larger shift of spikes between distant channels than in case of the thenar muscles.

The results of the real signals largely confirm the findings of the simulation study. The %complete achieved by our algorithm (median value 91%) is similar to the level reported in other state of the art HD-sEMG decomposition studies [33], [84]. Since the signals corresponded to low contraction forces, and the fact that the operators decided that the firing patterns were successfully reconstructed, the %complete

values can be considered close to ones that would be obtained when comparing with the ideal, complete firing patterns. The situation where a firing was marked by the operators and not by our program, can be explained by three different reasons. First, when many (similar or small) unidentifiable MUAPs were present, the algorithm was not able to decompose the mixtures containing unrecognized shapes; second, more substantial differences in MUAP shapes induced by noise (e.g. datasets 1 and 9); and third, similar shapes can cause wrong assignments (e.g. in dataset 6). Nevertheless, the firing patterns could still be reliably enough approximated to derive the dominant mean firing frequency of the identified units. It is also worth mentioning that our algorithm identified several additional units. These had not been detected by the operators and were, therefore, excluded from evaluation.

In accordance with these results, the next step appears to be further validation of our algorithm by means of co-registration and correlation of intramuscular and surface EMG recordings as performed in [33], [84]. It can be anticipated that in clinical settings, unstable contractions and physiological noise can impede the extraction of all present signatures and hence also the quality of firing pattern reconstruction can go down. The key assumptions for our algorithm are that each MUAP has a relatively stable shape and appears a number of times to be recognized as a cluster. The former is inherently shared by most of automated methods and although the clustering method we used can deal with certain shape instability, it is yet to be explored to which extent it is resilient to such cases. The latter assumes having a number of uncorrupted shapes suggesting a limitation connected with high contractions and needs to be explored further.

To achieve decomposition in a wider range of applications, the demixing strategy could be extended. As an initial demixing algorithm, we opted for a straight-forward but reliable solution for demixing, allowing only known shapes to participate in mixtures. Despite the fact that MUAP shapes are in general reliably estimated, %complete should be further improved in cases where not all present units are detected in the clustering step. By modifying the demixing criteria to observe the residue on only a part of the grid associated with the identified MUAP shape could be an obvious step to detect more timestamps.

Another way to extract more timestamps is by resolving the cases of phase cancellation between nearly simultaneous MUAPs (e.g., similar to previous work on intramuscular EMG decomposition [122]) at a higher computational cost. The idea would be to estimate all possible mixture shapes in advance by exploring all possible combinations. A possible way to extract additional MUAP signatures, is to employ approaches using e.g. convolutive constrained ICA ([24]) where a mixture is described as a sum of known and yet unidentified sources which are then extracted.

5.5 Conclusion

The new method for the decomposition of HD-sEMG recorded signals was introduced. It presents an attractive and automated solution that is desirable for many applications, especially due to the unavailability of other methods of similar performance. The algorithm was verified on simulated and real signals. The signal decomposition is not always complete and its results decay with the increasing muscle contraction force. Exact limits of performance are yet to be determined by means of congruent recordings with needle EMG and comparison of the results. Method also shows potential for further improvement.

Chapter 6

Correcting electrode displacement errors in motor unit tracking using high density surface electromyography (HDsEMG)

Matching the same MUAPs recorded by means of HD-sEMG in different recording sessions is not an easy task. Furthermore, this was not possible unless a recording HD-sEMG grid is always re-placed exactly on the same spot. This study discusses a technique to correct for effects of electrode grid displacement across serial surface EMG measurements with HD-sEMG electrode arrays. A proof of concept study shows that automated correction is possible and that agreement is increased between the same motor unit action potentials observed across different measurements. It also shows great potential for assisting motor unit tracking studies, indicating that otherwise electrode displacements cannot always be precisely described. This chapter is based on [70].

6.1 Introduction

Neuromuscular diseases affect MUs, either directly or indirectly. The follow-up study of MUs during a disease process may, therefore, improve our understanding

of neuromuscular diseases. Recently, MU tracking using HD-sEMG has been introduced as a neurophysiological technique that enables noninvasive follow-up of single MUs [115]. In this technique MUAPs are recorded with an array of densely spaced electrodes after electrical stimulation of the afferent nerve. As stated earlier, in HD-sEMG recordings, each MUAP is presented as a spatio-temporal profile (signature or fingerprint) of the corresponding MU. Use of the characteristic information in the fingerprints facilitates detection of the MUAPs in consecutive recording sessions and, hence, allows for MU tracking.

MU tracking may provide insight into the relationship between MUAP properties and how these are affected during disease progression. However, before changes in a MUAP between sessions can be ascribed to an underlying pathophysiological process, other factors that affect the MUAP fingerprint have to be taken into account. It is known that MUAP properties depend on geometrical and anatomical factors such as muscle fiber length, signal stability (electrode-skin contact), electrode location, and electrode orientation [124]. In particular, even small shifts in electrode position can affect the MUAP parameters significantly.

In clinical practice, the recording grid can be rotated, translated and bended in a different way compared to how it was attached in the previous recording session. In [83], a method was proposed to correct for translational errors for the study of the external sphincter muscle. In this study we extend this correction procedure and show how the effects of rotation between sessions can also be automatically compensated for. We illustrate the approach on a low-force voluntary contraction measurement of thenar muscles, following well-defined displacements.

6.2 Methods

6.2.1 Recordings

Test recordings of voluntary contractions were performed on three healthy subjects using a HD-sEMG grid with 126 electrodes spaced equidistantly in 9 rows and 14 columns, as described in detail elsewhere [115]. The grid was placed over the thenar muscles. Initially, four configurations were introduced to illustrate the concept using recordings from a single subject, indicated in Figure 6.1 (a). Additionally, recording grid in configuration 1 was used as a reference configuration for 5 additional 2-minute recordings in each of 3 subjects: with the grid positioned in reference configuration, and positions rotated for -5, +5, -10 and +10 degrees around it, mimicking accidental grid displacement. The approximate reference position (configuration 1) is identified as the orthogonal to the direction connecting carpometacarpal (CMC) and metacarpophalangeal (MCP) joints of the thumb. This guaranteed the total thenar muscle coverage.

Figure 6.1: (a) Four test recording configurations; arrows indicate the direction from the side of PCB connector towards the horizontal end of the electrode grid; (b) recording grid in configuration 1. Red dot indicates the point used as a reference for rotation.

Placement of the electrode grid

In the experimental setup, it was important to ensure that the position of the electrode grid was precise, especially in cases of small (intentional) displacements. For this purpose, a double-sided adhesive tape (Figure 6.2 a) was used like in [104]. This double sided tape contained small and large gaps. The large gaps were placed 4mm apart from each other and matched the positions of the electrodes to be placed. The small gaps were in between and also 4mm apart, with the purpose of marking the exact grid location. The procedure for placing the adhesive tape and the recording grid is as follows: first, the tape is placed on top of the skin, followed by marking the position through the small holes using a pen/marker; then, a conductive gel is inserted in the large holes for a better contact with the skin. Second part of the tape is removed and the electrode is attached to the tape. Thanks to perfusions of the same size in the tape and the recording grid, the placement is precise. After the measurement, traces of marked positions are preserved (Figure 6.2 b) and this dot pattern serves as a reference for calculating the new positions of small gaps (small displacement) using simple trigonometry relations. Once this is done, these positions are manually marked on the skin and

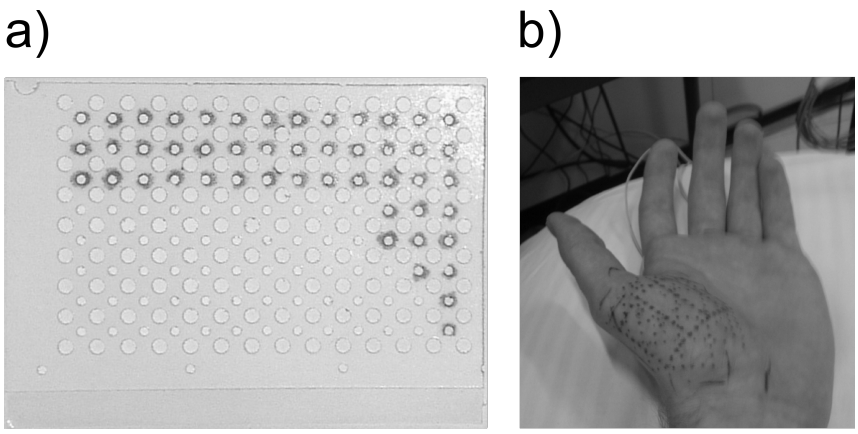

Figure 6.2: (a) Adhesive double-sided tape used for the recording. Large holes correspond with the electrode positions while the small ones are used to mark the position of the grid. (b) After measurement, traces of pen on the skin remain and assist the correct replacement of the electrode mimicking accidental displacement.

the new tape is placed to match them as to repeat the measurement procedure.

The point of rotation is the top left corner of the recording grid, as indicated with red dot in Figure 6.1 b.

Measurements and extraction of MUAPs

Recordings were performed on a single day for each subject, with half-hour break intervals. Visual feedback in the form of bipolarly filtered signals (Figure 6.3) was used to assist the subject in establishing and maintaining a stable, low-force contraction level. An experienced observer gave feedback if the interference pattern was too complex based on the ability to observe clear trains of spikes from individual MUs.

All signals were first decomposed automatically, separating each into contributions from individual MUs using the algorithm described in [68]. This yielded sets of MUAP fingerprints for each session.

Fingerprints that were observed at least 100 times during the two-minute recording were considered reliable, averaged and kept for further analysis. This high number of observations ensured the effective noise cancellation after averaging.

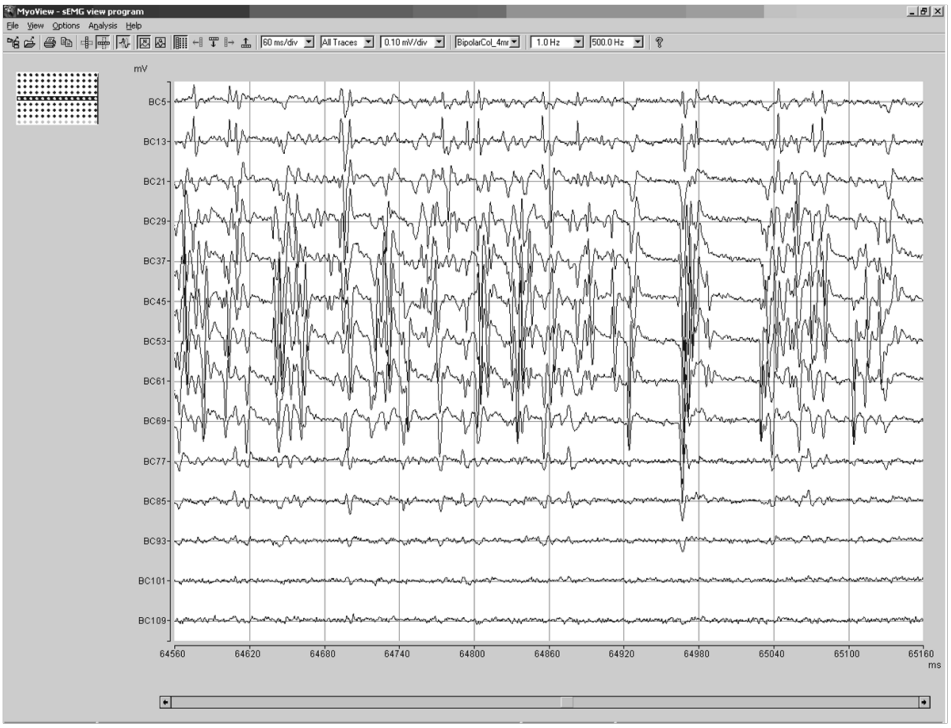

Figure 6.3: Example of visual feedback assisting the subjects with maintaining the low-force contraction level.

6.2.2 Artificial recording grid displacement

To assess the effect of rotation of a grid around its center, we first assign coordinates (x, y) to the electrode locations in the original grid placement. After rotation over angle θ, new coordinates (x', y'), representing the position of these electrodes are then obtained by multiplication with a rotation matrix:

$$\begin{bmatrix} x' \\ y' \end{bmatrix} = \begin{bmatrix} cos(\theta) & -sin(\theta) \\ sin(\theta) & cos(\theta) \end{bmatrix} \begin{bmatrix} x \\ y \end{bmatrix} \tag{6.1}$$

To assess the value of a fingerprint in every set of rotated coordinates (x', y'), we use the linear interpolation based on originally recorded values. This was done for each temporal sample to obtain a projection of a fingerprint on a rotated grid. The rotation procedure is depicted in Figure 6.4 (a). The interpolation is reliable

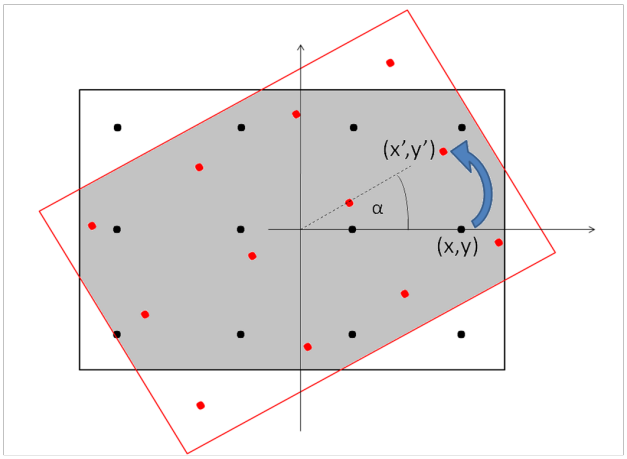

a)

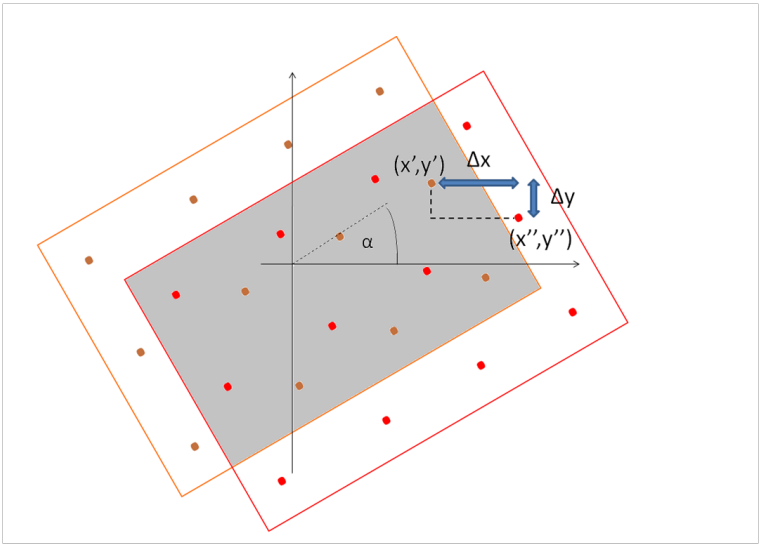

b)

Figure 6.4: (a) Calculating the positions of electrodes of a rotated grid; (b) additional translation for finding the position of the best matching

only in the intersection area (gray), while the rest of the values cannot be reliably assessed and were put to zero.

Apart from rotation, the in-plane translation of the recording grid is practically

inevitable and thus has to be taken into account [83]. Comparing translated observations can be done only in the intersection area (gray in Figure 6.4 (b)). Since we can compare only part of each fingerprint, it is necessary to choose a "subgrid" – 6x6 subset of electrodes around the place of the highest spike which is subsequently used for comparison. The subgrid "subfingerprint" is compared with each possible counterpart of the investigated fingerprint with which we attempt to match. The best possible position reveals the translation. This example is shown in Figure 6.4 (b). In order to have a better than inter-electrode distance resolution we first need to upsample the signal. For this purpose, we apply bicubic interpolation [103].

Each fingerprint is upsampled and rotated for a chosen angle, followed by the estimation of optimal translation for the comparison with its "non-rotated" counterpart. We proceed with downsampling the signal to its original dimensions, and then compare rotated and "fixed" fingerprints using 2 parameters: correlation and normalized mean squared error (NRMSE) like in [68]. The peak of the ratio between these values (ρ, high correlation and small residue when we subtract fingerprints) indicates units that match. Each MUAP fingerprint obtained by a "displaced" grid is compared with its best match from the "fixed" grid measurement.

The complete procedure relies on the algorithm 6.2.2 which is called upon twice, with slightly different inputs. Two sets of MUAPs (MUAPs_1 and MUAPs_2) are extracted in different measurements for which accidental displacement of the recording grid is assumed. $MUAPs_1$ are being altered by rotation/translation, while $MUAPs_2$ are fixed. Additional inputs for the algorithm are the maximal assumed displacement angle α and the rotation angle step $\Delta\alpha$. In the first go, the angle and angle steps are: $\alpha = 30°$ and $\Delta\alpha = 2.5°$. This means that the rotation angle is varied between $-30°$ and $30°$, in steps of $2.5°$, calculating the optimal translation for each angle. This is achieved through comparison of upsampled subgrids identified in the rotated MUAPs (rtMUAPs_1) around its peak spike, with all possible (upsampled) subgrids in MUAPs_2. Optimal rotation angle is identified by the peak value of ρ. This identifies the rough angle (α_1) after which the algorithm is called again, this time for the indicated rotation angle value α_1 and the fine angle step $\Delta\alpha = 0.5°$, to achieve the fine tuning. Finally, the output provides the angle of rotation and the displacement in x and y directions.

6.3 Results

For the study with 4 configurations (Figure 6.1 (a)) in total, 25 reliable MU fingerprints were extracted with the decomposition method. Out of these, 3 units could be tracked across measurements: 1 unit appeared in 3 configurations (1, 2 and 4), and the remaining two were matched across configurations 1 and 2. An

Algorithm 1 Identifying the displacement of the recording grid

Input: MUAPs_1, MUAPs_2, α, $\Delta\alpha$
Output: rtMUAPs_1, α_1, Δx_1, Δy_1, ρ

Initialization: $\alpha_i = -\alpha,\ \alpha_1 = -\alpha,\ \Delta x_1 = 0,\ \Delta y_1 = 0,\ \rho = 0$
loop ▷ Until maximal ρ is found
    Upsample MUAPs_1 and MUAPs_2.
    Obtain rtMUAPs_1 as rotation of MUAPs_1 for angle α_i.
    Extract subgrids.
    Match all sub-grids and find maximum ratio ρ_{it}.
    Downsample rtMUAPs_1 and MUAPs_2.
    if $\rho_{\text{it}} > \rho$ **then**
        $\rho \leftarrow \rho_{\text{it}}$
        $\alpha_1 \leftarrow \alpha_i$
        Modify Δx_1, Δy_1
    end if
    if $\alpha_i = \alpha$ **then**
        Stop the algorithm.
    else
        $\alpha_i \leftarrow \alpha_i + \Delta\alpha$
    end if
end loop

example for the automatic correction of the specified 45 degrees displacement is portrayed in Figure 6.5, showing the correlation and the ratio between correlation and NRMSE. The angle was estimated at 42 degrees, translation at -2 and 3 mm displacement in x and y directions respectively. Figure 6.5 (a) and (b) indicate the originally recorded fingerprints from positions 2 and 1 respectively. Once the rotational and translational corrections have been applied, these 2 fingerprints proved to match almost perfectly (Figure 6.6 (c)). The subgrid used for comparison is also indicated. Overlaid observation can finally be seen in Figure 6.6 (d).

The second part of the study involved 3 subjects and aimed at MU tracking with simulated accidental displacements of the recording grid for configuration 1 (Figure 6.1 (a)). On average, 5 fingerprints per subject could be tracked across one or more measurement configurations.

The number of units that were found and tracked per subject together with their average correlation before and after electrode placement corrections, are summarized in Table 6.1. It was found that the indicated grid displacements did not always match the ones extracted by our procedure. The largest observed

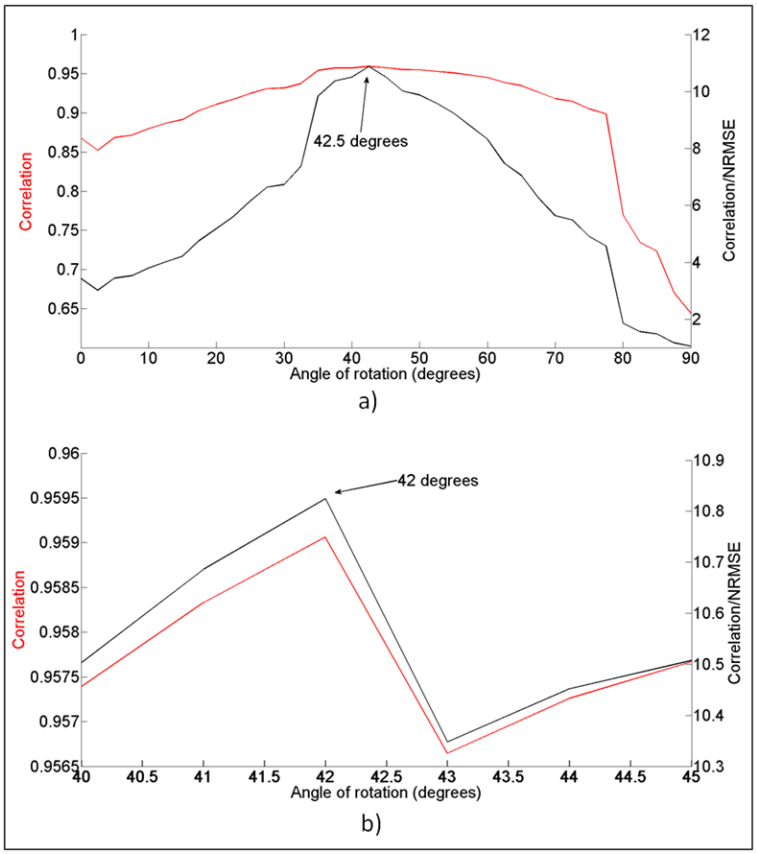

Figure 6.5: Example for the automatic correction of the indicated 45° displacement. Correlations (red) and the ratio correlation/NRMSE (black) between the original and fingerprint obtained by adjusting the displaced electrode grid (a) roughly identified angle of rotation (42.5°) as a peak of the ratio correlation/NRMSE and (b) pinpointed precise value of 42°

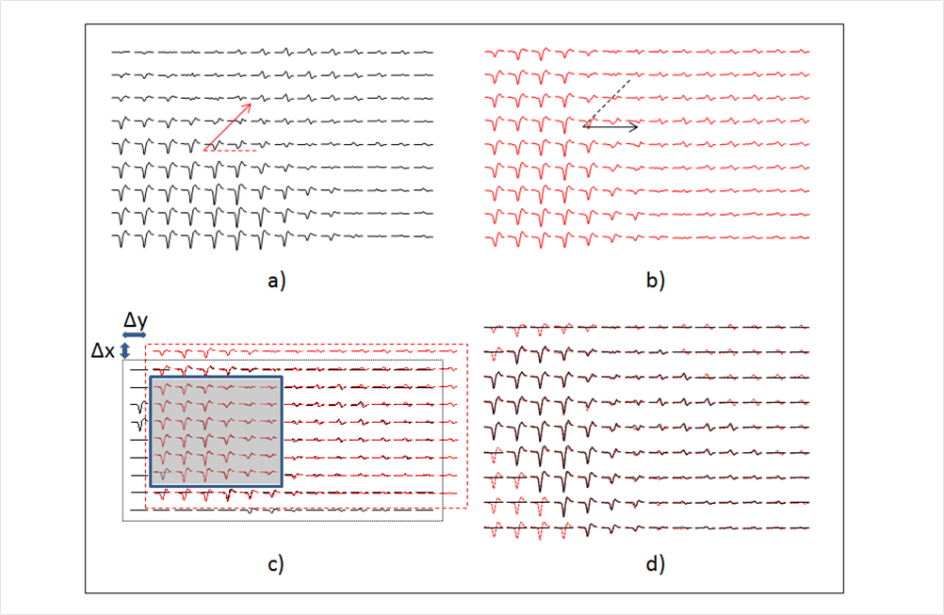

Figure 6.6: Matching the units from displaced grid recordings; (a) MUAP fingerprint obtained using grid rotated over 42° with respect to signature from (b); (c) matching corrected projection of (a) using the operators described in the text; subgrid used to pinpoint the translation displacement is depicted in gray; (d) overlaid signatures (b) - red and (c) - black

difference was the one for measurement involving subject 1. While the indicated angle was 5 degrees, the calculated (and in fact, correct) one was -2 degrees with respect to the position 1 ("error" of 7 degrees). This may be the result of relative muscle-skin displacement (due to e.g. thumb movement) rather than angle measurement error. On average, estimated displacement was within ±3 degrees from the indicated value.

Angular precision could be tested on subject 2, where the same 2 fingerprints were found in two electrode displacement configurations. Searching for the joint peak of agreement revealed the angular ambiguity of 1.6 degrees.

Two examples showing the overlaid original (blue) and matched fingerprint (red) after correction of displacements are portrayed in Figure 6.7 and Figure 6.8. Another example how the described procedure can be used even in cases where no matching units are found is shown in Figure 6.9. Even though the fingerprints with the highest degree of similarity are apparently not originating from the same MU, the

Table 6.1: Comparison of the fingerprints from measurements with displaced electrode grid, before and after applying the in-plane projection adjustment

	Fingerprints		Average correlation	
Subject	Extracted	Trackable	Before correction %	After correction %
1	51	8	86.3	92.4
2	39	6	84.0	93.4
3	30	3	82.2	90.0

suggested correction procedure guessed the electrode grid displacement right, as a consequence of similarity of MU's spatio-temporal profiles.

6.4 Discussion

Even when electrode re-placement between sessions is done with great care, repositioning errors may remain. Mitigating the effect of such errors may be expected to improve the reliability of ascribing changes in the MUAP to true (patho) physiological changes. Extrapolating the results of our pilot study with known displacements indicates how this may be achieved when the replacement error is not known.

Thus far, MU tracking using HD-sEMG has been performed without corrections for recording grid displacement [115] or accounting for translational displacements only [83]. This implied that correlations between identical but displaced MUAPs could be relatively low; indeed, the threshold for considering MUAPs to be similar was set to a cross-correlation value of 80% ([115], [83]). Being able to automatically adjust for re-placement errors might allow for a higher threshold, increasing the specificity. It may also simplify greatly the otherwise strict and time consuming procedure for placing the HD-sEMG recording grid.

After adjusting the projection using rotation and translation operators, significant improvement in agreement was observable both visually and numerically via the correlation and NRMSE coefficients. Moreover, it was found that this method allows fine-tuning in the order of two degrees in angular direction in rotation and 1mm (a quarter of the inter-electrode distance for the used electrode grid) accuracy in translation. One should note that these measures are likely to be muscle specific and do not necessarily hold for other muscle types. The correction procedure

maximizes correlations between units in different sessions. Hard thresholding on these correlation parameters did not enable fully automatic matching in a sense that the visual confirmation on indicated "similar" units was still necessary. Further insight into methods for rotation and translation invariant pattern classification might provide more reliable measures for this purpose (e.g. [35]). To define the necessary agreement between fingerprints in order to consider them as originating from the same MU, the minimal disagreement between different MUAPs has to be described. Also, it is important to investigate and describe the changes that could be ascribed to the remaining modeling imperfections such as bending of the electrode grid, and changes in skin-electrode contact. This would enable to differentiate between the physiological changes of the muscle and the method limitations when comparing healthy units. This rule would help to maximize the applicability of MU tracking studies. The other remaining issues concern muscle specific properties.

6.5 Conclusion

We presented the method to track MUs across measurements more reliably when a recording grid is potentially not perfectly repositioned. The initial results show that the method reliably aligns MUs across sessions. This will allow to perform MU tracking with higher precision than currently possible.

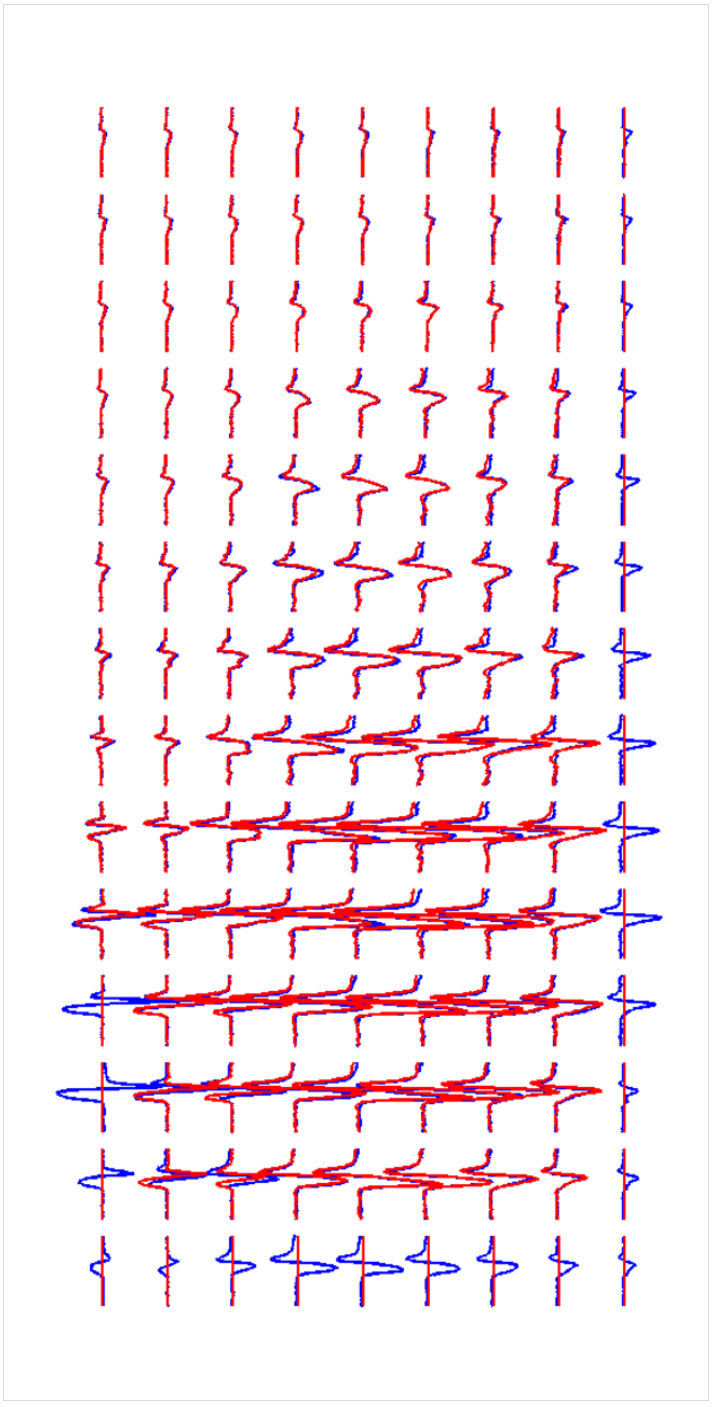

Figure 6.7: An example of matched fingerprints recorded in different sessions involving electrode grid displacement; the overlaid original (blue) and matched fingerprint (red) confirm they belong to the same MU; indicated and estimated measurement angular displacement was $-10°$ and $-11°$ degrees respectively

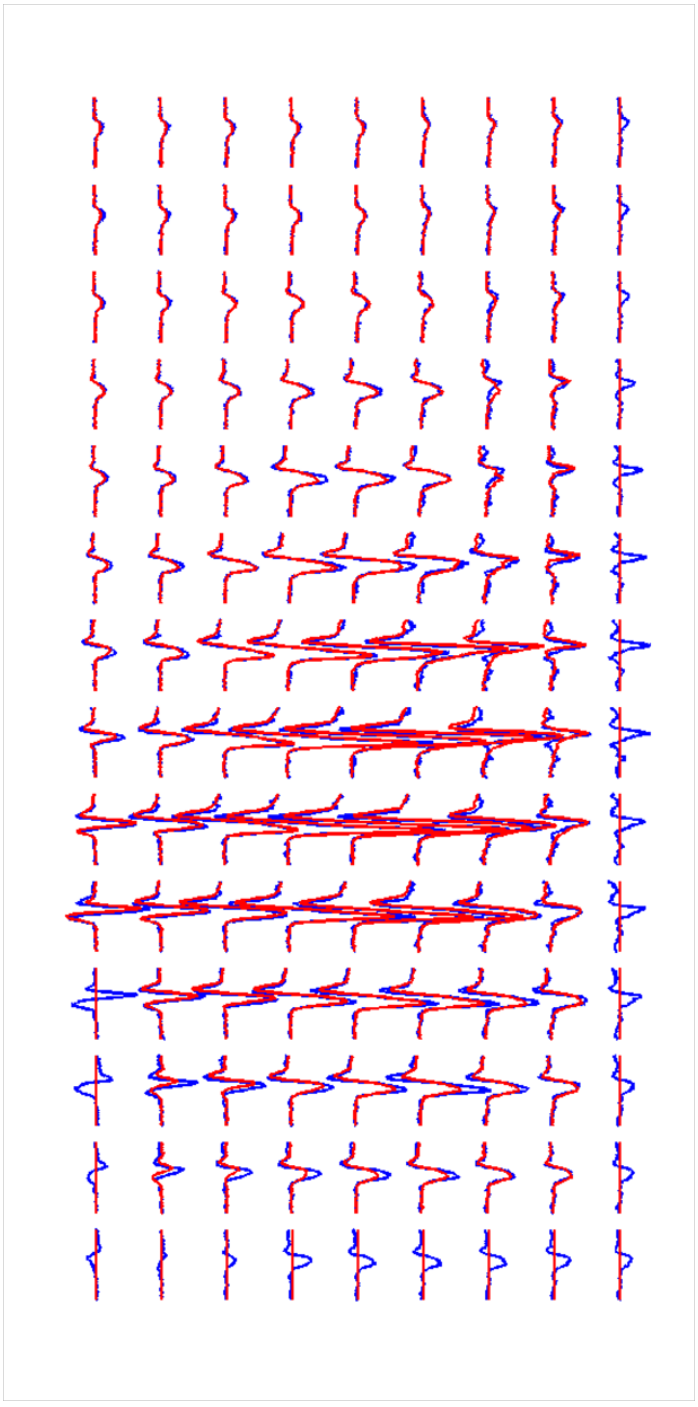

Figure 6.8: An example of matched fingerprints recorded in different sessions involving electrode grid displacement; the overlaid original (blue) and matched fingerprint (red) confirm they belong to the same MU; indicated and estimated measurement angular displacement was -5° and -7° degrees respectively

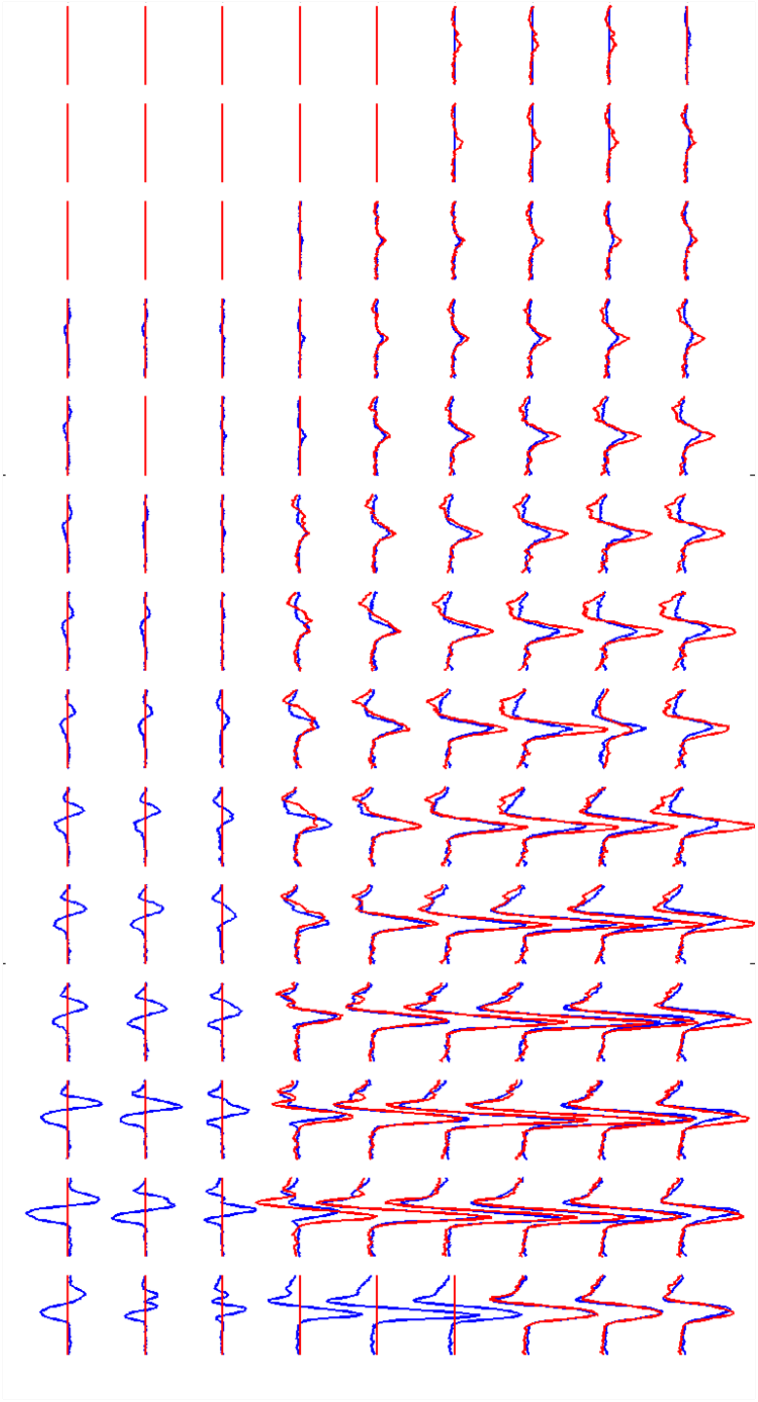

Figure 6.9: Displacement correction procedure for two fingerprints originating from different MU's (blue - original, red - corrected) estimated the rotation angle right to 15° degrees as indicated from the operator performing the measurement; This was possible due to similar fingerprint "spread" profiles related to the thenar muscles.

Chapter 7

Conclusion and Future Work

The classification of neuronal spikes and motor unit action potentials (MUAPs) are different problems which were tackled in this thesis. The connection point was the obvious similarity in signal processing needed to extract relevant information: detection and classification of spike shapes as well as the post processing of detected timestamps. This chapter provides an overview of the work presented concerning these two topics. Additionally, it states some open questions, and proposes approaches towards solutions of these problems, including some ongoing activity.

7.1 Analysis of neuronal signals using multichannel neuroprobes

7.1.1 Automated analysis of neural spike trains

The classification of neural spikes is an old but still not fully solved issue. Modern neuroprobes with many contacts call for using automated signal processing, that assumes accurate classification and detection of trends in neural activity. Spikes need to be detected and classified according to the putative neuron. This enables the study of how brain networks function and the testing of various research paradigms related to changes in neural activity. Available solutions are not perfect and the errors induced by inaccurate classification that cannot be avoided are often overlooked in terms of how they affect the outcome interpretation. This inaccurate classification is especially pronounced when the SNR of spikes is low, which is frequently the case in real life recordings. A theoretical limit of SNR preventing the

successful classification has been drawn before ([162]), however, without practical, real life considerations.

In Chapter 2, we demonstrated how the usually unchecked results obtained after the spike train classification can offer deceiving information about spike rate function even when using up-to-date clustering algorithms. A set of realistic, low quality signals has been investigated to determine the practical lower limit of SNR for classification using the existing Wave_clus algorithm ([149]). Although one can always argue how different spike shapes affect the outcome, it was found that SNR ratios of at least 1.5 are needed for obtaining reliable estimates of a spike firing pattern with the traditional classification approaches.

The second part of the same study started from the assumption of an arbitrary classification algorithm, and treated the problem of clustering errors more generally. Instead of excluding the clusters of low SNR or blindly accepting the results of classification, a different approach was proposed. It employs a set of parameters that are used for the description of spike rate/ISI function. These parameters describe its main properties of interest and detect the changing activity of neurons. First, a set of major features of a firing neuron has been determined and parameters were introduced to detect and describe them. This set of parameters included previously used as well as newly proposed ones. Furthermore, one of the key points of this investigation was to test the reliability of these parameters. Train signals were used which contained a degree of misclassification errors. These parameters were then tested for robustness in presence of these errors, information carrying potential and the ability to detect overclustering. New parameters describing fast neural activity were found as a suitable, more robust replacement for traditional burst detection which could be strongly biased by missed detections and spike misclassification. Traditional mean firing frequency was found to be unreliable even with modest classification errors. A median function was found to be a better, robust descriptor. Coefficient of variation (along with other, less prominent parameters) was found to be descriptive and reliable for adding information about the spike firing pattern. Finally, the frequently appearing problem of overclustering was also addressed using the parameters (namely skewness and kurtosis). Despite their apparent low confidence, these were able to reliably pinpoint cases of overclustering showing a potential for the use as a criteria for automated cluster merging. The whole study was done with varying SNR, where at each level a point of achieved trust was established. Describing ISI function with parameters presents a framework that could be further extended for future automated neural signals processing.

Chapter 3 describes a study aimed at finding new possible targets for DBS for treatment of OCD. Here, we encountered the case or spike clusters which (on average) had a low SNR. Extracted spike clusters had to be first visually inspected to exclude the cases of obvious, very large misclassifications or noise induced spikes. After visual selection, some of the parameters introduced in Chapter 2, were used in

the automated processing step. The mean neuron firing rate (which is traditionally considered), was not found to exhibit detectably different values in control and test groups. This is probably due to the low SNR of spike clusters (as indicated in Chapter 2). Therefore, other parameters were used as well, showing statistically significant different behavior in the BST area of polydiptic rats compared to the resistant group. This justified the concept of using the proposed parameters. Furthermore, the results of this study motivate future investigation of BST as a meaningful DBS target.

7.1.2 Future work on neural spike train processing

The reliability of parameters describing ISI function can be further improved similarly to [142] and [141] used in EMG studies where an ISI histogram is first cut, leaving out distant timestamps which are corrupting these describing parameters even if they come as a result of an accurate classification. This is expected to enhance the parameter robustness, since they are in a way modeling the ISI histogram.

The whole logic of using the parameters for description of ISI function defines a way for automated processing of signals recorded by modern multichannel neuroprobes, which is a necessity due to the large amount of data. There are two ways to do this: 1) by setting a hard threshold on parameter reliability with respect to spike cluster SNR, keeping the signals above it and discarding the others; and 2) by further extending the limits of acceptable clusters depending on similarity with the other extracted clusters. These extensions are expected to enable long-term *in vivo* spike train analysis, e.g. in cases of chronic probe implantation.

To investigate changes in neural activity as a function of applied stimuli (condition, paradigm) it is important to have an online tool for analysis and visualization of this activity. A first step towards the goal of online tracking of neural activity has been taken in a master thesis we supervised ([73]), that demonstrated the online classification, parameter extraction and visual tracking for the purpose of observing the immediate effects of DBS. An example of this online graphical user interface (GUI) is shown in Figure 7.1. This example shows the simulation of detected changes induced by DBS. First, spikes from spontaneously firing neurons are detected and classified in the training stage prior to electrical stimulation; baseline values of ISI parameters (here just mean firing rate and bursting) are extracted; after the stimulation starts, it is possible to track online significant changes in parameter values as a result of the stimuli.

Extending this proof of concept to a user-ready tool needs several additional extensions, namely automated selection of channels with acceptable noise level, and further denoising using blind source separation (BSS) techniques. Some of the

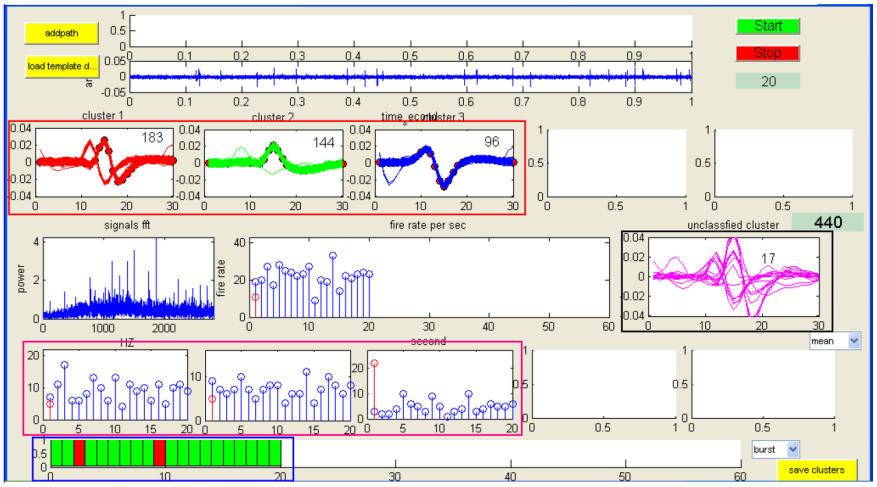

Figure 7.1: GUI for tracking the online changes in neural activity. After an initialization that identifies the existing spike clusters and baseline values describing these spike firing patterns, electrical stimulation is applied. The picture represents a screenshot after 20s of applied stimulation visualizing the changing neural activity. The drawing encircled with the red rectangle shows three types of spikes classified, 183 of type 1, 144 of type 2 and 96 spikes of type 3. In the black rectangle, the 17 unclassified spikes are also displayed. The pink rectangle shows the average firing rates of each type of spikes for every second (blue circles); the mean firing rate before applying the stimulation is displayed in read circles for comparison. At the bottom of the blue rectangle, the color indicators show the bursting information per second, where the green color indicates no activity and the red color indicates bursting. These parameters are estimated on the fly giving the visual feedback to the researcher.

recent approaches using Empirical Mode Decomposition (EMD) in combination with Independent Component Analysis (ICA) were examined during the course of this doctoral dissertation and reported in [125] and [126]. EMD decomposes the signal in spectrally non-overlapping components. The ICA then groups the statistically correlated components. This allows to leave out the noise related parts of the signal in the subsequent reconstruction. Current versions of the EMD algorithm are rather slow. However, speeding up this process (e.g. using the proposed synchro-squeezed wavelets reported in [31]) might make it a good candidate for such an effort. Fully automated processing of neural signals can support a number of behavioral studies, e.g. with freely moving animals and allow combining this type of signals with other modalities such as video data.

The newest generation of invasive neuroprobes allows multichannel measurements and stimulation with an enormous potential for fighting against diseases such as Parkinson, epilepsy, obsessive compulsive disorders, depression, psychoses. One of the main challenges is to process and interpret a large amount of the recorded data. The aim is to achieve this by building up a software platform for advanced, automated, and robust spike sorting and LFP processing being a main driver for improving health technology for brain diseases. Such platform would enable coupling of the LFP and spike train analysis as complementary modalities for better understanding of the correlations between recorded signals and different brain states. Moreover, new and flexible approaches are needed for real-time visualization of multi-channel, noisy, and highly correlated data taking into account the spatial layout of the probe and the underlying research application. Researchers need a tool that extracts the most relevant features and displays them in an intuitive manner enabling instantaneous interpretation needed for adjustments and later thorough analysis. Real-time neurofeedback during experiments and during specific behavioral tasks would dramatically improve current experimental practice by allowing researchers to adjust experimental conditions on the fly.

The ultimate goal is to implement neurofeedback into closed-loop systems for the targeted modulation/treatment of normal and abnormal neural dynamics using appropriate stimuli. Creating such a platform able to work in a closed-loop system can lead to novel, more efficient strategies for DBRS: more adapted to patient needs, more meaningful and "on demand" instead of using constant electrical stimulation.

7.2 Utilizing HD-sEMG for the analysis of muscle signals

7.2.1 Analysis of signals recorded using HD-sEMG

HD-sEMG as a new, non-invasive technique for the analysis of muscle activity is gaining popularity as a research and possible medical tool as described in Chapter 4. The decomposition of muscle signals into contributions of individual MUs is an important task in muscle signal analysis, which is still not a fully resolved problem. As shown, a big part of the possible applications of HD-sEMG assumes the decomposition of muscle signals as a starting point.

In Chapter 5 we proposed a solution to the decomposition problem. The introduced algorithm is shown to be able to decompose signals with contributions of up to 20 active MUs. The solution is able to deal with all kinds of recording HD-sEMG grids and with arbitrary spatial filtering applied in the pre-processing step. It is able to process the data in an automated and semi-automated (assisted) way in

search for optimal performance.

Motor unit tracking is a way to track the shapes of MUAPs and their firing patterns and relate them to a disease (or age) induced changes. If achieved, a reliable MU tracking would represent a valuable research and medical tool for the follow-up studies of such conditions. In Chapter 6 we build upon the previously reported idea about MU tracking using HD-sEMG. Previous efforts involved time consuming precise relocation of the recording grid. This HD-sEMG grid had to be placed very carefully at exactly the same area atop of the muscle to be theoretically able to track MUs in successive measurements. This problem has been tackled successfully, enabling automated corrections of the grid position using mathematical rotational and translational transforms with minor loss of information. The presented study proved this concept using three healthy subjects' voluntary contraction recordings. Coupled with the automated decomposition these, also automated transforms, can reduce the needed man-hours considerably and open the possibility of future clinical applications for follow-up studies of a variety of neuromuscular disorders.

7.2.2 Future work on HD-sEMG

Our decomposition solution can potentially be improved in several ways. Various spatial filtering techniques, which change the original signals, can enhance differences between MUAPs. This presents a first and obvious choice towards performance improvement. Secondly, achieving a decomposition using a two-step approach presents an idea possibly allowing treatment of higher muscle contraction signals. Here the "traditional", first step would partially decompose the signal, revealing some of the active MUs. The contributions (MUAPs) from the identified MUs would then be subtracted from the original signal. The residue signal would then be used as an input to the second stage. This time, identification of undetected MUAPs would be achieved using BSS techniques with constraints using the identified shapes as possible mixture constituents.

Ongoing work with HD-sEMG deals with a problem of corrupted channels. The experience shows that very often a number of electrodes has a high impedance or records signals that cannot be of use (e.g. bad adhesion to the surface rendering them useless). These channels have to be switched-off because they would otherwise undermine automated analysis (like decomposition and others). It has been shown that the information recorded by HD-sEMG grids is highly redundant (but not exactly to which extent). This allows for various matrix completion algorithms (e.g. [21], [22], [20], [164]) to be applied to the recovery of MUAPs that would be recorded on electrodes if they were functioning well. There are several motives for this, for instance, in MU tracking studies: different sets of electrodes might be corrupted in successive measurements making it hard to compare MUs. One

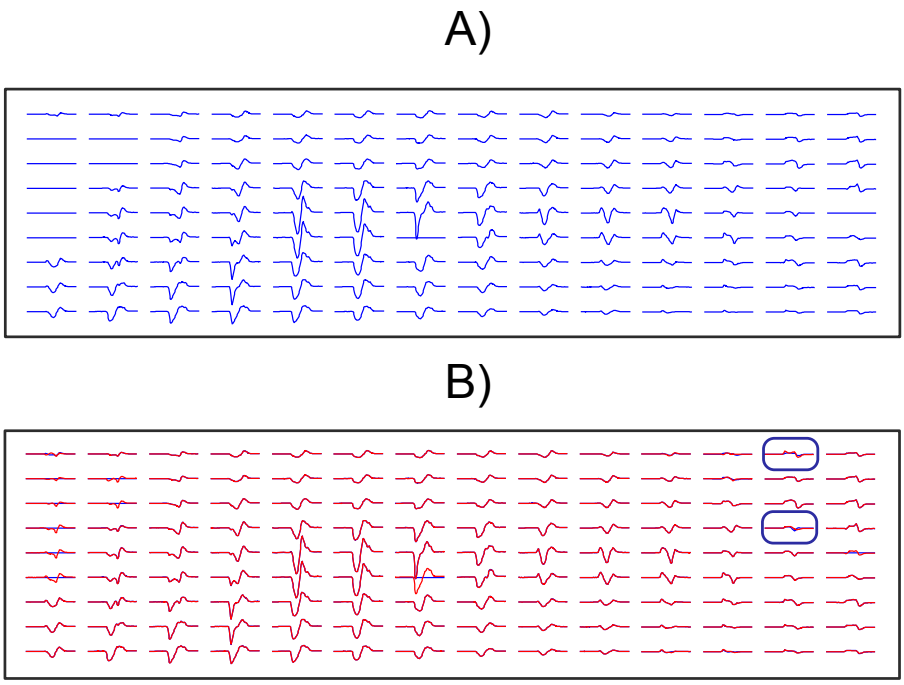

Figure 7.2: Extrapolating missing MUAPs using sparse matrix completion with MCA algorithm; a) original signature missing 9 channels; b) overlaid original and completed signature; due to the usage of the method, 2 good channels (blue squares) are mildly distorted.

example of matrix completion using the Morphological Component Analysis (MCA) [164] is shown in Figure 7.2. MCA first presents the data in some sparse dictionary before attempting the completion. Figure 7.2 a) shows the recorded signatures where 9 channels were corrupted and switched off. Figure 7.2 b) shows the overlaid original signature (blue) and the complete signature using matrix completion with MCA (red). Searching for optimal sparse dictionaries as well as limits to the precision of this MUAP reconstruction is part of ongoing research.

Extension of this approach for the purpose of automated detection of corrupted electrodes is also possible. Here, on a number of automatically detected MUAP peaks as described in Chapter 5, each electrode would be switched off in a number of Monte-Carlo simulations, attempting its content reconstruction using sparse matrix completion. Statistics of differences between reconstructed and original data is expected to reveal corrupted channels as the ones exhibiting large differences between the two.

The mentioned redundancy of HD-sEMG data raises the question of dimensionality of information. Naturally, it also calls for considering various HD-sEMG grids depending on the muscle and the dimensionality of its signals. For instance, "longitudinal" fibers like in biceps brachii muscles have "simpler" MUAPs than in the case of thenar muscles. There have been several attempts to assess the optimal inter-electrode distance (e.g. [105]). However, no convincing study has been presented so far. Proper way would be to start from reliable simulation signals allowing to assess MUAP potential at any point of the skin surface. This would create a "super-high" density potential surface that could be considered as a complete information. Then, a number of electrodes covering this surface would be varied in both directions of the recording HD-sEMG grid and the values on the predetermined potential surface would be interpolated. Comparing the original and the reconstructed surface would provide a view on quality of reconstruction. Putting a limit to this value would provide the necessary grid dimensions. This limit or threshold is highly connected with the similarity of MUAPs that can be expected with a particular muscle, because the reconstructed MUAP has to be sufficiently different from other MUs action potentials. An example of this reconstruction is provided in Figure 7.3 with a simulated MUAP signature of a small hand muscle. Figure 7.3 a) shows the original signature (blue) recorded using a 11×13 grid, with its overlaid approximation (black) with a simulated 5×8 grid. Figure 7.3 b), following the same reasoning shows the original signature with overlaid approximation using 8×5 grid. Clearly one direction carries more information needed for precise reconstruction which can be addressed when constructing electrode grids for such a muscle.

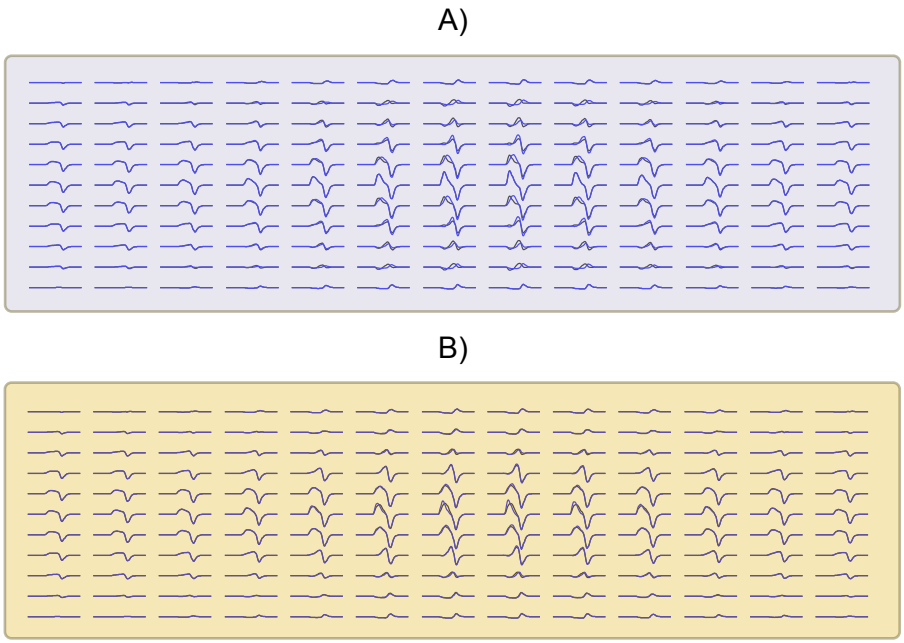

Figure 7.3: Original signature (blue) overlaid with its approximation (black). a) shows the approximation when using 5×8 recording grid; b) when perpendicular electrode direction is favored by using 8×5 recording grid, a better approximation is achieved.

Finally, a GUI that would incorporate decomposition, correction of grid displacements but also other relevant parameters of muscle signals would be a desirable tool. A similar idea about reliability of neural spike classification can also be easily implemented with MUAP clusters. This set of parameters would be smaller considering the known muscle physiology. This would represent a complete research tool for surface electromyography utilizing HD-sEMG.

Despite its popularity in the recent past, HD-sEMG is still considered as a research rather than a readily-used medical tool. This comes as a consequence of still not fully reliable employed signal processing techniques and sometimes even disputed theoretical abilities of the HD-sEMG. For one, finding ways of achieving reliable decomposition and commonly accepted procedures of testing its performance in real life settings would be a major milestone possibly bringing HD-sEMG closer to wider acceptance. If decomposition and other challenges are overcame, HD-sEMG could become an important non-invasive tool for medical applications.

Bibliography

[1] K. Abed-Meraim, W. Qiu, and Y. Hua. Blind system identification. *Proceedings of the IEEE*, 85(8):1310–1322, 1997.

[2] M. Abramowitz and I. Stegun. *Handbook of mathematical functions: with formulas, graphs, and mathematical tables*, volume 55. Dover publications, 1965.

[3] G. Alheid, J. De Olmos, and C. Beltramino. Amygdala and extended amygdala. *The rat nervous system*, 1:495–578, 1995.

[4] R. Baddeley, L. Abbott, M. Booth, F. Sengpiel, T. Freeman, E. Wakeman, and E. Rolls. Responses of neurons in primary and inferior temporal visual cortices to natural scenes. *Proceedings of the Royal Society of London. Series B: Biological Sciences*, 264(1389):1775–1783, 1997.

[5] W. Bair, C. Koch, W. Newsome, and K. Britten. Power spectrum analysis of bursting cells in area mt in the behaving monkey. *The Journal of neuroscience*, 14(5):2870–2892, 1994.

[6] K. Balanda and H. MacGillivray. Kurtosis and spread. *Canadian Journal of Statistics*, 18(1):17–30, 1990.

[7] I. Bankman, K. Johnson, and W. Schneider. Optimal detection, classification, and superposition resolution in neural waveform recordings. *Biomedical Engineering, IEEE Transactions on*, 40(8):836–841, 1993.

[8] A. Baraldi and E. Alpaydin. Constructive feedforward art clustering networks. i. *Neural Networks, IEEE Transactions on*, 13(3):645–661, 2002.

[9] A. Baraldi and E. Alpaydin. Constructive feedforward art clustering networks. ii. *Neural Networks, IEEE Transactions on*, 13(3):662–677, 2002.

[10] M. Blatt, S. Wiseman, and E. Domany. Superparamagnetic clustering of data. *Physical review letters*, 76(18):3251–3254, 1996.

[11] J. Blok, D. Stegeman, and A. Van Oosterom. Three-layer volume conductor model and software package for applications in surface electromyography. *Annals of biomedical engineering*, 30(4):566–577, 2002.

[12] J. Blok, J. Van Dijk, G. Drost, M. Zwarts, and D. Stegeman. A high-density multichannel surface electromyography system for the characterization of single motor units. *Review of scientific instruments*, 73(4):1887–1897, 2002.

[13] G. Box, G. Jenkins, and G. Reinsel. *Time series analysis: forecasting and control*, volume 734. Wiley, 2011.

[14] H. Breiter, S. Rauch, K. Kwong, J. Baker, R. Weisskoff, D. Kennedy, A. Kendrick, T. Davis, A. Jiang, M. Cohen, et al. Functional magnetic resonance imaging of symptom provocation in obsessive-compulsive disorder. *Archives of General Psychiatry*, 53(7):595, 1996.

[15] L. Brett and S. Levine. Schedule-induced polydipsia suppresses pituitary-adrenal activity in rats. *Journal of Comparative and Physiological Psychology*, 93(5):946, 1979.

[16] L. Brett and S. Levine. The pituitary-adrenal response to "minimized" schedule-induced drinking. *Physiology & behavior*, 26(2):153–158, 1981.

[17] E. Brown, R. Kass, and P. Mitra. Multiple neural spike train data analysis: state-of-the-art and future challenges. *Nature neuroscience*, 7(5):456–461, 2004.

[18] G. Buzsaki. *Rhythms of the Brain*. Oxford University Press, USA, 2009.

[19] G. Buzsaki, R. Traub, and T. Pedley. The cellular basis of eeg activity. *Current practice of clinical electroencephalography. Philadelphia: Lippincott Williams & Wilkins*, 2003.

[20] J. Cai, E. Candès, and Z. Shen. A singular value thresholding algorithm for matrix completion. *SIAM Journal on Optimization*, 20(4):1956–1982, 2010.

[21] E. Candes and Y. Plan. Matrix completion with noise. *Proceedings of the IEEE*, 98(6):925–936, 2010.

[22] E. Candès and B. Recht. Exact matrix completion via convex optimization. *Foundations of Computational mathematics*, 9(6):717–772, 2009.

[23] N. Carlson. *Foundations of Physiological Psychology*. Needham Heights, Massachusetts: Simon and Schuster., 1992.

[24] M. Castella, P. Bianchi, A. Chevreuil, and J. Pesquet. A blind source separation framework for detecting cpm sources mixed by a convolutive mimo filter. *Signal processing*, 86(8):1950–1967, 2006.

[25] H. Chan, M. Lin, S. Lee, Y. Tsai, P. Chao, and T. Wu. Complex analysis of neuronal spike trains of deep brain nuclei in patients with parkinson's disease. *Brain research bulletin*, 81(6):534–542, 2010.

[26] W. Chung, G. De Vries, and D. Swaab. Sexual differentiation of the bed nucleus of the stria terminalis in humans may extend into adulthood. *The Journal of Neuroscience*, 22(3):1027–1033, 2002.

[27] J. Cocatre-Zilgien and F. Delcomyn. Identification of bursts in spike trains. *Journal of neuroscience methods*, 41(1):19–30, 1992.

[28] K. Commons, K. Connolley, and R. Valentino. A neurochemically distinct dorsal raphe-limbic circuit with a potential role in affective disorders. *Neuropsychopharmacology*, 28(2):206–215, 2003.

[29] M. Dalsass and A. Siegel. The bed nucleus of the stria terminalis: electrophysiological properties and responses to amygdaloid and hypothalamic stimulation. *Brain research*, 425(2):346–350, 1987.

[30] R. Dantzer and P. Mormède. Pituitary-adrenal consequences of adjunctive activities in pigs. *Hormones and behavior*, 15(4):386–395, 1981.

[31] I. Daubechies, J. Lu, and H. Wu. Synchrosqueezed wavelet transforms: An empirical mode decomposition-like tool. *Applied and Computational Harmonic Analysis*, 30(2):243–261, 2011.

[32] P. Dayan and L. Abbott. *Theoretical neuroscience*, volume 31. MIT press Cambridge, MA, 2001.

[33] C. De Luca, A. Adam, R. Wotiz, L. Gilmore, and S. Nawab. Decomposition of surface emg signals. *Journal of neurophysiology*, 96(3):1646–1657, 2006.

[34] C. De Luca and E. Hostage. Relationship between firing rate and recruitment threshold of motoneurons in voluntary isometric contractions. *Journal of neurophysiology*, 104(2):1034–1046, 2010.

[35] D. Decoste and B. Schölkopf. Training invariant support vector machines. *Machine Learning*, 46(1):161–190, 2002.

[36] A. Del Casale, G. Kotzalidis, C. Rapinesi, D. Serata, E. Ambrosi, A. Simonetti, M. Pompili, S. Ferracuti, R. Tatarelli, and P. Girardi. Functional neuroimaging in obsessive-compulsive disorder. *Neuropsychobiology*, 64(2):61–85, 2011.

[37] D. Denny-Brown. Interpretation of the electromyogram. *Archives of neurology and psychiatry*, 61(2):99–28, 1949.

[38] D. Denys et al. Pharmacotherapy of obsessive-compulsive disorder and obsessive-compulsive spectrum disorders. *The Psychiatric clinics of North America*, 29(2):553, 2006.

[39] D. Denys, N. van der Wee, J. Janssen, F. De Geus, and H. Westenberg. Low level of dopaminergic d< sub> 2</sub> receptor binding in obsessive-compulsive disorder. *Biological psychiatry*, 55(10):1041–1045, 2004.

[40] D. Denys, H. VAN MEGEN, and H. Westenberg. Quetiapine addition to serotonin reuptake inhibitor treatment in patients with treatment-refractory obsessive-compulsive disorder: an open-label study. *The Journal of clinical psychiatry*, 63(8):700–703, 2002.

[41] P. Diggle, P. Heagerty, K. Liang, and S. Zeger. *Analysis of longitudinal data*, volume 25. Oxford University Press, USA, 2002.

[42] D. Dimitriadis, A. Potamianos, and P. Maragos. A comparison of the squared energy and teager-kaiser operators for short-term energy estimation in additive noise. *Signal Processing, IEEE Transactions on*, 57(7):2569–2581, 2009.

[43] C. Disselhorst-Klug, J. Silny, and G. Rau. Improvement of spatial resolution in surface-emg: a theoretical and experimental comparison of different spatial filters. *Biomedical Engineering, IEEE Transactions on*, 44(7):567–574, 1997.

[44] D. Dixon, A. Ackert, and L. Eckel. Development of, and recovery from, activity-based anorexia in female rats. *Physiology & behavior*, 80(2):273–279, 2003.

[45] K. Dolan, H. Martens, P. Schuurman, and L. Bour. Automatic noise-level detection for extra-cellular micro-electrode recordings. *Medical and Biological Engineering and Computing*, 47(7):791–800, 2009.

[46] H. Dong and L. Swanson. Organization of axonal projections from the anterolateral area of the bed nuclei of the stria terminalis. *The Journal of comparative neurology*, 468(2):277–298, 2003.

[47] D. Donoho and J. Johnstone. Ideal spatial adaptation by wavelet shrinkage. *Biometrika*, 81(3):425–455, 1994.

[48] L. Dorfman, J. Howard, and K. McGill. Motor unit firing rates and firing rate variability in the detection of neuromuscular disorders. *Electroencephalography and clinical neurophysiology*, 73(3):215–224, 1989.

[49] G. Drost, B. Kleine, D. Stegeman, B. van Engelen, and M. Zwarts. Fasciculation potentials in high-density surface emg. *Journal of Clinical Neurophysiology*, 24(3):301–307, 2007.

[50] G. Drost, D. Stegeman, B. van Engelen, and M. Zwarts. Clinical applications of high-density surface emg: a systematic review. *Journal of Electromyography and Kinesiology*, 16(6):586–602, 2006.

[51] P. Duchamp-Viret, L. Kostal, M. Chaput, P. Lánsky, and J. Rospars. Patterns of spontaneous activity in single rat olfactory receptor neurons are different in normally breathing and tracheotomized animals. *Journal of neurobiology*, 65(2):97–114, 2005.

[52] É. Dumont and J. Williams. Noradrenaline triggers gabaa inhibition of bed nucleus of the stria terminalis neurons projecting to the ventral tegmental area. *The Journal of neuroscience*, 24(38):8198–8204, 2004.

[53] N. Ebrahimi, M. Habibullah, and E. Soofi. Testing exponentiality based on kullback-leibler information. *Journal of the Royal Statistical Society. Series B (Methodological)*, pages 739–748, 1992.

[54] P. Editore. *Advanced Methods of Biomedical Signal Processing*, volume 27. Wiley-IEEE Press, 2010.

[55] R. Egli and D. Winder. Dorsal and ventral distribution of excitable and synaptic properties of neurons of the bed nucleus of the stria terminalis. *Journal of neurophysiology*, 90(1):405–414, 2003.

[56] D. Farina, L. Arendt-Nielsen, R. Merletti, B. Indino, and T. Graven-Nielsen. Selectivity of spatial filters for surface emg detection from the tibialis anterior muscle. *Biomedical Engineering, IEEE Transactions on*, 50(3):354–364, 2003.

[57] D. Farina, E. Fortunato, and R. Merletti. Noninvasive estimation of motor unit conduction velocity distribution using linear electrode arrays. *Biomedical Engineering, IEEE Transactions on*, 47(3):380–388, 2000.

[58] D. Farina and R. Merletti. A novel approach for precise simulation of the emg signal detected by surface electrodes. *Biomedical Engineering, IEEE Transactions on*, 48(6):637–646, 2001.

[59] J. Favre, J. Taha, T. Baumann, and K. Burchiel. Computer analysis of the tonic, phasic, and kinesthetic activity of pallidal discharges in parkinson patients. *Surgical neurology*, 51(6):665–673, 1999.

[60] J. Florestal, P. Mathieu, and A. Malanda. Automated decomposition of intramuscular electromyographic signals. *Biomedical Engineering, IEEE Transactions on*, 53(5):832–839, 2006.

[61] J. Florestal, P. Mathieu, and K. McGill. Automatic decomposition of multichannel intramuscular emg signals. *Journal of Electromyography and Kinesiology*, 19(1):1–9, 2009.

[62] F. Gabbiani and C. Koch. Principles of spike train analysis. *Methods in neuronal modeling*, pages 313–360, 1998.

[63] L. Gabriëls, B. Nuttin, and P. Cosyns. Dbs and the treatment of obsessive compulsive disorder. In *Proceedings Of The Medtronic Forum for Neuroscience And Neuro-Technology 2005*, volume 1, page 57. Springer Verlag, 2006.

[64] M. Gazzoni, D. Farina, and R. Merletti. A new method for the extraction and classification of single motor unit action potentials from surface emg signals. *Journal of neuroscience methods*, 136(2):165, 2004.

[65] F. Georges and G. Aston-Jones. Activation of ventral tegmental area cells by the bed nucleus of the stria terminalis: a novel excitatory amino acid input to midbrain dopamine neurons. *The Journal of neuroscience*, 22(12):5173–5187, 2002.

[66] W. Gerstner, A. Kreiter, H. Markram, and A. Herz. Neural codes: firing rates and beyond. *Proceedings of the National Academy of Sciences*, 94(24):12740–12741, 1997.

[67] S. Gibson, J. Judy, and D. Markovic. Spike sorting: The first step in decoding the brain. *Signal Processing Magazine, IEEE*, 29(1):124–143, 2012.

[68] I. Gligorijević, M. De Vos, J. Blok, B. Mijović, J. van Dijk, and S. Van Huffel. Automated way to obtain motor units' signatures and estimate their firing patterns during voluntary contractions using hd-semg. In *Engineering in Medicine and Biology Society, EMBC, 2011 Annual International Conference of the IEEE*, pages 4090–4093. IEEE, 2011.

[69] I. Gligorijević, J. Dijk, B. Mijović, S. Huffel, J. Blok, and M. Vos. A new and fast approach towards semg decomposition. *Medical & Biological Engineering & Computing*, pages 1–13, 2013.

[70] I. Gligorijević, B. Sleutjes, M. De Vos, J. Blok, I. Montfoort, B. Mijović, M. Signoretto, and S. Van Huffel. Correcting electrode displacement errors in motor unit tracking using high density surface electromyography (hdsemg). In *7th International Workshop on Biosignal Interpretation (BSI2012), Como, Italy*, pages 1–4. IMIA,IFMBE,IEEE-EMBS, 2012.

[71] I. Gligorijević, M. Welkenhuysen, D. Prodanov, W. Eberle, B. Nuttin, C. Bartic, and S. Van Huffel. Statistical analysis of neural spike trains for evaluation of functional differences in brain activity. In *Proc. of the BIOSIGNAL 2010 Conference, Berlin, Germany*, 2010.

[72] I. Gligorijević, M. Welkenhuysen, D. Prodanov, S. Musa, B. Nuttin, W. Eberle, C. Bartic, and S. Van Huffel. Neural signal analysis and artifact removal in single and multichannel in-vivo deep brain recordings. In *Proc. of 4th Annual*

Symposium of the IEEE-EMBS Benelux Chapter (IEEE-EMBS), pages 79–82, 2009.

[73] X. Guangqi. Neuronal spike on-line classification and analysis. Master's thesis, Linköping University, Sweden, 2011.

[74] S. Hammack, J. Guo, R. Hazra, J. Dabrowska, K. Myers, and D. Rainnie. The response of neurons in the bed nucleus of the stria terminalis to serotonin: implications for anxiety. *Progress in Neuro-Psychopharmacology and Biological Psychiatry*, 33(8):1309–1320, 2009.

[75] P. Hansen and B. Jaumard. Cluster analysis and mathematical programming. *Mathematical programming*, 79(1):191–215, 1997.

[76] R. Harrison, P. Watkins, R. Kier, R. Lovejoy, D. Black, B. Greger, and F. Solzbacher. A low-power integrated circuit for a wireless 100-electrode neural recording system. *Solid-State Circuits, IEEE Journal of*, 42(1):123–133, 2007.

[77] J. Hartigan and P. Hartigan. The dip test of unimodality. *The Annals of Statistics*, 13(1):70–84, 1985.

[78] P. Hartigan. Algorithm as 217: Computation of the dip statistic to test for unimodality. *Journal of the Royal Statistical Society. Series C (Applied Statistics)*, 34(3):320–325, 1985.

[79] M. Häusser, N. Spruston, and G. Stuart. Diversity and dynamics of dendritic signaling. *Science*, 290(5492):739–744, 2000.

[80] I. Heyman, E. Fombonne, H. Simmons, T. Ford, H. Meltzer, and R. Goodman. Prevalence of obsessive—compulsive disorder in the british nationwide survey of child mental health. *The British Journal of Psychiatry*, 179(4):324–329, 2001.

[81] M. Hines, L. Allen, and R. Gorski. Sex differences in subregions of the medial nucleus of the amygdala and the bed nucleus of the stria terminalis of the rat. *Brain research*, 579(2):321–326, 1992.

[82] S. Hogg and A. Dalvi. Acceleration of onset of action in schedule-induced polydipsia: combinations of ssri and 5-ht< sub> 1a</sub> and 5-ht< sub> 1b</sub> receptor antagonists. *Pharmacology Biochemistry and Behavior*, 77(1):69–75, 2004.

[83] A. Holobar. On repeatability of motor unit identification in multi-channel surface electromyograms of the external sphincter muscle. In *Proc. of ERK, Protoroz, Slovenia*, 2007.

[84] A. Holobar, M. Minetto, A. Botter, F. Negro, and D. Farina. Experimental analysis of accuracy in the identification of motor unit spike trains from high-density surface emg. *Neural Systems and Rehabilitation Engineering, IEEE Transactions on*, 18(3):221–229, 2010.

[85] A. Holobar and D. Zazula. Multichannel blind source separation using convolution kernel compensation. *Signal Processing, IEEE Transactions on*, 55(9):4487–4496, 2007.

[86] R. Howard and N. Murray. Surface emg in the recording of fasciculations. *Muscle & nerve*, 15(11):1240–1245, 1992.

[87] W. Huff, D. Lenartz, M. Schormann, S. Lee, J. Kuhn, A. Koulousakis, J. Mai, J. Daumann, M. Maarouf, J. Klosterkötter, et al. Unilateral deep brain stimulation of the nucleus accumbens in patients with treatment-resistant obsessive-compulsive disorder: outcomes after one year. *Clinical neurology and neurosurgery*, 112(2):137–143, 2010.

[88] M. Jalabert, G. Aston-Jones, E. Herzog, O. Manzoni, and F. Georges. Role of the bed nucleus of the stria terminalis in the control of ventral tegmental area dopamine neurons. *Progress in Neuro-Psychopharmacology and Biological Psychiatry*, 33(8):1336–1346, 2009.

[89] I. Jolliffe. *Principal component analysis*. Wiley Online Library, 2005.

[90] E. Kandel, J. Schwartz, T. Jessell, et al. *Principles of neural science*, volume 4. McGraw-Hill New York, 2000.

[91] T. Kash, R. Matthews, and D. Winder. Alcohol inhibits nr2b-containing nmda receptors in the ventral bed nucleus of the stria terminalis. *Neuropsychopharmacology*, 33(6):1379–1390, 2007.

[92] K. Kim and S. Kim. Neural spike sorting under nearly 0-db signal-to-noise ratio using nonlinear energy operator and artificial neural-network classifier. *Biomedical Engineering, IEEE Transactions on*, 47(10):1406–1411, 2000.

[93] K. Kim and S. Kim. A wavelet-based method for action potential detection from extracellular neural signal recording with low signal-to-noise ratio. *Biomedical Engineering, IEEE Transactions on*, 50(8):999–1011, 2003.

[94] B. Kleine, J. van Dijk, B. Lapatki, M. Zwarts, and D. Stegeman. Using two-dimensional spatial information in decomposition of surface emg signals. *Journal of Electromyography and Kinesiology*, 17(5):535–548, 2007.

[95] B. Kleine, J. van Dijk, M. Zwarts, and D. Stegeman. Inter-operator agreement in decomposition of motor unit firings from high-density surface emg. *Journal of Electromyography and Kinesiology*, 18(4):652–661, 2008.

[96] N. Koolen. Reliability of statistical features describing neural spike trains in presence of classification errors. Master's thesis, Department of Electrical Engineering (ESAT), KU Leuven, 2010 – 2011.

[97] N. Koolen, I. Gligorijević, and S. Van Huffel. Reliability of statistical features describing neural spike trains in the presence of classification errors. In *Proceedings of the International Conference on Bio-inspired Systems and Signal Processing (BIOSIGNALS 2012)*, volume 1, pages 169–173, 2012.

[98] L. Kostal, P. Lansky, and J. Rospars. Review article: Neuronal coding and spiking randomness. *European Journal of Neuroscience*, 26(10):2693–2701, 2007.

[99] G. Kreiman, C. Hung, A. Kraskov, R. Quiroga, T. Poggio, and J. DiCarlo. Object selectivity of local field potentials and spikes in the macaque inferior temporal cortex. *Neuron*, 49(3):433–445, 2006.

[100] K. Kuyck, K. Brak, J. Das, D. Rizopoulos, and B. Nuttin. Comparative study of the effects of electrical stimulation in the nucleus accumbens, the mediodorsal thalamic nucleus and the bed nucleus of the stria terminalis in rats with schedule-induced polydipsia. *Brain research*, 1201:93–99, 2008.

[101] R. Lambert, F. Moos, C. Ingram, J. Wakerley, P. Kremarik, Y. Guerne, and P. Richard. Electrical activity of neurons in the ventrolateral septum and bed nuclei of the stria terminalis in suckled rats: statistical analysis gives evidence for sensitivity to oxytocin and for relation to the milk-ejection reflex. *Neuroscience*, 54(2):361–376, 1993.

[102] B. Lapatki. The facial musculature–characterization at a motor unit level. *Unpublished doctoral dissertation, Radboud University, Nijmegen*, 2010.

[103] B. Lapatki, R. Oostenveld, J. Van Dijk, I. Jonas, M. Zwarts, and D. Stegeman. Topographical characteristics of motor units of the lower facial musculature revealed by means of high-density surface emg. *Journal of neurophysiology*, 95(1):342–354, 2006.

[104] B. Lapatki, J. Van Dijk, I. Jonas, M. Zwarts, and D. Stegeman. A thin, flexible multielectrode grid for high-density surface emg. *Journal of Applied Physiology*, 96(1):327–336, 2004.

[105] J. Lee, A. Adam, and C. De Luca. A simulation study for a surface emg sensor that detects distinguishable motor unit action potentials. *Journal of neuroscience methods*, 168(1):54–63, 2008.

[106] Y. Lee and M. Davis. Role of the hippocampus, the bed nucleus of the stria terminalis, and the amygdala in the excitatory effect of corticotropin-releasing hormone on the acoustic startle reflex. *The Journal of neuroscience*, 17(16):6434–6446, 1997.

[107] R. LeFever and C. De Luca. A procedure for decomposing the myoelectric signal into its constituent action potentials-part i: technique, theory, and implementation. *Biomedical Engineering, IEEE Transactions on*, (3):149–157, 1982.

[108] C. Legendy and M. Salcman. Bursts and recurrences of bursts in the spike trains of spontaneously active striate cortex neurons. *Journal of neurophysiology*, 53(4):926–939, 1985.

[109] R. Lemon and A. Prochazka. *Methods for neuronal recording in conscious animals*, volume 4. Wiley London:, 1984.

[110] J. Letelier and P. Weber. Spike sorting based on discrete wavelet transform coefficients. *Journal of neuroscience methods*, 101(2):93–106, 2000.

[111] M. Lewicki. A review of methods for spike sorting: the detection and classification of neural action potentials. *Network: Computation in Neural Systems*, 9(4):53–78, 1998.

[112] K. Liang and S. Zeger. Longitudinal data analysis using generalized linear models. *Biometrika*, 73(1):13–22, 1986.

[113] H. Lilliefors. On the kolmogorov-smirnov test for normality with mean and variance unknown. *Journal of the American Statistical Association*, 62(318):399–402, 1967.

[114] M. Lopez-Grancha, G. Lopez-Crespo, C. Venero, F. Cañadas, F. Sanchez-Santed, C. Sandi, and P. Flores. Differences in corticosterone level due to inter-food interval length: implications for schedule-induced polydipsia. *Hormones and behavior*, 49(2):166–172, 2006.

[115] E. Maathuis, J. Drenthen, J. van Dijk, G. Visser, and J. Blok. Motor unit tracking with high-density surface emg. *Journal of Electromyography and Kinesiology*, 18(6):920–930, 2008.

[116] J. MacQueen et al. Some methods for classification and analysis of multivariate observations. In *Proceedings of the fifth Berkeley symposium on mathematical statistics and probability*, volume 1, page 14. California, USA, 1967.

[117] J. Mai, J. Assheuer, and G. Paxinos. Atlas of the human brain, vol, 2004.

[118] F. J. Massey Jr. The kolmogorov-smirnov test for goodness of fit. *Journal of the American statistical Association*, 46(253):68–78, 1951.

[119] T. Masuda and T. Sadoyama. The propagation of single motor unit action potentials detected by a surface electrode array. *Electroencephalography and clinical Neurophysiology*, 63(6):590–598, 1986.

[120] W. Mathieson, P. Federico, W. Veale, and Q. Pittman. Single-unit activity in the bed nucleus of the stria terminalis during fever. *Brain research*, 486(1):49–55, 1989.

[121] Z. McElligott and D. Winder. Modulation of glutamatergic synaptic transmission in the bed nucleus of the stria terminalis. *Progress in Neuropsychopharmacology and Biological Psychiatry*, 33(8):1329–1335, 2009.

[122] K. McGill. Optimal resolution of superimposed action potentials. *Biomedical Engineering, IEEE Transactions on*, 49(7):640–650, 2002.

[123] R. Merletti, A. Holobar, and D. Farina. Analysis of motor units with high-density surface electromyography. *Journal of Electromyography and Kinesiology*, 18(6):879–890, 2008.

[124] R. Merletti, A. Rainoldi, and D. Farina. Surface electromyography for noninvasive characterization of muscle. *Exercise and sport sciences reviews*, 29(1):20–25, 2001.

[125] B. Mijović, M. De Vos, I. Gligorijević, J. Taelman, and S. Van Huffel. Source separation from single-channel recordings by combining empirical-mode decomposition and independent component analysis. *Biomedical Engineering, IEEE Transactions on*, 57(9):2188–2196, 2010.

[126] B. Mijović, M. De Vos, I. Gligorijević, and S. Van Huffel. Combining emd with ica for extracting independent sources from single channel and two-channel data. In *Engineering in Medicine and Biology Society (EMBC), 2010 Annual International Conference of the IEEE*, pages 5387–5390. IEEE, 2010.

[127] M. Moga, C. Saper, and T. Gray. Bed nucleus of the stria terminalis: cytoarchitecture, immunohistochemistry, and projection to the parabrachial nucleus in the rat. *The Journal of comparative neurology*, 283(3):315–332, 2004.

[128] F. Mosteller and J. Tukey. Data analysis and regression. a second course in statistics. *Addison-Wesley Series in Behavioral Science: Quantitative Methods, Reading, Mass.: Addison-Wesley, 1977*, 1, 1977.

[129] S. Musa. *Design, Fabrication, and Characterization of a Neural Probe for Deep Brain Stimulation and Recording*. PhD thesis, Faculty of Science, KU Leuven(Belgium), 2011.

[130] S. Musa, M. Welkenhuysen, D. Prodanov, W. Eberle, C. Bartic, B. Nuttin, and G. Borghs. In vitro and in vivo electrochemical characterization of a microfabricated neural probe. In *Engineering in Medicine and Biology Society, 2009. EMBC 2009. Annual International Conference of the IEEE*, pages 7143–7146. IEEE, 2009.

[131] B. Myklebust, G. Gottlieb, and G. Agarwal. Stretch reflexes of the normal infant. *Developmental Medicine & Child Neurology*, 28(4):440–449, 1986.

[132] S. Nawab, S. Chang, and C. De Luca. High-yield decomposition of surface emg signals. *Clinical Neurophysiology*, 121(10):1602–1615, 2010.

[133] Z. Nenadic and J. Burdick. Spike detection using the continuous wavelet transform. *Biomedical Engineering, IEEE Transactions on*, 52(1):74–87, 2005.

[134] Z. Nenadic and J. W. Burdick. A control algorithm for autonomous optimization of extracellular recordings. *Biomedical Engineering, IEEE Transactions on*, 53(5):941–955, 2006.

[135] Z. Ni, R. Bouali-Benazzouz, D. Gao, A. Benabid, and A. Benazzouz. Changes in the firing pattern of globus pallidus neurons after the degeneration of nigrostriatal pathway are mediated by the subthalamic nucleus in the rat. *European Journal of Neuroscience*, 12(12):4338–4344, 2000.

[136] E. Nordstrom, F. Burton, et al. A transgenic model of comorbid tourette's syndrome and obsessive-compulsive disorder circuitry. *Molecular psychiatry*, 7(6):617–625, 2002.

[137] B. Nuttin, P. Cosyns, H. Demeulemeester, J. Gybels, and B. Meyerson. Electrical stimulation in anterior limbs of internal capsules in patients with obsessive-compulsive disorder. *The Lancet*, 354(9189):1526, 1999.

[138] B. Nuttin, L. Gabriëls, P. Cosyns, B. Meyerson, S. Andréewitch, S. Sunaert, A. Maes, P. Dupont, J. Gybels, F. Gielen, et al. Long-term electrical capsular stimulation in patients with obsessive-compulsive disorder. *Neurosurgery*, 52(6):1263–1274, 2003.

[139] I. Obeid. Comparison of spike detectors based on simultaneous intracellular and extracellular recordings. In *Neural Engineering, 2007. CNE'07. 3rd International IEEE/EMBS Conference on*, pages 410–413. IEEE, 2007.

[140] S. Pallanti, E. Hollander, C. Bienstock, L. Koran, J. Leckman, D. Marazziti, M. Pato, D. Stein, and J. Zohar. Treatment non-response in ocd: methodological issues and operational definitions. *The International Journal of Neuropsychopharmacology*, 5(02):181–191, 2002.

[141] H. Parsaei, F. Nezhad, D. Stashuk, and A. Hamilton-Wright. Validating motor unit firing patterns extracted by emg signal decomposition. *Medical and Biological Engineering and Computing*, 49(6):649–658, 2011.

[142] H. Parsaei and D. Stashuk. A method for detecting and editing mupts contaminated by false classification errors during emg signal decomposition. In *Engineering in Medicine and Biology Society, EMBC, 2011 Annual International Conference of the IEEE*, pages 4394–4397. IEEE, 2011.

[143] G. Paxinos and C. Watson. *The rat brain in stereotaxic coordinates*. Academic press, 2007.

[144] J. Perlmutter and J. Mink. Deep brain stimulation. *Annu. Rev. Neurosci.*, 29:229–257, 2006.

[145] C. Phelix, Z. Liposits, and W. Paull. Serotonin-crf interaction in the bed nucleus of the stria terminalis: a light microscopic double-label immunocytochemical analysis. *Brain research bulletin*, 28(6):943–948, 1992.

[146] R. Pitman. Animal models of compulsive behavior. *Biological psychiatry*, 26(2):189–198, 1989.

[147] B. Platt, C. Beyer, L. Schechter, and S. Rosenzweig-Lipson. Schedule-induced polydipsia: A rat model of obsessive-compulsive disorder. *Curr Protoc Neurosci*, 9:1–7, 2008.

[148] S. Pullman, D. Goodin, A. Marquinez, S. Tabbal, and M. Rubin. Clinical utility of surface emg report of the therapeutics and technology assessment subcommittee of the american academy of neurology. *Neurology*, 55(2):171–177, 2000.

[149] R. Quian Quiroga, Z. Nadasdy, and Y. Ben-Shaul. Unsupervised spike detection and sorting with wavelets and superparamagnetic clustering. 2004.

[150] M. Rasch, A. Gretton, Y. Murayama, W. Maass, and N. Logothetis. Inferring spike trains from local field potentials. *Journal of neurophysiology*, 99(3):1461–1476, 2008.

[151] M. Rizk and P. Wolf. Optimizing the automatic selection of spike detection thresholds using a multiple of the noise level. *Medical and Biological Engineering and Computing*, 47(9):955–966, 2009.

[152] K. Roeleveld, J. Blok, D. Stegeman, and A. Van Oosterom. Volume conduction models for surface emg; confrontation with measurements. *Journal of Electromyography and Kinesiology*, 7(4):221–232, 1997.

[153] K. Roeleveld, D. Stegeman, B. Falck, and E. Stålberg. Motor unit size estimation: confrontation of surface emg with macro emg. *Electroencephalography and Clinical Neurophysiology/Electromyography and Motor Control*, 105(3):181–188, 1997.

[154] K. Roeleveld, D. Stegeman, H. Vingerhoets, and A. Oosterom. The motor unit potential distribution over the skin surface and its use in estimating the motor unit location. *Acta physiologica scandinavica*, 161(4):465–472, 1997.

[155] U. Rutishauser, E. Schuman, and A. Mamelak. Online detection and sorting of extracellularly recorded action potentials in human medial temporal lobe recordings, in vivo. *Journal of neuroscience methods*, 154(1):204–224, 2006.

[156] S. Saxena, A. Brody, J. Schwartz, and L. Baxter. Neuroimaging and frontal-subcortical circuitry in obsessive-compulsive disorder. *British Journal of Psychiatry*, 1998.

[157] J. Schwartz, E. Kandel, and T. Jessell. *Principles of neural science*. Prentice-Hall International, 1991.

[158] D. Science. Sports science - contraction of muscles, 2013. [Online; accessed 31-January-2013].

[159] L. Senhadji, J. Dillenseger, F. Wendling, C. Rocha, and A. Kinie. Wavelet analysis of eeg for three-dimensional mapping of epileptic events. *Annals of biomedical engineering*, 23(5):543–552, 1995.

[160] M. Shadlen and W. Newsome. Noise, neural codes and cortical organization. *Current opinion in neurobiology*, 4(4):569–579, 1994.

[161] C. Shannon and W. Weaver. Mathematical theory of communication. 2002.

[162] M. Sheikh and D. Johnson. Fundamental detection and estimation limits in spike sorting. In *Acoustics, Speech and Signal Processing, 2007. ICASSP 2007. IEEE International Conference on*, volume 1, pages I–329. IEEE, 2007.

[163] G. Skoog and I. Skoog. A 40-year follow-up of patients with obsessive-compulsive disorder. *Archives of General Psychiatry*, 56(2):121, 1999.

[164] J. Starck, Y. Moudden, J. Bobin, M. Elad, and D. Donoho. Morphological component analysis. In *Proceedings of the SPIE conference wavelets*, volume 5914, page 191. Citeseer, 2005.

[165] R. Stein, E. Gossen, and K. Jones. Neuronal variability: noise or part of the signal? *Nature Reviews Neuroscience*, 6(5):389–397, 2005.

[166] D. Straker. *A toolbook for quality improvement and problem solving*. Prentice Hall Englewood Cliffs, NJ, 1995.

[167] B. I. Susan Dean. Descriptive statistics: Skewness and the mean, median, and mode, 2012. [Online; accessed 3-December-2012].

[168] H. Taba, S. Wu, K. Foote, C. Hass, H. Fernandez, I. Malaty, R. Rodriguez, Y. Dai, P. Zeilman, C. Jacobson IV, et al. A closer look at unilateral versus bilateral deep brain stimulation: results of the national institutes of health compare cohort. *Journal of neurosurgery*, 113(6):1224–1229, 2010.

[169] J. Ting and G. Feng. Glutamatergic synaptic dysfunction and obsessive-compulsive disorder. *Current chemical genomics*, 2:62, 2008.

[170] A. Troiano, F. Naddeo, E. Sosso, G. Camarota, R. Merletti, and L. Mesin. Assessment of force and fatigue in isometric contractions of the upper trapezius muscle by surface emg signal and perceived exertion scale. *Gait & posture*, 28(2):179, 2008.

[171] J. van Dijk. *On the number of motor units*. PhD thesis, Radbound University Nijmegen (Netherlands), June 2010.

[172] J. van Dijk, J. Blok, B. Lapatki, I. van Schaik, M. Zwarts, and D. Stegeman. Motor unit number estimation using high-density surface electromyography. *Clinical Neurophysiology*, 119(1):33–42, 2008.

[173] R. VanRullen, R. Guyonneau, and S. Thorpe. Spike times make sense. *Trends in neurosciences*, 28(1):1–4, 2005.

[174] O. Vasicek. A test for normality based on sample entropy. *Journal of the Royal Statistical Society. Series B (Methodological)*, pages 54–59, 1976.

[175] N. Vulink, D. Denys, S. Fluitman, J. Meinardi, and H. Westenberg. Quetiapine augments the effect of citalopram in non-refractory obsessive-compulsive disorder: a randomized, double-blind, placebo-controlled study of 76 patients. *Journal of Clinical Psychiatry*, 70(7):1001, 2009.

[176] D. Walker, D. Toufexis, and M. Davis. Role of the bed nucleus of the stria terminalis versus the amygdala in fear, stress, and anxiety. *European journal of pharmacology*, 463(1):199–216, 2003.

[177] M. Welkenhuysen. *Electrical brain stimulation and microrecording: Research in animal models for psychiatric disorders and in vivo evaluation of a neural probe*. PhD thesis, Faculty of Medicine, KU Leuven(Belgium), 2011.

[178] M. Welkenhuysen, I. Gligorijević, L. Ameye, D. Prodanov, S. Van Huffel, and B. Nuttin. Neuronal activity in the bed nucleus of the stria terminalis in a rat model for obsessive-compulsive disorder. *To appear in Behavioural Brain Research*, 240:52–59, 2013.

[179] H. Westenberg, N. Fineberg, and D. Denys. Neurobiology of obsessive-compulsive disorder: serotonin and beyond. *CNS Spectr*, 12(2 Suppl 3):14–27, 2007.

[180] Wikipedia. Neural coding — wikipedia, the free encyclopedia. `http://en.wikipedia.org/w/index.php?title=Neural_coding&oldid=524511814`, November 2012.

[181] M. Wilkinson and Q. Pittman. Changes in arterial blood pressure alter activity of electrophysiologically identified single units of the bed nucleus of the stria terminalis. *Neuroscience*, 64(3):835–844, 1995.

[182] H. Wittchen and F. Jacobi. Size and burden of mental disorders in europe—a critical review and appraisal of 27 studies. *European neuropsychopharmacology*, 15(4):357–376, 2005.

[183] A. Woods, C. Smith, M. Szewczak, R. Dunn, M. Cornfeldt, and R. Corbett. Selective serotonin re-uptake inhibitors decrease schedule-induced polydipsia in rats: a potential model for obsessive compulsive disorder. *Psychopharmacology*, 112(2):195–198, 1993.

[184] A. Wyler, E. Fetz, and A. Ward. Firing patterns of epileptic and normal neurons in the chronic alumina focus in undrugged monkeys during different behavioral states. *Brain research*, 98(1):1–20, 1975.

[185] R. Xu and D. Wunsch. Clustering algorithms in biomedical research: A review. *Biomedical Engineering, IEEE Reviews in*, 3:120–154, 2010.

[186] Z. Xu and W. Pulsinelli. Electrophysiological changes of ca1 pyramidal neurons following transient forebrain ischemia: an in vivo intracellular recording and staining study. *Journal of neurophysiology*, 76(3):1689–1697, 1996.

[187] Z. Xu, S. Xiao, and Z. Chi. Art2 neural network for surface emg decomposition. *Neural Computing & Applications*, 10(1):29–38, 2001.

[188] D. Zazula and A. Holobar. An approach to surface emg decomposition based on higher-order cumulants. *Computer methods and programs in biomedicine*, 80:S51–S60, 2005.

List of Publications

Papers in international journals

1. M. Welkenhuysen, **I. Gligorijević**, L. Ameye, D. Prodanov, S. Van Huffel and B. Nuttin. *Neuronal activity in the bed nucleus of the stria terminalis in a rat model for obsessive-compulsive disorder.* To appear in Behavioural Brain Research, vol. 240, 2013, pp. 52-59.

2. **I. Gligorijević**, J.P. van Dijk, B. Mijović, S. Van Huffel, J.H. Blok, M. De Vos. *A new and fast approach towards sEMG decomposition.* Medical and Biological Engineering and Computing, Accepted for publication, Nov. 2012.

3. C.M. Lopez, D. Prodanov, D. Braeken, **I. Gligorijević**, W. Eberle, C. Bartic and G. Gielen. *A Multichannel Integrated Circuit for Electrical Recording of Neural Activity, With Independent Channel Programmability.* IEEE Transactions on Biomedical Circuits and Systems, vol. 6, no. 2, 2012, pp. 101-110.

4. K. Mols, **I. Gligorijević**, D. Prodanov and B. Nuttin. *Signal analysis of the effects of microlesions in the medial septal area on the dominant hippocampal rhythm in anesthetized rats.* Neuroscience letters, vol. 500, supplement, July 2011, pp. 27-28.

5. B. Mijović, M. De Vos, **I. Gligorijević**, J. Taelman and S. Van Huffel. *Source Separation from Single-Channel Recordings by Combining Empirical Mode Decomposition and Independent Component Analysis.* IEEE Transaction on Biomedical Engineering, vol. 57, no. 9, 2010, pp. 2188 - 2196.

Papers submitted to international journals

6. Y. Liu, M. De Vos, **I. Gligorijević**, V. Matić, Y. Li and S. Van Huffel. *Multi-Structural Signal Recovery for Biomedical Compressive Sensing: A Unified*

Framework. IEEE Transactions on Biomedical Engineering, submitted, Dec. 2012.

Papers in proceedings of international conferences

7. Y. Liu, **I. Gligorijević**, V. Matić, M De Vos and S. Van Huffel. *Multi-Sparse Signal Recovery for Compressive Sensing.* in Proc. of the 34th Annual International Conference of the IEEE Engineering in Medicine and Biology Society (IEEE EMBC San Diego), San Diego, USA, Aug. 2012, pp. 1-4.

8. **I. Gligorijević**, B.T.H.M. Sleutjes, M. De Vos, J.H. Blok, I. Montfoort, B. Mijović, M. Signoretto and S. Van Huffel. *Correcting electrode displacement errors in motor unit tracking using high density surface electromyography (HDsEMG).* 7th International Workshop on Biosignal Interpretation (BSI2012), Como, Italy, July 2012, pp. 1-4.

9. N. Koolen, **I. Gligorijević** and S. Van Huffel. *Reliability of Statistical Features Describing Neural Spike Trains in the Presence of Classification Errors.* in Proc. of the International Conference on Bio-inspired Systems and Signal Processing (BIOSIGNALS 2012), Vilamoura, Portugal, Feb. 2012, pp. 169-173.

10. **I. Gligorijević**, M. De Vos, J.H. Blok, B. Mijović, J.P. van Dijk and S. Van Huffel. *Automated way to obtain motor units' signatures and estimate their firing patterns during voluntary contractions using HD-sEMG.* in Proc. of the 33rd Annual International Conference of the IEEE Engineering in Medicine and Biology Society (IEEE EMBS Boston), Boston, Massachusetts, Aug. 2011, pp. 4090-4093.

11. J. Taelman, S. Vandeput, **I. Gligorijević**, A. Spaepen and S. Van Huffel. *Time-frequency heart rate variability characteristics of young adults during physical, mental and combined stress in laboratory environment.* in Proc. of the 33rd Annual International Conference of the IEEE Engineering in Medicine and Biology Society (IEEE EMBC), Boston, Massachusetts, Sep. 2011, pp. 1973-1976.

12. B. Mijović, M. De Vos, **I. Gligorijević** and S. Van Huffel. *Combining EMD with ICA for Extracting Independent Sources from Single Channel and Two-Channel Data.* in Proc. of the 32rd Annual International Conference of the IEEE Engineering in Medicine and Biology Society (IEEE EMBS Buenos Aires), Buenos Aires, Argentina, Aug. 2010, pp. 5387-5390.

13. **I. Gligorijević**, M. Welkenhuysen, D. Prodanov, W. Eberle, B. Nuttin, C. Bartic and S. Van Huffel. *Statistical analysis of neural spike trains*

for evaluation of functional differences in brain activity. in Proc. of the BIOSIGNAL 2010 conference (BIOSIGNAL 2010), Berlin, Germany, Jul. 2010.

14. **I. Gligorijević**, M. Welkenhuysen, D. Prodanov, S. Musa, B. Nuttin, W. Eberle, C. Bartic and S. Van Huffel. *Neural signal analysis and artifact removal in single and multichannel in-vivo deep brain recordings.* in Proc. of 4th Annual Symposium of the IEEE-EMBS Benelux Chapter (IEEE-EMBS), Twente, The Netherlands, Nov. 2009, pp. 79-82.

Abstracts in proceedings of international conferences

15. **I. Gligorijević**, M. De Vos, H. van Dijk, J. Blok and S. Van Huffel. *A novel approach to voluntary HD-sEMG decomposition.* 3rd Dutch conference on Biomedical Engineering, Egmond aan Zee, The Netherlands, Jan. 2011.

16. B. Nuttin, C. Bartic, M. Welkenhuysen, S. Musa, W. Eberle, K. van Kuyck, L. Luyten, D. Prodanov, **I. Gligorijević**, S. Van Huffel, J. Das, L. Gabriëls, J.P. Kruth, K. Verstreken and G. Borghs. *Concept of bridging the lesion cavity wall with stimulating and recording devices in the central nervous system.* European Society for Stereotactic and Functional Neurosurgery, Athene, Greece, Sep. 2010.

Curriculum Vitae

Ivan Gligorijević was born in Ćuprija, Serbia on March 13, 1983. He received the MSc. degree in Electrical Engineering from the University of Belgrade, Serbia in September 2008. His master thesis "Surface plasmon resonance (SPR) based dip fiber optic sensor using multimode fibers - theoretical and practical treatment" was performed in ESAT/SCD/SISTA-Biomed group, KU Leuven and defended in the Faculty of Electrical Engineering, Belgrade University, Serbia.

In October 2008, he joined the SISTA research group at the Department of Electrical Engineering (ESAT), KU Leuven, Belgium as a predoctoral student. In January 2009, he started his PhD program with the focus on neural signal analysis with the initial emphasis on closing the loop between deep brain stimulation and recording. As such, he was involved in the joint research with IMEC - Belgium (BioNe/BES group). He later worked on high-density surface electromyography (HD-sEMG) related research in collaboration with the Department of Clinical Neurophysiology, Erasmus MC Rotterdam, The Netherlands.